Title
Structural, functional and cellular characterization of mitochondrial Phosphoglycerate Mutase 5

Author
Ruiz, Karen Paola

Publication Date
2019

Peer reviewed|Thesis/dissertation

Structural, functional and cellular characterization of mitochondrial Phosphoglycerate Mutase 5

by
Karen Ruiz

DISSERTATION
Submitted in partial satisfaction of the requirements for degree of
DOCTOR OF PHILOSOPHY

in

Biochemistry and Molecular Biology

in the

GRADUATE DIVISION
of the
UNIVERSITY OF CALIFORNIA, SAN FRANCISCO

Approved:

DocuSigned by:
Natalia Jura
E438674A382B42F...

Natalia Jura
Chair

DocuSigned by:
Peter Walter
DocuSigned by:
E40D...

Peter Walter

Geeta Narlikar
EE2E6D32EE3043B...

Committee Members

Acknowledgements

Words cannot encompass how fortunate I am to have met the wide diversity of people who made a doctoral degree possible. I believe the work put forth in this dissertation is a perfect example of the benefits of collaboration and believe it only to have been possible as a collaborative effort between myself, my wonderful lab, generous collaborators, supportive thesis committee, and most of all, and my dedicated PI.

All of this would not have been possible without the unwavering support, patience, dedication and care of my PI, Natalia Jura. I will never be able to thank you enough for all of your kindness and mentorship and for all of the care you have taken in helping me grow as a scientist and as a person. I have learned countless lessons from you on becoming a better scientist, a more logical thinker and have always felt inspired by your perseverance, dedication and selflessness. I could not have picked a better mentor under whom to pursue my graduate studies and feel I have been extremely fortunate in having been able to learn from you. From you, I learned how to persevere and pick myself up through the myriad of challenges and hurdles that make up a graduate school education. You were always there for me through my biggest challenges, all of my successes and continued to motivate and inspire me. I feel truly fortunate to have had you as my guide, source of support and mentor.

My work thrived under the guidance and mentorship of my wonderful thesis committee. I am truly fortunate to have the privilege to learn from and spend time with two of the most passionate, driven scientists who formed part of my thesis committee: Peter Walter and Geeta Narlikar. Geeta, you always served as the logic behind some of best my work, always grounding my experiments and ideals, and instilled in me early to always keeps my mind open. Peter, you always encouraged me to think and dream big. You have inspired me more than you could ever

realize—from the first presentation I saw during my first year, throughout the rest of my graduate education. I know my project would not have taken some of the serendipitous turns it did without your tutelage, guidance and support, and I can't thank you enough for all you have done for me. You continually inspire me to be a better scientist and to strive to be the best person I can, and I am eternally grateful for everything you have done for me.

I cannot thank my lab enough for all of their support, friendship and camaraderie throughout the years. One of Natalia's greatest abilities has always been finding and recruiting strong scientists and wonderful people, and I am thankful I've learned from and grown with some of the most generous, kind people I have had the privilege to meet. Peter, Nicole, Chris, Jennifer, Lijun, Tarjani, Bettina, Michael, Megan, Mitch, Raphael, Devan, Ed and Erron: each and every one of you has changed my life and has made me a better scientist and a better friend. I can't imagine going through the many challenges and joys of graduate school without each and every one of you.

My graduate studies would not have been possible without the care and help of my family and the love, belief and support of my friends. I would like to thank my mom, Jaqueline, for her unwavering hard work during my youth, which allowed for me to value and acquire an education, and her determination and love which laid the foundation for me reach for my dreams of college and graduate school. To my siblings, Antonio, Ruby, and Victor: I would not be the same without your friendship and camaraderie, and I am thankful to have the three of you in my life. To my second mom Renata, thank you for always being my inspiration, mentor, guide and for always nurturing my growth. To my partner Tim: words will never be able to convey how much you mean to me, how much you have changed my life, or how happy and fortunate I am to share this journey

with you. Thank you for bringing immeasurable happiness into my life, for always believing in me, and for simultaneously inspiring me to dream bigger while keeping me grounded.

I am incredibly fortunate and thankful to have a truly wonderful classmates, who embarked on this remarkable journey with me, and with whom I shared the struggles and joys of graduate school. To my wonderful, kind, genuine, loving friends inside and outside of graduate school who have supported and shown me patience and care every day of this journey, and who always bring happiness to my life daily: Alejandra, Iliana, Nick, Justin, Joe, Karina, Efren, Kayla, Anna, Megan, Julia, Lina, Jose, Lianne and Maria. All of you continue to motivate me, and I am forever thankful to have you in my life.

While I feel a deep pang of sadness that the completion of this document marks the end of my graduate studies, I am excited and invigorated to continue my growth as a scientist and as a person with such a wonderful community of individuals who have made all of this possible.

Abstract

Cellular, structural and functional characterization of mitochondrial Phosphoglycerate Mutase 5

by

Karen P. Ruiz

This thesis examines multiple facets of the mitochondrial phosphatase Phosphoglycerate Mutase Family Member 5 (PGAM5), including its structure, function and mechanism of activation. The Phosphoglycerate mutase family, titled for its namesake phosphoglycerate Mutase (PGAM), is a family of enzymes able to catalyze the transfer of a phosphate group from 3-phosphoglycerate to 2-phosphoglycerate. Despite a conserved catalytic core and its classification into the PGAM family, PGAM5 lacks any detectable phosphoglycerate mutase activity and paradoxically possesses phosphatase activity.

PGAM5 is a mitochondrially localized serine, threonine and histidine phosphatase that is responsible for dephosphorylation of a wide variety of cytosolic protein substrates and has been identified as an interacting partner of multiple mitochondrial proteins. This mitochondrially-tethered protein has been implicated in progression of apoptosis, necrosis and mitophagy where it has been shown to promote cell death in response to oxidative stress or mitochondrial damage. In addition to its role in contributing to mitochondrial destruction and cell death, PGAM5 has been implicated in the regulation of mitochondrial fission. PGAM5's exact switch from a possible mitochondrial remodeler to a harbinger of death is still unknown, though preliminary data suggests

it may be tied to its cleavage and subsequent migration from the inner mitochondrial membrane (IMM) space to the cytosol.

When we embarked on this project in the Jura lab, the mechanism for regulation of PGAM5's phosphatase activity was poorly understood, and as a result, the tools for understanding the biological functions of PGAM5 or manipulating its activity did not exist. Using a wide variety of techniques, among these X-ray crystallography, electron cryo-microscopy, super-resolution microscopy and activity assays, we have observed PGAM5 is able to form higher order filaments in solution and in cells and succeeded in dissecting the dodecamer that comprises these rings and leads to PGAM5's activation as a phosphatase.

The first chapter of this thesis contains a brief introduction to PGAM5, including background information on the histidine phosphatase superfamily, of which the PGAM family of proteins is classified, the PGAM family itself and PGAM5's diverse roles in the cell. The second chapter of this thesis focuses on exploring the way in which PGAM5's phosphatase activity is regulated. In this chapter, we explore PGAM5's ability to form higher order structures, dissect these structures and unravel PGAM5's activation as a phosphatase. The third chapter focuses on our work to employ our newfound structural knowledge of PGAM5 in an effort to identify, test and optimize novel PGAM5 activators and inhibitors.

Table of contents

List of figures

Chapter 2:

List of tables

Chapter 2:

Chapter 3:

Chapter 1: Introduction

1.1 Phosphatases

A brief history of phosphatases

Phosphorylation, a powerful reversible post-translational modification of proteins, lipids and carbohydrates that governs signal propagation, exists in a delicate balance maintained by opposing kinases and phosphatases. Eukaryotic protein phosphorylation, well-established on serine, threonine, tyrosine residues and most recently identified on histidine residues, allows for the rapid, efficient control of a myriad of cellular processes. Dysregulation or dysfunction of either of these enzymes underlies many human diseases.

Despite performing equally important but opposite reactions, there exists a large difference in the number of eukaryotic kinases and phosphatases, their evolution and regulation, and ultimately, our knowledge and understanding of these two groups of proteins. With at least 550 known protein kinases, this family of proteins makes up a large percent of the human genome. While it is estimated that at least 200 phosphatases exist, a definitive number remains elusive; this numerical discrepancy between these families was initially interpreted to suggest phosphatases lacked substrate specificity and may less tightly regulated[1]. Further overarching distinctions separate these two groups that perform antithetical functions; while the structures of protein kinases and the basic mechanistic principles for their activation are generally conserved[2], protein phosphatases are more difficult to categorize using unifying criteria. This is due in large part to the fact that phosphatase activity is associated with a wide variety of protein folds and catalytic mechanisms, many of which have additional hydrolase activity or are found in nonenzymatic proteins; this is in sharp contrast to protein kinases, which have similar three dimensional structures whose catalytic domains arise predominantly from a single protein structural fold[3], and which adopt similar structures when active[4]. While significant progress has been made in

furthering our understanding of kinases, catalytically and structurally, our collective understanding of phosphatases is lacking.

Phosphatases: classical and atypical

Classical protein phosphatases have been categorized historically into two broad classes relative to their substrates into as (i) protein serine/ threonine phosphatases (PSPs), (ii) protein tyrosine phosphatases (PTPs) or (iii) dual-specificity phosphatases (DUSPs)[5]. These three broad groups have been further subclassified into 21 distinct families within their classes based on their chemical structures and have been shown to be able to adopt at least 10 distinct possible protein folds[3]. Despite best efforts to identify and organize these proteins, however, their study has been laborious and slow. Several factors have made studies on phosphatases especially challenging, among these: (i) the technical difficulty of generating phosphorylated substrate to probe for phosphatase activity, (ii) the transient nature of phosphatase and substrate interactions, (iii) the diversity in possible protein folds and (iv) the diversity of phosphatase active sites, which impedes general inhibitor design[6]. Further complicating their study, many phosphatases have been recently identified which do not conform to these classical phosphatase families due to differences in their structural and enzymatic features. These increasing numbers of atypical protein phosphatases have been implicated in the regulation of various critical physiological processes and present a shift in our understanding of these enzymes[7]. Among these atypical phosphatases, phosphoglycerate mutase family member 5 (PGAM5), a member of the Histidine phosphatase superfamily, has emerged as a multifaceted regulator of cell death, mitochondrial homeostasis and cell signaling.

Histidine phosphatase superfamily

While functionally diverse, the histidine phosphatase superfamily share a conserved catalytic core with a key histidine residue. During the course of the reaction, this essential histidine residue functions as a phosho-acceptor and becomes phosphorylated. The founding member of this superfamily is Phosphoglycerate Mutase, was identified as early as 1935[8], and the family has grown since to encapsulate two large branches, the majority of which are phosphatases involved a wide variety of regulatory roles. Perhaps ironically, the vast majority of this superfamily of enzymes has been found to possess phosphatase activity, while its founding member has become an anomaly with its mutase function[9].

The larger first branch of the family, clade-1, is functionally and sequentially diverse. Branch 1 has been identified as containing the PGAM family and various hydrolases and has been observed to have significant sequence diversity between members of the branch. In addition to functional and sequential diversity, the first branch of the family has been found to exist in a variety of cellular localizations, from cytoplasm to nucleus.

The second branch of the family, clade-2 is made up predominantly of acid phosphatases, proteins that hydrolyze phosphate esters at low pH, and phytases, proteins able to catalyze the hydrolysis of phytate to myo-inositol and inorganic phosphate. Despite a greater conservation in the enzyme type that characterizes branch 2 of the histidine phosphatase superfamily, branch 2 also possesses a high degree of sequence diversity. It has been found that the majority of branch 2 family proteins exist in various subcellular locations such as the endoplasmic reticulum or cell membrane while others have been found to be secreted; key to branch 2 proteins is their ability to enter the secretory pathway.

Despite a conserved catalytic core histidine residue, the two branches of the family share little sequence similarity to themselves and each other, making proper identification and organization of the families that comprise this family difficult. This difference between the branches is further exemplified in their structural differences.

Despite vast differences in protein sizes, roles and subcellular location, the catalytic mechanism for the members of the histidine phosphatase superfamily is conserved. Four largely invariant residues make up the catalytic core, three of which make up the characteristic RHG motif in the core. While the catalytic histidine is phosphorylated during the course of the reaction, the other three residues making up the RHG motif are able to form the 'phosphate pocket' and are able to electrostatically interact with the phospho group prior to, during and after its interaction with the central histidine during catalysis[9].

The Phosphoglycerate Mutase family

The phosphoglycerate mutase family, categorized in branch 1 of the histidine phosphatase superfamily, contains various metabolic enzymes that possess mutase activity on small molecule substrates. PGAM enzymes have been observed to typically function as phosphotransferases or phosphohydrolases of small metabolites[10], have recently been assigned to the histidine phosphatase superfamily[9] and were initially classified by their shared catalytic PGAM domain. The most well-characterized member of this family is its namesake, phosphoglycerate mutase, which is able to convert 3-phosphoglycerate (3PG) to 2-phosphoglycerate (2PG) during step 8 of glycolysis, where it is able to function as an isomerase. Many other members of this PGAM family have been observed to function as mutases in metabolic pathways where they serve to catalyze the transfer of a phosphate group from one position to another on the same substrate through the use

of a conserved phosphohistidine intermediate, a function which is dependent on the conserved histidine residue tucked in the PGAM domain. Interestingly enough, many of these family members have also been observed to for dimers[11].

Despite this family's placement in the histidine phosphatase superfamily and a its conservation of the central histidine residue that comprises the active site of these enzymes, many of these family members, with three exceptions, possess mutase activity. Despite the conservation of this core PGAM domain across the various members of the PGAM family of enzymes, three members of the PGAM family: Sts-1, Sts-2 and PGAM5, have been shown to lack observable mutase activity and instead been observed to dephosphorylate protein substrates. Although lacking any detectable mutase activity, PGAM5 was initially categorized as a member of the Phosphoglycerate Mutase (PGAM) family of enzymes that share the conserved PGAM domain despite lacking mutase activity. Similar to PGAM5, The Sts phosphatases have been observed to diverge from the rest of the PGAM family catalytically. Sts 1 and sts2 have been shown to be specific towards phosphorylated tyrosine residues[12], while PGAM5 was initially identified as possessing serine/ threonine phosphatase activity[13]. Most recently, PGAM5 has been shown to possess histidine phosphatase activity through its ability to dephosphorylate the catalytic histidine on cytosolic nucleoside diphosphatase kinase B (NDPK-B)[14] and remains one of the most perplexing members of the PGAM family.

1.2 Phosphoglycerate Mutase Family Member 5

Domain architecture of PGAM5 and its localization

Classified into the PGAM family, PGAM5 retains the canonical PGAM domain that characterizes this family of proteins, however, presents remarkable other differences that make it

novel and unique, among these its localization and mechanism of activation. PGAM5 is targeted to the mitochondria by an N-terminal mitochondrial targeting sequence (MS). The N-terminal mitochondrial targeting signal that anchors PGAM5 to the mitochondrial membrane is followed by a linker domain and the PGAM phosphatase domain. Initial studies by Wilkins and colleagues demonstrated that the linker domain greatly potentiates activity of the recombinant PGAM5 and identified a region within the linker domain responsible for the observed enhancement[15]. This region, termed the multimerization motif, also promoted higher-order oligomerization of the recombinant PGAM5 construct, which was composed of the linker and phosphatase domains. The importance of this motif is underscored by its conservation

In the absence of the linker domain, PGAM5 was unable to oligomerize and displayed minimal phosphatase activity. This work was seminal, as it functionally linked PGAM5's activity as a phosphatase to its ability to form an unknown oligomer. Within the mitochondria, PGAM5's exact localization is still debated. There is some evidence for PGAM5 localization to the Inner Mitochondrial Membrane (IMM)[16,17], while other data suggests PGAM5 can be found on the Outer Mitochondrial membrane (OMM) with its phosphatase domain accessible from the cytosol[18]. Localization of PGAM5 to the inner mitochondrial membranes is supported by the observation that PGAM5 is cleaved by at least two IMM-resident proteases: presenilins-associated rhomboid-like protein (PARL)[16] and the metalloprotease OMA1[19], generating a fragment of PGAM5 that lacks the transmembrane targeting sequence. PGAM5 cleavage occurs under conditions of mitochondrial stress, which is triggered either by the loss of mitochondrial membrane potential ($\Delta\psi_m$) upon treatment with carbonyl cyanide m-chlorophenyl hydrazine (CCCP)[16] or by inducers of apoptosis, such as staurosporin (STS) or actiomycin D[20,21]. Other studies have shown that following cleavage, a fraction of PGAM5 is released to the cytosol to engage in a number of

signaling functions[16,20-22]. Thus, it is possible that both localization patterns of PGAM5 are correct, as current data suggests that PGAM5's localization is dynamic and stress-responsive.

The various roles of PGAM5 in the cell

PGAM5 contributes to homeostasis through regulation of mitochondrial dynamics, respiration, mitophagy quality control and cell survival. PGAM5 was initially identified as a binding partner of KEAP1 and Bcl-xL[23]. As an adaptor protein for the Cul3-dependent E3 ubiquitin ligase complex, KEAP1 serves as a major sensor of oxidative stress by controlling ubiquitination and degradation of the NRF2 transcription factor. PGAM5 was shown to form a ternary complex with KEAP1 and NRF2 on the OMM, suppressing KEAP1 activity[18]. The functional role of this complex has also been linked to the regulation of Miro2, a mitochondrial GTPase that regulates retrograde transport of the mitochondria along microtubules[24].

PGAM5 also binds to the PTEN-induced kinase (PINK1), an important regulator of mitochondrial quality control[17,25]. PINK1 accumulates and dimerizes on damaged mitochondrial outer membranes, resulting in the recruitment of PARKIN and downstream initiation of mitophagy[26-29]. Although genetic studies in flies suggest a negative effect of PGAM5 on PINK1 signaling[25], studies in mice provide evidence that overwhelmingly supports the opposite effect[17]. The data in mice shows PGAM5 stabilizes PINK1 and promotes mitophagy as a protective measure against neuronal degeneration. Similar to the effect of PINK1 loss or kinase inactivating mutations on promoting neurodegeneration[30-33], loss of PGAM5 results in a Parkinson's disease-like phenotype caused by degeneration of dopaminergic neurons[17].

The involvement of PGAM5 in promoting mitophagy is corroborated by other studies. In response to hypoxia or loss of mitochondrial membrane potential, PGAM5 binds and

dephosphorylates FUNDC1, which promotes L3 binding and recruitment of autophagosomes to mitochondria[34]. This function of PGAM5 is negatively regulated through binding of BCL2L1, which inhibits PGAM5-dependent dephosphorylation of FUNDC1 and opposes mitophagy[35].

It has been observed that genetic knockout of PGAM5 in mice leads to a more severe Parkinson's disease-like phenotype than PINK1 knockout, suggesting that independent from the PINK1/ Parkin pathway, other functions of PGAM5 might be important for dopaminergic neuron survival. Regulation of mitochondrial motility through the stabilization of the KEAP1/ NRF2/ PGAM5 ternary complex is suggested to be one of these functions[24]. Other functions include a role for PGAM5 in metabolism. Genetic ablation of PGAM5 in the mouse causes resistance to high fat diet induced obesity linked to enhanced lipid uptake and utilization in the brown adipose tissue[36], as well as slight decrease in basal body weight[37]. These effects might be the result of a poorly understood role of PGAM5 in the regulation of mitochondrial morphology. PGAM5 overexpression results in visibly altered mitochondrial dynamics, such as perinuclear aggregation and fragmentation of the mitochondria[18]. Drastic changes in mitochondrial dynamics, such as rapid mitochondrial fission in brown adipocytes in response to adrenergic stimulation, was shown to promote energy expenditure[38]. More recent studies shown that PGAM5 is essential for the induction of FOXO-dependent transcription in response to the mitochondrial unfolded protein response in which PGAM5 exerts a protective effect on cells and contributes to organismal longevity[39].

Perhaps the least understood PGAM5 function is its role in the regulation of cell death[21,40,41]. In necroptosis, initiated by Tumor Necrosis Factor alpha (TNFα) and involving kinases RIP1, RIP3 and MLKL, PGAM5 was suggested to be a part of a RIP1 and RIP3 kinase complex promoting cell death[40]. Upon necrosis induction, PGAM5 was first proposed to recruit

and dephosphorylate the mitochondrial fission factor, DRP1, resulting in mitochondrial fragmentation, a necessary step to necroptosis[40]. However, the PGAM5/ DRP1 axis was later shown to be dispensable for TNFα-induced necroptosis by several other studies[42-44], with the exception of its function in hepatocytes where ConA-induced hepatic necrosis involves abnormal mitochondrial fission through the Drp1/ PGAM5 pathway[45]. In a different study, PGAM5 was also shown to be irrelevant to necroptosis, instead being involved in inflammation through promotion of inflammasomes and caspase 1 activation in macrophages[37]. PGAM5 was also shown to sensitize cells to apoptosis through binding of XIAP, a member of an IAP family of caspase inhibitors, and prevent XIAP from binding caspases[21]. This function of PGAM5 is linked to the release of its cleaved form into the cytosol. Adding to the complexity of the roles PGAM5 plays in regulating cell death, a recent study has shown that PGAM5 protects cells from necroptosis through its positive effect on PINK1-dependent mitophagy[46]. PGAM5's involvement in such a wide array of cellular processes, combined with its complex self-regulation and interesting cellular make it a compelling subject of study.

1.3 REFERENCES

1. Sacco F, Perfetto L, Castagnoli L, Cesareni G. The human phosphatase interactome: An intricate family portrait. FEBS letters. 2012; *586*(17), 2732–2739.
2. Kung JE, Jura N. Structural Basis for the Non-catalytic Functions of Protein Kinases. Structure. 2016;24(1):7–24.
3. Chen MJ, Dixon JE, Manning. Genomics and evolution of protein phosphatases. Science Signaling. 2017; 10: 474.
4. Endicott JA, Noble ME, Johnson LN. The Structural Basis for Control of Eukaryotic Protein Kinases. Annual Reviews. 2012; 81: 587-613.
5. Tomiyama A, Kobayashi T, Mori K, Ichimura K. Protein Phosphatases—A Touchy Enemy in the Battle Against Glioblastomas: A Review. *Cancers*. 2019; 11(2):241.
6. Shi, Y. (2009). Serine/Threonine Phosphatases: Mechanism through Structure. Cell, 139 (3) 468-484.
7. Sadatomi D, Tanimura S, Ozaki K, Takeda K. Atypical protein phosphatases: emerging players in cellular signaling. Int J Mol Sci. 2013;14(3):4596-612.
8. Meyerhof O, Kiessling W. Über die isolierung der isomeren phosphoglycerinsäuren (glycerinsäure-2-phosphorsäure und glycerinsäure-3-phosphorsäure) aus gäransätzen und ihr enzymatisches gleichgewicht.Biochem. Z. 1935. **276**:239–253.
9. Rigden DJ. The histidine phosphatase superfamily: structure and function. Biochem J. 2008;409(2):333-48.
10. Jedrzejas MJ. Structure, function, and evolution of phosphoglycerate mutases: comparison with fructose-2,6-bisphosphatase, acid phosphatase, and alkaline phosphatase. Prog Biophys Mol Biol. 2000;73(2-4):263-87.

11. Sakoda S, Shanske S, DiMauro S, Schon EA. Isolation of a cDNA encoding the B isozyme of human phosphoglycerate mutase (PGAM) and characterization of the PGAM gene family. The Journal of Biological Chemistry. 1988; 263(16899-16905).
12. Carpino N, Turner S, Mekala D, Takahashi Y, Zang H, Geiger TL, et al. Regulation of ZAP-70 activation and TCR signaling by two related proteins, Sts-1 and Sts-2. Immunity. 2004;20(1):37-46.
13. Takeda K, Komuro Y, Hayakawa T, Oguchi H, Ishida Y, Murakami S, et al. Mitochondrial phosphoglycerate mutase 5 uses alternate catalytic activity as a protein serine/threonine phosphatase to activate ASK1. Proc Natl Acad Sci U S A. 2009;106(30):12301-5.
14. Panda S, Srivastava S, Li Z, Vaeth M, Fuhs SR, Hunter T, et al. Identification of PGAM5 as a Mammalian Protein Histidine Phosphatase that Plays a Central Role to Negatively Regulate CD4(+) T Cells. Molecular cell. 2016;63(3):457-69.
15. Wilkins JM, McConnell C, Tipton PA, Hannink M. A conserved motif mediates both multimer formation and allosteric activation of phosphoglycerate mutase 5. The Journal of biological chemistry. 2014;289(36):25137-48.
16. Sekine S, Kanamaru Y, Koike M, Nishihara A, Okada M, Kinoshita H, et al. Rhomboid protease PARL mediates the mitochondrial membrane potential loss-induced cleavage of PGAM5. The Journal of biological chemistry. 2012;287(41):34635-45.
17. Lu W, Karuppagounder SS, Springer DA, Allen MD, Zheng L, Chao B, et al. Genetic deficiency of the mitochondrial protein PGAM5 causes a Parkinson's-like movement disorder. Nature communications. 2014;5:4930.
18. Lo SC, Hannink M. PGAM5 tethers a ternary complex containing Keap1 and Nrf2 to mitochondria. Experimental cell research. 2008;314(8):1789-803.

19. Wai T, Saita S, Nolte H, Muller S, Konig T, Richter-Dennerlein R, et al. The membrane scaffold SLP2 anchors a proteolytic hub in mitochondria containing PARL and the i-AAA protease YME1L. EMBO Rep. 2016;17(12):1844-56.
20. Saita S, Nolte H, Fiedler KU, Kashkar H, Venne AS, Zahedi RP, et al. PARL mediates Smac proteolytic maturation in mitochondria to promote apoptosis. Nature cell biology. 2017;19(4):318-28.
21. Zhuang M, Guan S, Wang H, Burlingame AL, Wells JA. Substrates of IAP ubiquitin ligases identified with a designed orthogonal E3 ligase, the NEDDylator. Molecular cell. 2013;49(2):273-82.
22. Bernkopf DB, Jalal K, Bruckner M, Knaup KX, Gentzel M, Schambony A, et al. Pgam5 released from damaged mitochondria induces mitochondrial biogenesis via Wnt signaling. J Cell Biol. 2018.
23. Lo SC, Hannink M. PGAM5, a Bcl-XL-interacting protein, is a novel substrate for the redox-regulated Keap1-dependent ubiquitin ligase complex. The Journal of biological chemistry. 2006;281(49):37893-903.
24. O'Mealey GB, Plafker KS, Berry WL, Janknecht R, Chan JY, Plafker SM. A PGAM5-KEAP1-Nrf2 complex is required for stress-induced mitochondrial retrograde trafficking. J Cell Sci. 2017.
25. Imai Y, Kanao T, Sawada T, Kobayashi Y, Moriwaki Y, Ishida Y, et al. The loss of PGAM5 suppresses the mitochondrial degeneration caused by inactivation of PINK1 in Drosophila. PLoS genetics. 2010;6(12):e1001229.

26. Matsuda N, Sato S, Shiba K, Okatsu K, Saisho K, Gautier CA, et al. PINK1 stabilized by mitochondrial depolarization recruits Parkin to damaged mitochondria and activates latent Parkin for mitophagy. J Cell Biol. 2010;189(2):211-21.
27. Vives-Bauza C, Zhou C, Huang Y, Cui M, de Vries RL, Kim J, et al. PINK1-dependent recruitment of Parkin to mitochondria in mitophagy. Proc Natl Acad Sci U S A. 2010;107(1):378-83.
28. Geisler S, Holmstrom KM, Skujat D, Fiesel FC, Rothfuss OC, Kahle PJ, et al. PINK1/Parkin-mediated mitophagy is dependent on VDAC1 and p62/SQSTM1. Nature cell biology. 2010;12(2):119-31.
29. Narendra DP, Jin SM, Tanaka A, Suen DF, Gautier CA, Shen J, et al. PINK1 is selectively stabilized on impaired mitochondria to activate Parkin. PLoS Biol. 2010;8(1):e1000298.
30. Gispert S, Ricciardi F, Kurz A, Azizov M, Hoepken HH, Becker D, et al. Parkinson phenotype in aged PINK1-deficient mice is accompanied by progressive mitochondrial dysfunction in absence of neurodegeneration. PLoS One. 2009;4(6):e5777.
31. Glasl L, Kloos K, Giesert F, Roethig A, Di Benedetto B, Kuhn R, et al. Pink1-deficiency in mice impairs gait, olfaction and serotonergic innervation of the olfactory bulb. Experimental neurology. 2012;235(1):214-27.
32. Kitada T, Pisani A, Porter DR, Yamaguchi H, Tscherter A, Martella G, et al. Impaired dopamine release and synaptic plasticity in the striatum of PINK1-deficient mice. Proc Natl Acad Sci U S A. 2007;104(27):11441-6.
33. Valente EM, Abou-Sleiman PM, Caputo V, Muqit MM, Harvey K, Gispert S, et al. Hereditary early-onset Parkinson's disease caused by mutations in PINK1. Science. 2004;304(5674):1158-60.

34. Chen G, Han Z, Feng D, Chen Y, Chen L, Wu H, et al. A regulatory signaling loop comprising the PGAM5 phosphatase and CK2 controls receptor-mediated mitophagy. Molecular cell. 2014;54(3):362-77.
35. Wu H, Xue D, Chen G, Han Z, Huang L, Zhu C, et al. The BCL2L1 and PGAM5 axis defines hypoxia-induced receptor-mediated mitophagy. Autophagy. 2014;10(10):1712-25.
36. Sekine S, Yao A, Hattori K, Sugawara S, Naguro I, Koike M, et al. The Ablation of Mitochondrial Protein Phosphatase Pgam5 Confers Resistance Against Metabolic Stress. EBioMedicine. 2016;5:82-92.
37. Moriwaki K, Farias Luz N, Balaji S, De Rosa MJ, O'Donnell CL, Gough PJ, et al. The Mitochondrial Phosphatase PGAM5 Is Dispensable for Necroptosis but Promotes Inflammasome Activation in Macrophages. J Immunol. 2016;196(1):407-15.
38. Wikstrom JD, Mahdaviani K, Liesa M, Sereda SB, Si Y, Las G, et al. Hormone-induced mitochondrial fission is utilized by brown adipocytes as an amplification pathway for energy expenditure. The EMBO journal. 2014;33(5):418-36.
39. Borch Jensen M, Qi Y, Riley R, Rabkina L, Jasper H. PGAM5 promotes lasting FoxO activation after developmental mitochondrial stress and extends lifespan in Drosophila. Elife. 2017;6.
40. Wang Z, Jiang H, Chen S, Du F, Wang X. The mitochondrial phosphatase PGAM5 functions at the convergence point of multiple necrotic death pathways. Cell. 2012;148(1-2):228-43.
41. Ishida Y, Sekine Y, Oguchi H, Chihara T, Miura M, Ichijo H, et al. Prevention of apoptosis by mitochondrial phosphatase PGAM5 in the mushroom body is crucial for heat shock resistance in Drosophila melanogaster. PLoS One. 2012;7(2):e30265.

42. Murphy JM, Czabotar PE, Hildebrand JM, Lucet IS, Zhang JG, Alvarez-Diaz S, et al. The pseudokinase MLKL mediates necroptosis via a molecular switch mechanism. Immunity. 2013;39(3):443-53.
43. Remijsen Q, Goossens V, Grootjans S, Van den Haute C, Vanlangenakker N, Dondelinger Y, et al. Depletion of RIPK3 or MLKL blocks TNF-driven necroptosis and switches towards a delayed RIPK1 kinase-dependent apoptosis. Cell Death Dis. 2014;5:e1004.
44. Moujalled DM, Cook WD, Murphy JM, Vaux DL. Necroptosis induced by RIPK3 requires MLKL but not Drp1. Cell Death Dis. 2014;5:e1086.
45. He GW, Gunther C, Kremer AE, Thonn V, Amann K, Poremba C, et al. PGAM5-mediated programmed necrosis of hepatocytes drives acute liver injury. Gut. 2017;66(4):716-23.
46. Lu W, Sun J, Yoon JS, Zhang Y, Zheng L, Murphy E, et al. Mitochondrial Protein PGAM5 Regulates Mitophagic Protection against Cell Necroptosis. PLoS One. 2016;11(1):e0147792.

Chapter 2: Functional role of PGAM5 multimeric assemblies and their polymerization into filaments

This chapter contains a reprint of "Functional role of PGAM5 multimeric assemblies and their polymerization into filaments", published in Nature Communications on January 31, 2019.

Author contributions are as follows: Karen Ruiz developed the project, expressed, optimized and purified each of the protein constructs, performed cell-based confocal, SIM and STED imaging, X-ray crystallography, titration experiments and analysis and contributed to paper writing. Tarjani M. Thaker acquired negative stain images, conducted Cryo-EM data acquisition and processing, performed Blue Native-PAGE experiments, and contributed to developing the project and paper writing. Christopher Agnew helped with X-ray crystallography data acquisition, processing and deposition. Maria Ingaramo assisted with STED training and data acquisition. Raphael Trenker performed kinetics experiments. Natalia Jura contributed to the project development, data analysis and paper writing.

2.1 ABSTRACT

PGAM5 is a mitochondrial protein phosphatase whose genetic ablation in mice results in mitochondria-related disorders, including neurodegeneration. Functions of PGAM5 include regulation of mitophagy, cell death, metabolism and aging. However, mechanisms regulating PGAM5 activation and signaling are poorly understood. Using electron cryo-microscopy, we showed that PGAM5 forms dodecamers in solution. We also present a crystal structure of PGAM5 that reveals the determinants of dodecamer formation. Furthermore, we observed PGAM5 dodecamer assembly into filaments both *in vitro* and in cells. We found that PGAM5 oligomerization into a dodecamer is not only essential for catalytic activation, but this form also plays a structural role on mitochondrial membranes, which is independent of phosphatase activity. Together, these findings suggest that modulation of the oligomerization of PGAM5 may be a regulatory switch of potential therapeutic interest.

2.2 INTRODUCTION

Phosphoglycerate mutase family member 5 (PGAM5) is an atypical protein phosphatase implicated in a number of functions within mitochondria, including organelle homeostasis, mitophagy and cell death. As a member of the PGAM histidine phosphatase superfamily, PGAM5 has the conserved PGAM domain[1]. However, unlike most PGAM enzymes, which are phosphotransferases or phosphohydrolases of small metabolites, PGAM5 dephosphorylates protein substrates[2], targeting phosphorylated serine, threonine, and histidine residues[3,4]. PGAM5 contains an N-terminal mitochondrial targeting sequence (MTS), which also serves as a membrane anchor. Experimental evidence supports PGAM5 localization to the outer mitochondrial membrane (OMM), where its phosphatase domain is accessible from both the cytosol[5] and the inner mitochondrial membrane (IMM)[6,7]. In response to loss of mitochondrial membrane potential ($\Delta\psi_m$)[6] or apoptosis[8,9], PGAM5 undergoes cleavage by two IMM-resident proteases, presenilin-associated rhomboid-like protein (PARL)[6] and the metalloprotease OMA1[10], generating a fragment of PGAM5 missing the MTS (Fig. 2.1a) that can be partially released into the cytosol[6,8,9,11]. Thus, the localization of PGAM5 seems dynamic and stress responsive.

PGAM5 has been linked to mitochondrial homeostasis and cell death through the regulation of mitochondrial dynamics, respiration and mitophagic quality control. Interaction partners of PGAM5 include KEAP1, an adaptor protein for the Cul3-dependent E3 ubiquitin ligase complex, and Bcl-XL, an anti-apoptotic protein[12]. By inhibiting KEAP1 activity[5], PGAM5 promotes retrograde transport of mitochondria along microtubules by the GTPase Miro2[13]. PGAM5 also regulates levels of PTEN-induced kinase 1 (PINK1), a guardian of mitochondrial quality control[7,14], which upon mitochondrial damage accumulates on the cytosolic surface of mitochondria to recruit Parkin and initiate mitophagy[15-18]. In mice, PGAM5 stabilizes PINK1 and

promotes mitophagy to protect against neuronal degeneration[7], whereas in flies PGAM5 negatively regulates PINK1[14]. In response to hypoxia or loss of mitochondrial membrane potential, PGAM5 binds and dephosphorylates FUNDC1, promoting recruitment of autophagosomes to mitochondria[19], consistent with PGAM5's role in promotion of mitophagy. Notably, PGAM5 knockout in mice leads to a more severe Parkinson's disease-like phenotype than observed for PINK1 knockout, suggesting that PGAM5 has multiple functions that support dopaminergic neuron survival[7,20-23].

The role of PGAM5 in cell death is poorly understood [9,24,25]. In necroptosis, initiated by Tumor Necrosis Factor alpha (TNFα), PGAM5 may be a part of a complex with the kinases RIP1 and RIP3 that promotes cell death through dephosphorylation of the mitochondrial fission factor DRP1[24]. However, the PGAM5/DRP1 axis is dispensable for TNFα-induced necroptosis in many cells and conditions[26-29], except for ConA-induced hepatic necrosis[30]. Other studies link PGAM5 to apoptosis through sequestration of a caspase inhibitor, XIAP E3 ubiquitin ligase[9]. During apoptosis, PGAM5 also contributes to mitochondrial recruitment of Bax and to DRP1 dephosphorylation, possibly be engaging them in a heteromeric complex[31]. Most recently, PGAM5 was shown to protect cells from necroptosis through its positive effect on PINK1-dependent mitophagy[32].

Biochemical and structural studies elude to an elaborate mechanism by which many functions of PGAM5 might be controlled. Between the MTS and phosphatase domain, PGAM5 contains a linker domain (Fig. 2.1a) with a centrally located "multimerization motif" that potentiates PGAM5 activity[33]. The multimerization motif also promotes higher-order oligomerization of PGAM5[33]. A crystal structure of PGAM5 containing the linker and phosphatase domains showed that the multimerization motif stabilizes a catalytically active conformation of

the enzyme[34]. The structure also revealed a dodecameric, ring-shaped organization of the phosphatase domain in the crystal lattice[34], of unknown physiological relevance.

Here, we provide evidence that oligomerization is essential for PGAM5 catalysis and present a new crystal structure of the PGAM5 ring demonstrating the sufficiency of the multimerization motif for PGAM5 dodecamer formation. We also discover that PGAM5 can adopt different oligomeric states in solution, including filamentous structures composed of stacked dodecameric rings that can form both *in vitro* and in cells. Lastly, we find that PGAM5 oligomerization exerts a structural effect on mitochondrial membranes that is independent of its phosphatase activity. Taken together, we propose that the functions of this atypical phosphatase are regulated through both catalytic and non-catalytic mechanisms.

2.3 RESULTS

Linker domain induces filamentation of the PGAM5 phosphatase

To understand the mechanism of oligomerization-dependent activation of PGAM5, we purified a truncated form of PGAM5 (Δ48 PGAM5), previously characterized as a stable and fully active construct, which includes the multimerization motif (residues 58 – 63) (Fig. 2.1a)[33]. We focused on the form of PGAM5, known as PGAM5L, that has an intact PGAM domain formed by residues 98-289. Δ48 PGAM5 resolved as two distinct peaks during size exclusion chromatography (Fig. 2.1b). The later peak was consistent with the profile expected for a dimeric complex of PGAM5, similar to the elution observed for the isolated phosphatase domain (Δ90 PGAM5)[33] (Fig. 2.1b). The earlier peak, however, was consistent with a larger oligomer that has been observed in biochemical preparations of a comparable construct, Δ54 PGAM5[33,34].

Analysis of both chromatogram peaks using negative-stain electron microscopy (EM) revealed the presence of spontaneously formed filaments of several hundred nanometers in the earlier peak. These filaments were not observed in purified samples of PGAM5 dimers (Δ48 later peak or Δ90 PGAM5) (Fig. 2.1c). Filaments were comprised of a repeating unit with an occasional shift in register along the length of the filament. In addition, singular ring-like particles frequently decorated the ends of the filaments in an orientation perpendicular to the filament axis. We hypothesized that the filaments are comprised of individual rings, with the lumen of the ring forming the interior of the filament. The lack of isolated rings within either sample suggests that PGAM5 oligomerization into filaments is a cooperative process.

The presence of rings and their potential role as the building blocks of PGAM5 filaments was intriguing, especially in light of a recent crystal structure of Δ54 PGAM5, which revealed a ring-like oligomer through lattice interactions between 12 copies of PGAM5 (PDB: 5MUF)[34]. Δ48

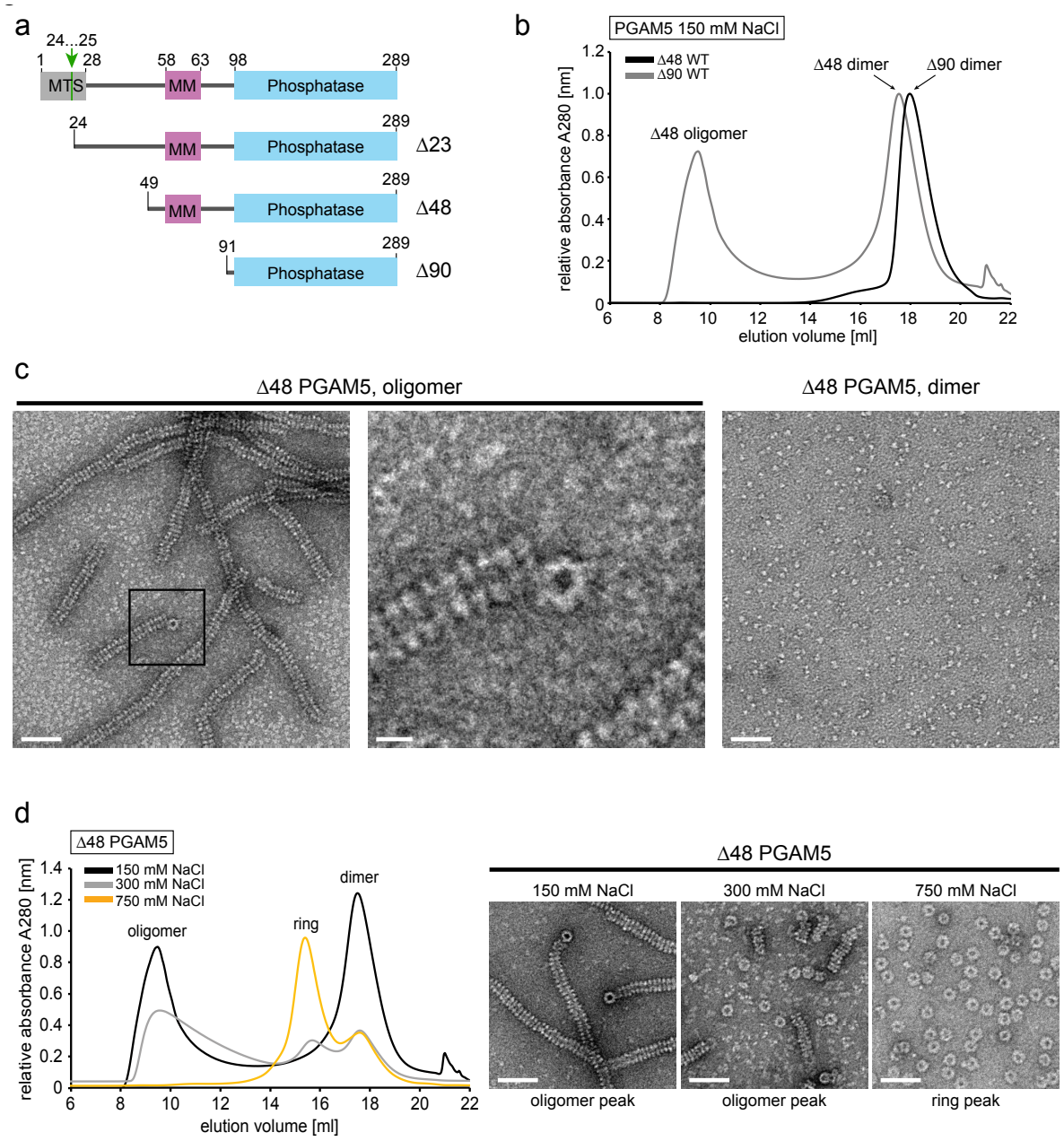

Fig. 2.1: Δ48 PGAM5 forms tubular filaments in solution composed of ring-like structures. **a.** Domain architecture of constructs used in this study. Full-length PGAM5 is comprised of a single transmembrane helix containing a mitochondrial targeting sequence (MTS), a linker domain including the regulatory multimerization motif (MM), and a C-terminal PGAM phosphatase domain. The native cleavage site between residues 24 and 25, cleaved by PARL[6], is marked with a green arrow. **b.** Elution profiles for Δ48 and Δ90 PGAM5 constructs purified by size exclusion chromatography (SEC) using a Superose 6 column (GE Healthcare) in buffer containing 150 mM NaCl. The corresponding oligomeric states of each peak observed in the chromatograms are indicated. **c.** Representative EM micrographs of negatively-stained protein samples taken from fractions corresponding to the two distinct peaks observed in the Δ48 PGAM5 purification. **d.** SEC profiles for Δ48 PGAM5 in buffer containing 20 mM Tris-Cl pH 8.0, 500 µM TCEP, and NaCl at a final concentration of 150 mM, 300 mM, or 750 mM. EM micrographs of negatively-stained

samples of Δ48 PGAM5 taken directly from the primary peak observed during purification are shown, highlighting the decomposition of filaments into rings at increasing salt concentrations. Scale bars in (c) and (d) correspond to 50 nm, except for the inset in (c) in which the scale bar corresponds to 10 nm.

PGAM5 filaments could be dissociated into rings by increasing the ionic strength during purification (Fig. 2.1d). With high concentrations of NaCl (>500 mM NaCl), we could enrich for discrete PGAM5 rings, enabling structural analyses on the ring-like Δ48 PGAM5 state in solution.

PGAM5 rings in solution and in a new crystal structure

We assessed the molecular structure of Δ48 PGAM5 rings in solution by cryo-EM. Our data revealed a mixture of PGAM5 ring particles with dimensions consistent with the formation of single rings, a doublet of rings, and less frequently, partial doublets (Fig. 2.2). The particles adopted a preferred orientation in the vitreous layer that limited the number of side views necessary for complete 3D reconstruction. Thus, we performed 2D classification of the top view of the Δ48 PGAM5 ring, visualized along the central symmetry axis, revealing features of PGAM5 at a resolution sufficient to analyze its organization (Fig. 2.3a). The solution structure of Δ48 PGAM5 adopted C6 symmetry in which six phosphatase domain dimers form a ring. Comparison of the best 2D class of the Δ48 PGAM5 ring to a projection image of the crystallographic ring observed in the structure of Δ54 PGAM5[34] (filtered to 4.5 Å resolution) showed similar ring architectures (Fig. 2.3b). Despite slightly different dimensions, stemming from the crystallographic symmetry of the Δ54 PGAM5 structure (Fig. 2.4a-d), the overall similarity in ring architecture verified that the dodecameric assembly of PGAM5 in the crystalline lattice of the Δ54 PGAM5 structure also occurs in solution.

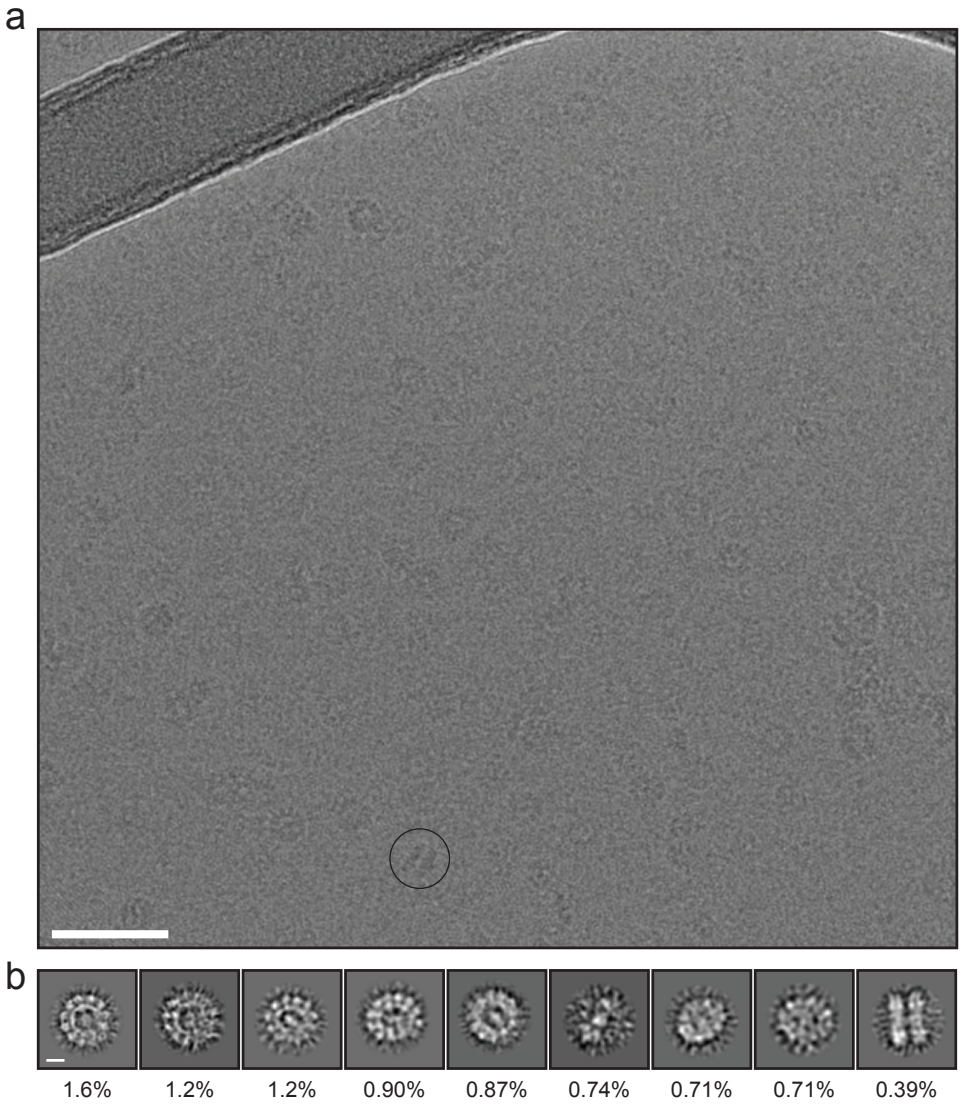

Fig. 2.2: Representative electron cryo-micrograph and 2D class averages of Δ48 PGAM5 dodecamer side views. a. Representative raw micrograph image of Δ48 PGAM5, with a representative side view of a dodecamer doublet circled on the image. The scale bar in **(a)** corresponds to 50 nm. **b.** Approximately 8.3% of the total number of particles picked from 6,543 micrographs corresponded to orientations other than the C6 symmetry 'top' view of the dodecamer and were subject to iterative rounds of 2D-classification into 9 classes as described in the methods section of the main text, revealing a single class in which the side view of a doublet of dodecamers stacked on the apparent planar face of the assembly (class 9 comprised of 542 particles) is observed. The scale bar in **(b)** corresponds to 5 nm.

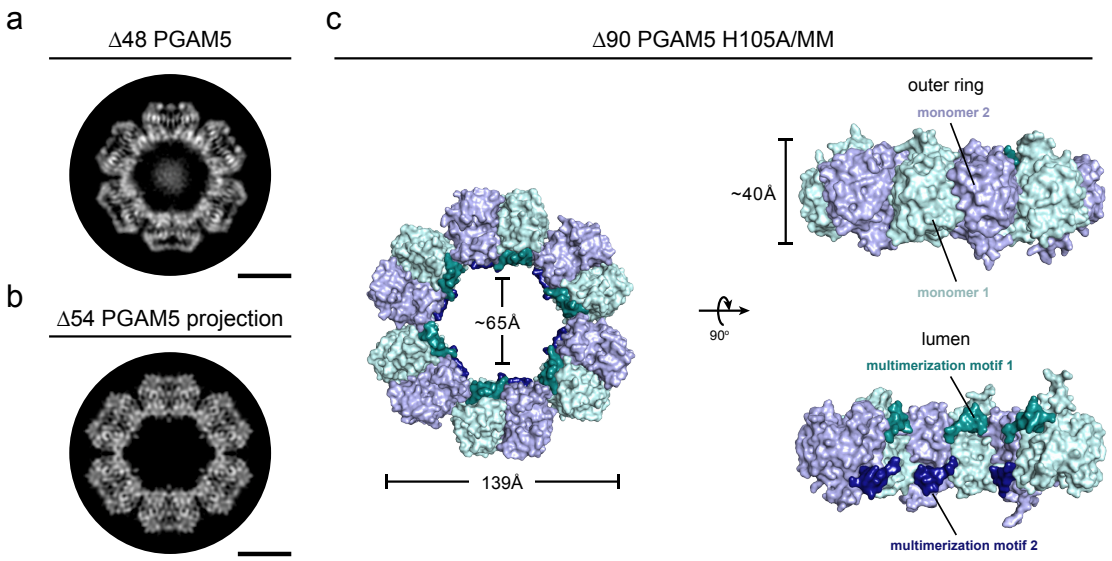

Fig. 2.3: Architecture of the PGAM5 dodecameric ring in solution and in a new crystal structure. a. 2D class average of the predominant view of the ring assembly observed in cryo-EM micrographs of Δ48 PGAM5 reveals a dodecameric topology highly similar in architecture to (b). **b.** 2D projection image of the crystallographic ring observed in the crystal lattice of the Δ54 PGAM5 dimer (PDB: 5MUF) limited to 4.5 Å resolution. **c.** Architecture and subunit arrangement of the dodecameric assembly observed in the crystal structure of the Δ90 PGAM5 H105A phosphatase domain crystallized in the presence of the peptide containing the multimerization motif (MM).

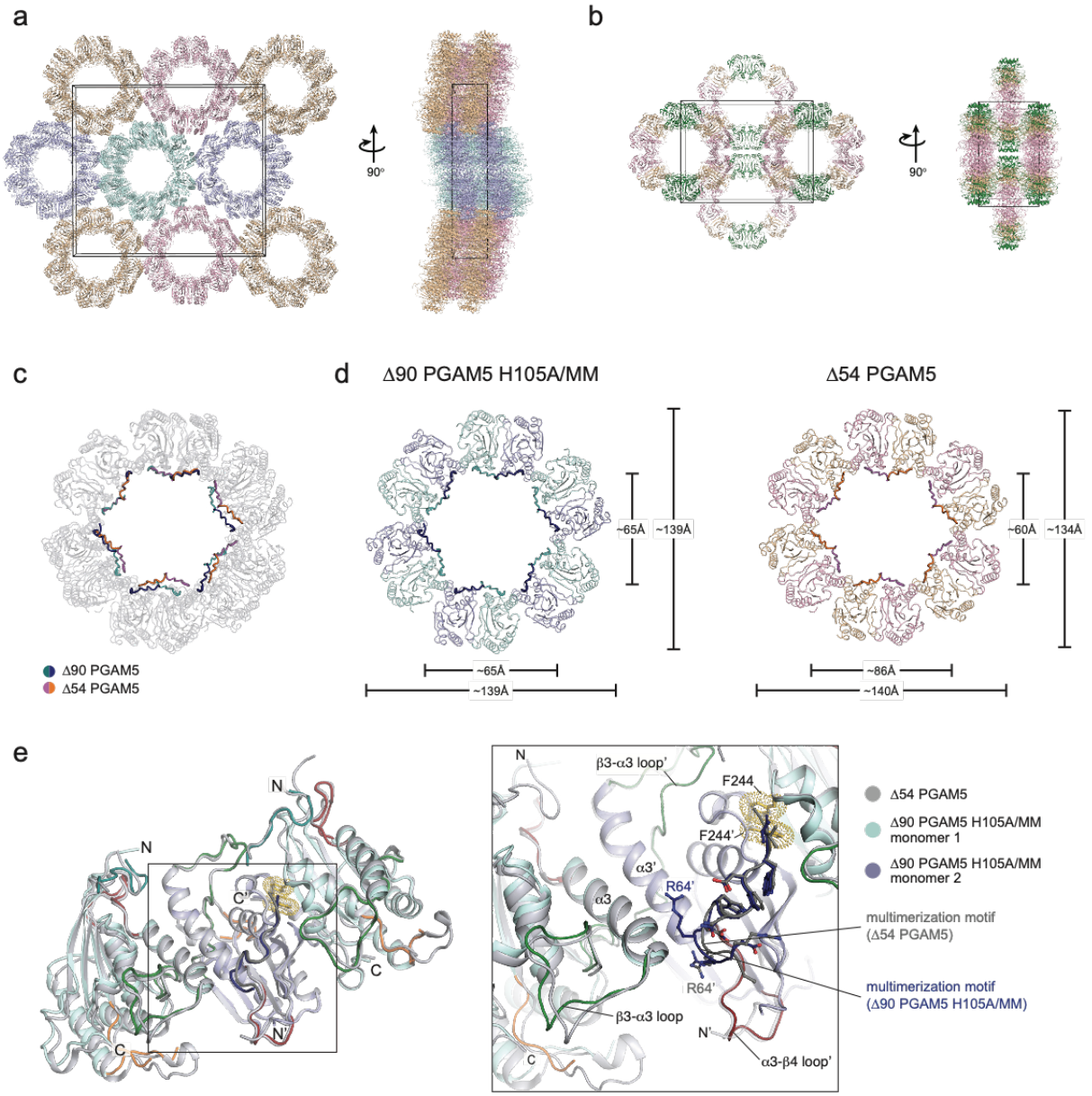

Fig. 2.4: Overview of dodecamer geometry in Δ90 PGAM5 H105A/MM compared to Δ54 PGAM5. Comparison of crystal packing in the structures of **a.** Δ90 PGAM5 H105A/MM and **b.** Δ54 PGAM5 (PDB: 5MUF). Molecules related by symmetry are colored the same in the respective lattices. **c.** Overlay of the dodecameric assemblies of Δ90 PGAM5 H105A/MM and Δ54 PGAM5, highlighting the differences in the geometry of the dodecamer lumen. **d.** Comparison of dodecamer dimensions in Δ90 PGAM5 H105A/MM (left panel) and Δ54 PGAM5 (right panel). **e** Differences in the dimerization interface mediated by the α3 helices of two adjacent phosphatase domains are highlighted in the structures of Δ54 PGAM5 (grey) and Δ90 PGAM5 H105A/MM colored using the same color scheme as shown in Fig. 2.2 (monomer 1 in cyan; monomer 2 in light blue). A detailed view of the interface and residues within the multimerization motifs in the monomer 1 in both structures are shown as stick representation in the panel on the right.

In the Δ54 PGAM5 crystal structure, the linker domain is mostly disordered, except for a region corresponding to the multimerization motif[34]. Similarly, we could not clearly identify the linker domain in 2D classes of the Δ48 PGAM5 ring (Fig. 2.3a). These observations suggested that the interactions supported by the multimerization motif might be sufficient to drive oligomerization and activation of PGAM5. This model is supported by a crystal structure we determined for a shorter fragment of a catalytically dead PGAM5 phosphatase domain (Δ90 PGAM5 H105A), in complex with a peptide encompassing the multimerization motif (linker domain residues 54 – 67, denoted as MM) (Table 2.1, 2.3c). The asymmetric unit of the unit cell in our 2.6 Å resolution structure of Δ90 PGAM5 H105A/MM revealed organization of the phosphatase domain into a dodecameric ring, with the multimerization motif peptide positioned in the lumen of the ring at the base of each phosphatase domain (Fig. 2.3c). Hence, our structure demonstrates that the multimerization motif is sufficient to induce the formation of a dodecameric PGAM5 ring, even when presented *in trans*.

The active conformation is independent of phosphate binding

The dodecameric ring in the crystal structure of Δ90 PGAM5 H105A/MM has a central 6-fold symmetry axis that better matches the C6 symmetry of the 2D class of the Δ48 PGAM5 ring than the C2 symmetry of the Δ54 PGAM5 crystallographic dodecamer (Fig. 2.3b). The differences between the two ring geometries stem from a slight rotation of the PGAM5 phosphatase monomers at the α3 helical interface; whereas the dimer interface-flanking residues F244 and burying approximately 1050.5 $Å^2$ through hydrophobic interactions is the same in both structures (Fig. 2.4e). Despite the differences, the ordered β3-α3 catalytic loop (residues 172 – 193) indicated that the phosphatase domain in both structures is in the active conformation (Fig. 2.5a). A notable

difference between the Δ54 PGAM5 structure and the Δ90 PGAM5 H105A/MM structure occurred in the β1-α1 loop (residues 105 – 121). In the Δ54 PGAM5 structure, this loop is ordered, whereas it is missing in the Δ90 PGAM5 H105A/MM dodecamer. This difference could be due to the engagement of the β1-α1 loop in crystal contacts in the Δ54 PGAM5 structure, but not in the Δ90 PGAM5 H105A/MM structure.

Mutation of the catalytic histidine (H105) to alanine resulted in active-site arrangements in our ring structure of Δ90 PGAM5 resembling an active state described as the PO4 'on' conformation in the Δ54 PGAM5 structure[34] (Fig. 2.5b, left and right panels). In this on state, the H230 residue is positioned inward relative to its position in the structure of the inactive phosphatase domain alone (Δ90 PGAM5 (PDB:3MXO); Fig. 2.5b, center panel). In the Δ54 PGAM5 structure residue R152 adopts a vertical, rather than the planar position observed in the Δ90 PGAM5 dimer structure[34], forming cation-π–stacking interactions with Y108, and together with H230 and H105, coordinates an active site phosphate (Fig. 2.5b, right panel). In the Δ90 PGAM5 H105A/MM structure, residues R152, Y108 and H230 adopt similar orientations, but in the absence of phosphate (Fig. 2.5b, left panel). The on state observed for Δ90 PGAM5 H105A/MM in the absence of bound phosphate underscores the importance of ring assembly for stabilizing the active architecture of the catalytic site.

Table 2.1: Data collection and refinement statistics.

	Δ90 PGAM5 H105A/MM	Δ90 PGAM5 H105A
Data collection		
PDB ID	6CNL	6CNI
Space group	P 2_1 2_1 2_1	P 2_1 2_1 2_1
Cell dimensions		
a, *b*, *c* (Å)	49.4, 242.5, 272.5	71.0, 72.0, 81.9
α, β, γ (°)	90, 90, 90	90, 90, 90
Resolution (Å)	48.6 – 2.6 (2.69 – 2.6)	41.0 – 1.7 (1.76 – 1.7)
R_{sym} or R_{merge}	19.8 (105.8)	7.5 (76.0)
$I / \sigma I$	7.2 (1.4)	21.8 (2.3)
Completeness (%)	99.8 (99.9)	99.7 (97.5)
Redundancy	5.0 (5.1)	12.1 (7.8)
Refinement		
Resolution (Å)	48.6 – 2.6 (2.69 – 2.6)	41.0 – 1.7 (1.76 – 1.7)
No. reflections	509,660 (51,383)	564,588 (35,185)
R_{work} / R_{free} %	22.3/26.4 (30.9/33.6)	17.1/19.7 (25.9/31.3)
No. atoms		
Protein	18,643	2,893
Ligand/ion	31	16
Water	199	308
B-factors		
Protein	35.5	26.2
Ligand/ion	30.5	25.8
Water	31.8	37.4
R.m.s. deviations		
Bond lengths (Å)	0.004	0.007
Bond angles (°)	0.8	1.1
Ramachandran plot %		
Favored	97.8	99.4
Additional allowed	2.2	0.00

Values in parentheses are for highest-resolution shell.

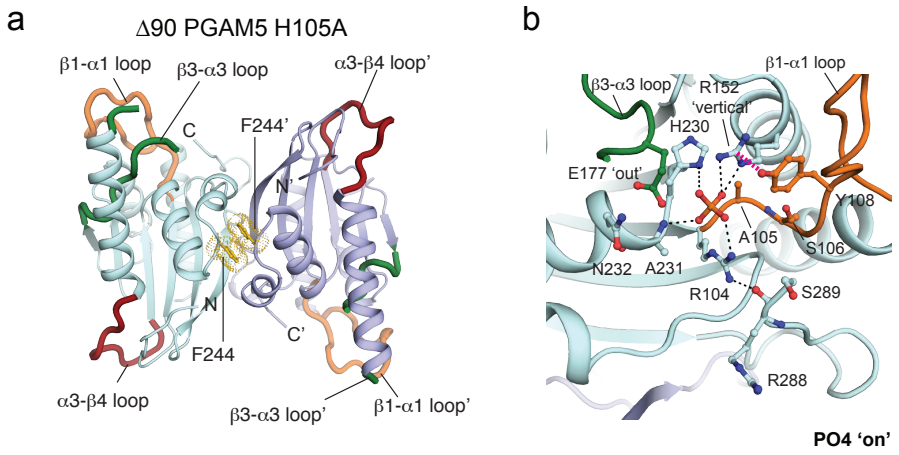

Fig. 2.5: Active site in the crystal structure of the Δ90 PGAM5 H105A phosphatase. **a.** The cartoon representation of the crystal structure of the Δ90 PGAM5 H105A phosphatase is shown using the same color assignment as in Fig. 2.3, with monomers 1 and 2 shown in cyan and light blue, respectively. The β1-α1 loops are colored in orange, the β3-α3 loops are colored in green, the α3-β4 loops are colored in red. The F244 residues in the constitutive dimer interface are colored in yellow. **b.** Detailed view of the residue positions in the active site in the crystal structure of the Δ90 PGAM5 H105A phosphatase depicting the coordination of a phosphate ion (PO4 'on').

Chaikuad and colleagues suggested that capping of the active site by the β3-α3 loop positions active site residues in the catalytically competent state[34]. However, a crystal structure of Δ90 PGAM5 H105A without the multimerization motif that we determined suggests otherwise (Table 2.1, Fig. 2.6). In this structure, PGAM5 phosphatase formed a dimer analogous to the one previously observed in the structure of Δ90 PGAM5 wild type (PDB:3MXO). Although the crystal packing was identical in the two Δ90 PGAM5 structures, the active site residues of Δ90 PGAM5 H105A adopted catalytically competent conformations (PO4 'on') in the presence of a phosphate ion (Fig. 2.6b). The main difference between this dimer conformation and the apo 'on' state of the dodecameric Δ90 PGAM5 H105A/MM structure was a disordered β3-α3 loop in Δ90 PGAM5 H105A. Thus, in the absence of discrete phosphatase domain interactions with the β3-α3 loop, the active architecture can be achieved, at least structurally, as long as a phosphate ion is coordinated.

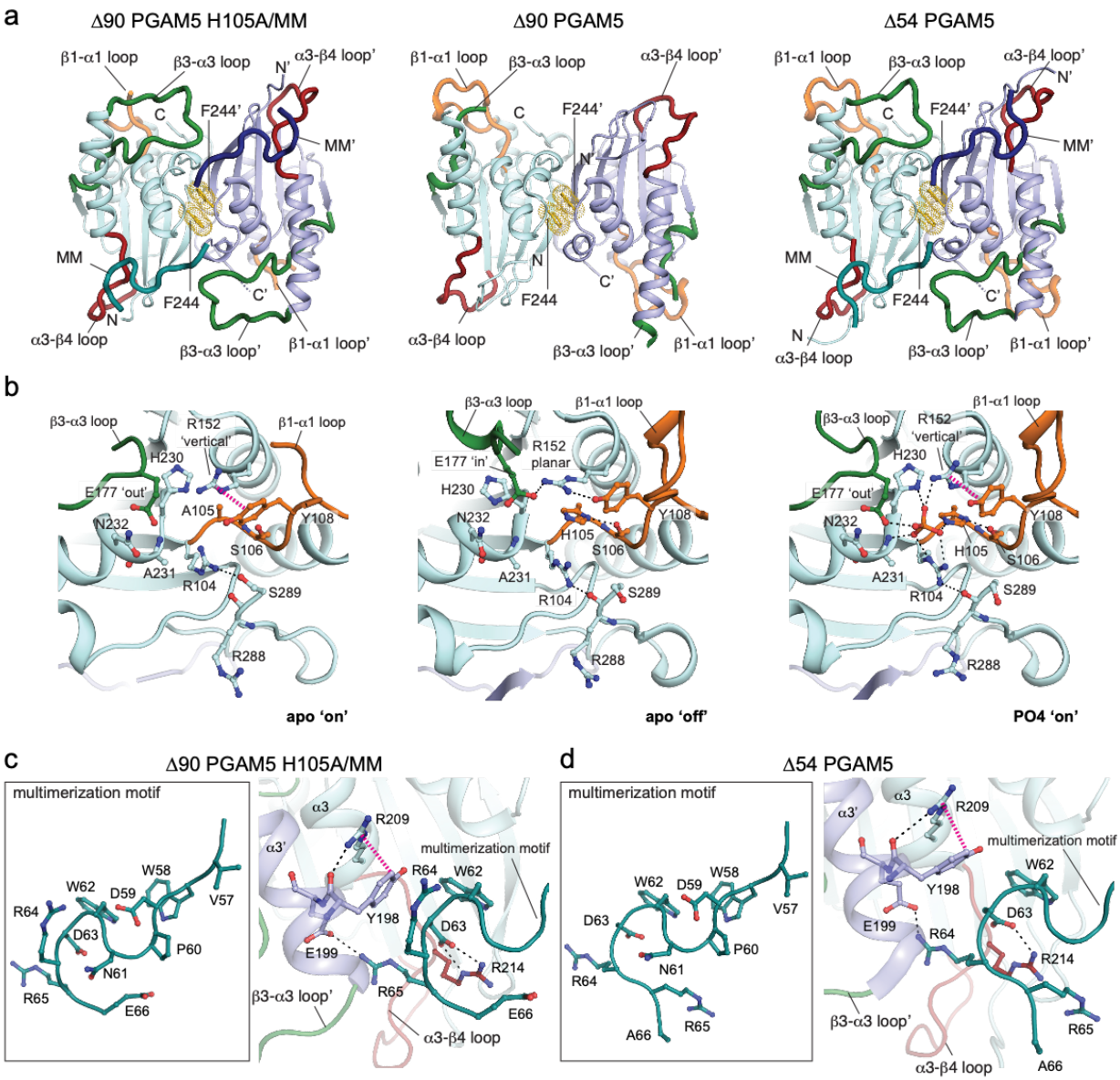

Fig. 2.6: Key features of PGAM5 activation in the crystal structure of Δ90 PGAM5 H015A/MM. **a.** The structures of Δ90 PGAM5 H105A with the multimerization motif (MM) added in *trans* (Δ90 PGAM5 H105A/MM) (left panel) compared to the structures of Δ90 PGAM5 (PDB: 3MXO) (middle panel) and Δ54 PGAM5 with the MM present in *cis* (PDB: 5MUF) (right panel). Monomers 1 and 2 are colored cyan and light blue, respectively, in all structures with their corresponding MM regions colored in teal (monomer 1 MM) and dark blue (monomer 2 MM) where present. The β1- α1 loop is indicated in orange, the β3-α3 loop is indicated in green, the α3-β4 loop is indicated in red. The F244 residues in the central axis forming the dimer interface are indicated in yellow. **b.** Detailed view of the catalytic core in Δ90 PGAM5 H105A/MM (left), Δ90 PGAM5 (middle), and Δ54 PGAM5 (right) highlighting interactions between active site residues and the phosphate ion (PO_4). **c-d.** Comparison of the MM architecture (left panel) and the differences in interactions with the phosphatase domain (right panel) for (c) Δ90 PGAM5 H105A/MM and (d) Δ54 PGAM5.

Altogether, these structures point to a remarkable plasticity of the PGAM5 catalytic center, which indicates that multiple structural elements coordinate for catalysis.

We also observed a notable difference in the conformation of the C-terminal region of the multimerization motif between our Δ90 PGAM5 H105A/MM structure and the previously determined Δ54 PGAM5 structure[34]. Although an identical length of the linker is resolved in both, the improved resolution of the Δ90 PGAM5 H105A/MM structure and overall quality of the electron density map in the linker region revealed a register shift in which the positions of R64 and R65 in the Δ54 PGAM5 structure are occupied by R65 and E66 in the Δ90 PGAM5 H105A/MM structure, respectively (Fig. 2.5c,d; Fig. 2.4e, Fig. 2.7). In Δ90 PGAM5 H105A/MM, R64 is positioned directly in the center of a dimerization interface mediated by the α3 helices (Fig. 2.5c, right panel), expanding the network of interactions in this region. The guanidinium group of R64 in monomer 1 is also involved in a previously unobserved cation π–stacking interaction in *trans* with the phenyl ring of Y198 of the adjacent monomer. Residue E199, previously described as hydrogen bonded to R64 of the adjacent monomer, now interacts with R65. In both structures, R214 hydrogen bonds in *cis* with D63, and R209 with the backbone carbonyl of Y198 in *trans* (Fig. 2.5c,d).

Catalytic activation of PGAM5 requires dodecamer formation

We further examined the role of dodecamer formation in the regulation of PGAM5 activity. In PGAM5 ring structures, each multimerization motif peptide interacts with three phosphatase domain monomers. An interaction with the central phosphatase subunit involves binding of the WDxxWD sequence of the multimerization motif. Two additional minor interactions engage N-

and C-terminal ends of the multimerization motif with two distinct dimer interfaces formed by the neighboring phosphatase domains (Fig. 2.8a).

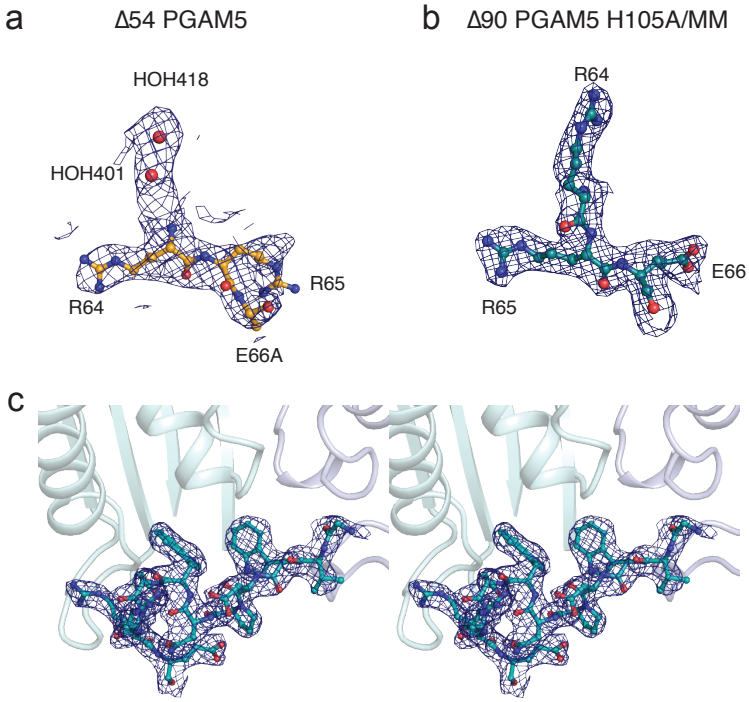

Fig. 2.7: Multimerization motif residue register and corresponding electron density. Differences in the electron density ($2F_o$-F_c maps contoured to 1σ), and subsequent amino acid assignment, of the multimerization motif region (residues 64 – 66) interacting with the phosphatase domain in **a.** Δ54 PGAM5 (PDB: 5MUF) and **b.** Δ90 PGAM5 H105A/MM. **c.** Stereo representation of the multimerization motif peptide (teal) associated with monomer 1 (cyan) in Δ90 PGAM5 H105A/MM, with corresponding $2F_o$-F_c electron density contoured to 1.0σ.

We defined the first minor interaction as the F dimer interface because of the presence of a pair of centrally located F244 residues supporting the dimerization interface. We defined the second interaction as the α3 dimer interface, because it involves a phosphatase domain dimer that engages the α3 helices. We introduced the F244E mutation to disrupt the F dimer interface and Y198E or R65A mutations to disrupt the α3 dimer interface (Fig. 2.8b). We also generated an A4 mutant of PGAM5 in which residues WDxxWD of the multimerization motif are replaced by the AAxxAA sequence, which inactivates PGAM5[33].

All four mutations affected Δ48 PGAM5 oligomerization (Fig. 2.8b,c). The F244E mutation had the most dramatic effect, shifting the entire population of Δ48 PGAM5 to a monomeric state. Likewise, the A4 mutant did not engage in higher-order oligomerization and, instead, preferentially formed dimers. Like the A4 mutant, both the Y198E and R65A mutants were predominantly or completely dimers. Because none of the A4, Y198E, or R65A mutations altered the F dimer interface, we predicted that their dimeric state is likely stabilized by the F244-centered interface (Fig. 2.8a). These findings suggested that, although both the F dimer and α3 dimer interfaces are important for ring formation, only the F244-mediated dimerization occurs in the absence of dodecamer formation.

We determined the catalytic activity of the PGAM5 interface mutants, including the H105A mutant as a negative control, by measuring the rate of PGAM5-mediated dephosphorylation of a phospho-ASK1 substrate peptide (Table 2.2). Like the A4 mutant, the monomerizing F244E mutation also resulted in the loss of phosphatase activity (Fig. 2.8d). The Y198E and R65A mutations, which dissociated Δ48 PGAM5 ring oligomers without disrupting the F dimer, impaired phosphatase activity, decreasing catalytic efficiency ~2 and ~5 fold, respectively (Fig. 2.8d, Table 2.2). The negative effect of every mutation disrupting PGAM5 ring assembly on phosphatase activity indicated that dodecamer formation is necessary to achieve maximal catalytic efficiency. These results also showed that phosphatase activity primarily depends on the interaction between the multimerization motif and phosphatase domains through the F dimer interface and that organization of F dimers into a hexameric ring through the α3 dimer interface further potentiates activity.

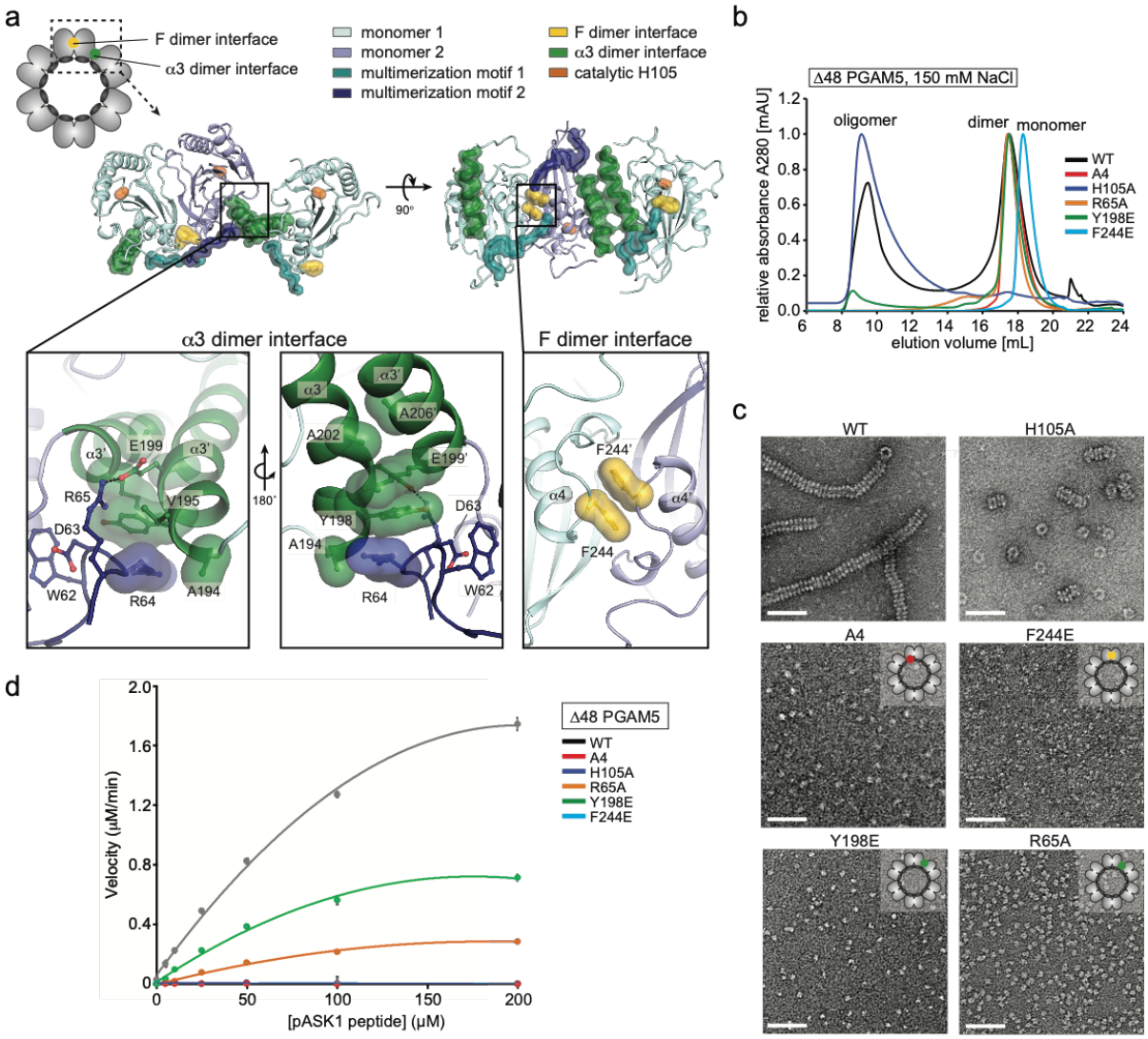

Fig. 2.8: PGAM5 multimerization is required for catalysis. a. Overview of interactions contributing to the stability of the dodecamer assembly in the structure of Δ90 PGAM5 H105A/MM. **b.** SEC elution profiles of wild type (WT) and interface-disrupting mutants (R65A, H105A, Y198E, F244E, and A4) of Δ48 PGAM5 in 150mM NaCl-containing buffer, highlighting the effect of the MM (R65A, A4) and dimer interface (F244E, Y198E) mutants on the oligomer/dimer equilibria observed in wild type Δ48 PGAM5. **c.** EM micrographs of negatively-stained samples of interface mutants of PGAM5 corresponding to the oligomer peaks for WT and H105A, and dimer/monomer peaks for all the other mutants as shown in (b). The insets in top right corners illustrate the position of the respective mutations within the PGAM5 dodecamer cartoon. Scale bars correspond to 50 nm. **d.** Phosphatase activity of the WT and mutant variants of Δ48 PGAM5 measured for 20 nM enzyme and varying concentrations of a phosphorylated ASK1 substrate peptide. Data are represented as mean +/- S.E.M.. The kinetic parameters K_m, k_{cat} and k_{cat}/K_m were determined using GraphPad Prism and are summarized in Table 2.2.

Table 2.2: Phosphatase activity of PGAM5 and its oligomerization-deficient mutants.

Dephosphorylation of the ASK1 phosphopeptide by WT and mutant variants of Δ48 PGAM5 was measured at 20 nM of enzyme concentration and varying concentrations of ASK1 substrate. The kinetic parameters K_m, k_{cat} and k_{cat}/K_m were determined using GraphPad Prism software. Kinetic data for PGAM5 variants without measurable phosphatase activity is denoted ND (not determined). Data are represented as mean +/- S.E.M..

Protein	K_m [μM]	K_{cat} [min^{-1}]	$Kcat/K_m$ [$min^{-1}M^{-1}$]
Δ48 WT	115.2 ± 5.0	137.20 ± 2.98	1.19 (± 0.06) · 10^6
Δ48 H105A	ND	ND	ND
Δ48 R288E	174.70 ± 26.99	143.30 ± 12.73	0.82 (± 0.15) · 10^6
Δ48 F244E	ND	ND	ND
Δ48 A4	ND	ND	ND
Δ48 R65A	119.9 ± 15.7	23.17 ± 1.55	0.19 (± 0.03) · 10^6
Δ48 Y198E	86.17 ± 6.19	51.65 ± 1.68	0.60 (± 0.05) · 10^6

Filament formation does not enhance PGAM5 activity

In solutions of physiological ionic strength, Δ48 PGAM5 existed predominantly as filaments composed of repeating dodecameric rings (Fig. 2.1c). Although such structures are not present in the crystal lattice of Δ54 PGAM5[34], the unit cell of our Δ90 PGAM5 H105A/MM structure reveals rings stacked to form tubular filaments (Fig. 2.9a). Within the filament, each successive ring is rotated ~15˚ around the 6-fold symmetry axis relative to the neighboring ring. This architecture resembles the filament organization of Δ48 PGAM5 examined by negative-stain EM (Fig. 2.9b). In the crystal structure, the lattice interactions that mediate ring stacking lack an extensive buried surface area and rely on sparse and non-symmetrically distributed hydrogen bond interactions between residues within loops at the perimeter of the rings (Fig. 2.9c and Fig. 2.10a). This could explain the apparent lack of structural rigidity in the EM images (Fig. 2.5b). Mutation of the hydrogen-bonding residues did not have a measurable effect on formation of the Δ48 PGAM5 filaments in solution (Fig. 2.10b), suggesting that stabilization of filament formation likely occurs through forces independent of loop interactions observed in the crystal structure.

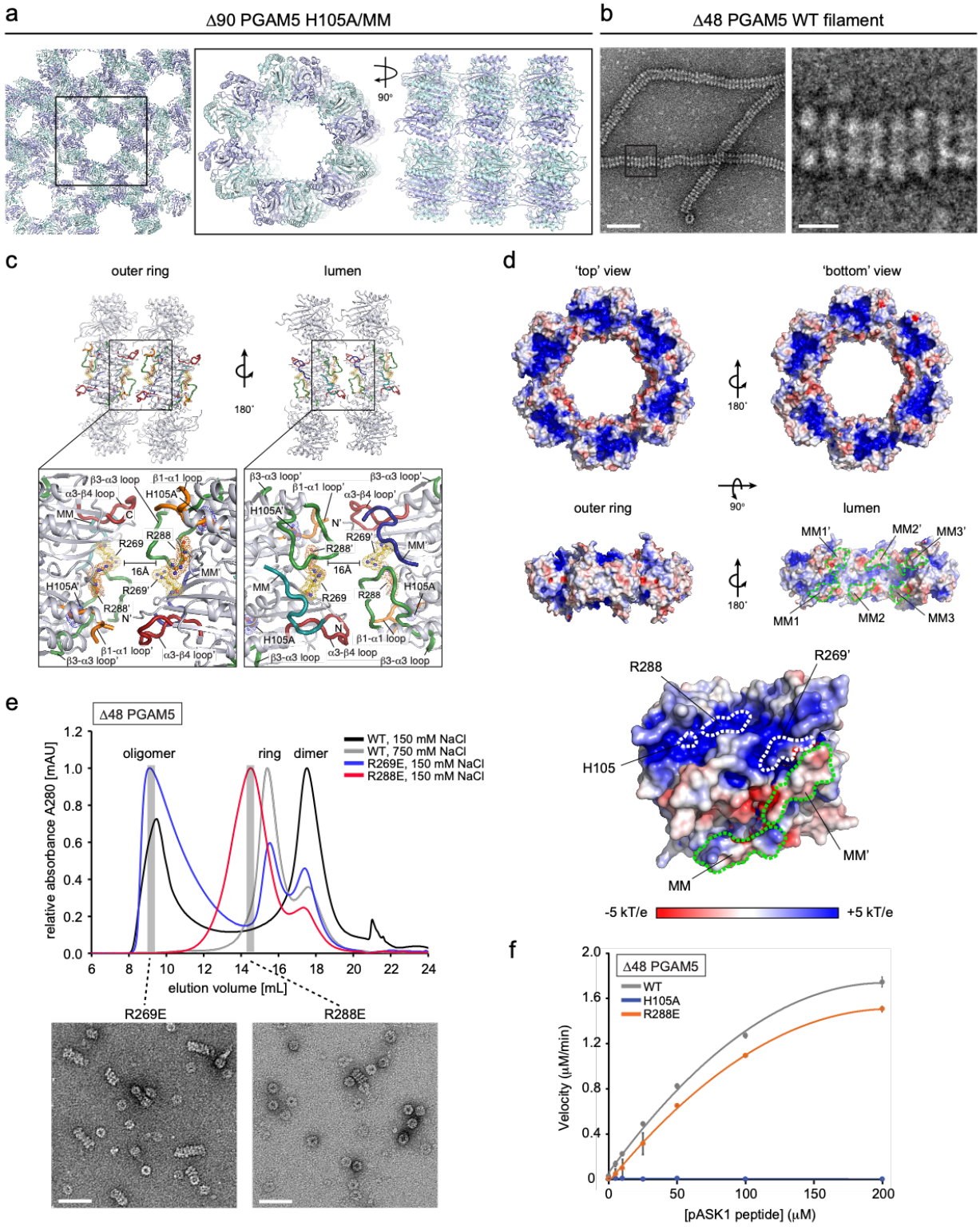
a
Δ90 PGAM5 H105A/MM
90°
b
Δ48 PGAM5 WT filament
c
outer ring
lumen
180°
β3-α3 loop
β1-α1 loop
α3-β4 loop
H105A
MM
C
R288
R269
16Å
MM'
H105A'
R269'
R288'
N'
β1-α1 loop'
α3-β4 loop'
β3-α3 loop'
N
d
'top' view
'bottom' view
180°
90°
outer ring
lumen
MM1'
MM2'
MM3'
MM1
MM2
MM3
R288
R269'
H105
MM'
MM
-5 kT/e
+5 kT/e
e
Δ48 PGAM5
oligomer
ring
dimer
WT, 150 mM NaCl
WT, 750 mM NaCl
R269E, 150 mM NaCl
R288E, 150 mM NaCl
relative absorbance A280 [mAU]
elution volume [mL]
R269E
R288E
f
Δ48 PGAM5
WT
H105A
R288E
Velocity (μM/min)
[pASK1 peptide] (μM)

Fig. 2.9: Role of PGAM5 filaments in catalysis. a-b. Overview of the (a) crystal packing in the Δ90 PGAM5 H105A/MM structure (left panel) highlighting a network of stacked rings (right panel), which resembles the organization of (b) filaments observed for Δ48 PGAM5 in solution by negative-stain EM. **c.** Overview of the ring stacking interface highlighting the positions of residues at the surface of the substrate-binding cleft relative to structural elements contributing to peripheral interactions between two adjacent dodecamers within the crystal lattice of the Δ90 PGAM5 H105A/MM structure. **d.** Electrostatic surface potential calculated for the Δ90 PGAM5 H105A/MM dodecamer using APBS[71]. The positions of the MM outlined in green are shown relative to the positions of basic residues R269E and R288E within the positively charged substrate-binding cleft as well as the catalytic residue, H105, in the active site. Coloring corresponds to the electronegativity of the surface potential as defined in the scale bar, with more negatively charged surfaces colored red and positively charged surfaces colored blue. **e.** Upper panel: size exclusion chromatograms of the WT Δ48 PGAM5 purified in buffer containing low (150 mM NaCl) or high (750 mM NaCl) salt concentrations compared to the results obtained for the R269E and R288E variants. Lower panel: EM micrographs of the negatively-stained samples of mutant Δ48 PGAM5 taken from the corresponding primary peak of the purification. **f.** Phosphatase activity of the wild type (WT), catalytically inactive H105A, and the stacking-impaired R288E variants of Δ48 PGAM5 measured for 20 nM enzyme and varying concentrations of a phosphorylated ASK1 substrate peptide. Data are represented as mean +/- S.E.M.. The kinetic parameters K_m, k_{cat} and k_{cat}/K_m were determined using GraphPad Prism and are summarized in Table 2.2. Scale bars in (b) and (e) correspond to 50 nm, except for the inset in (b) which corresponds to 10 nm.

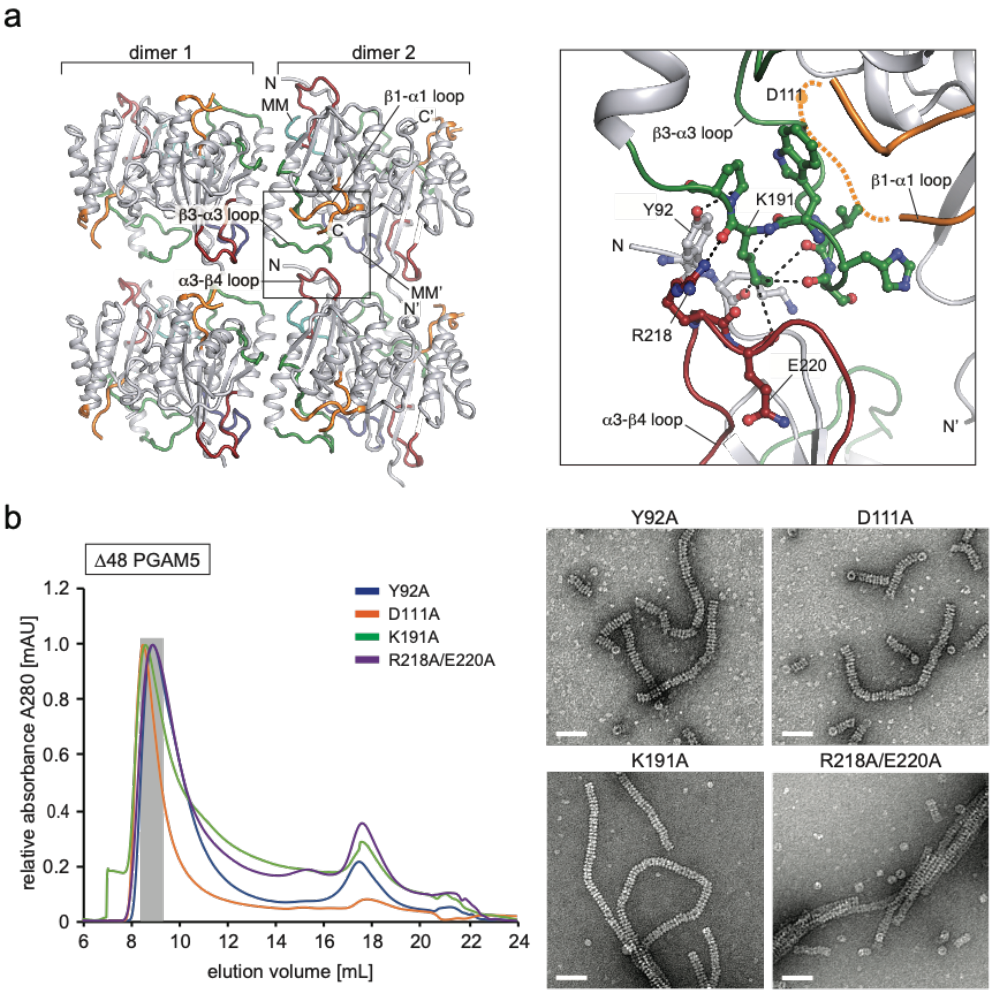

Fig. 2.10: Effect of mutations in the residues making direct contact at the crystallographic dodecamer stacking interface. a. Overview of the stacking interface between adjacent rings in the crystalline lattice of the Δ90 PGAM5 H105A/MM structure (left panel). Residues forming hydrogen bonding interactions at contact sites between rings are highlighted in the right panel. **b.** Elution profiles for Δ48 PGAM5 constructs carrying the indicated mutations of residues identified in **(a)** and purified by size exclusion chromatography (SEC) using a Superose 6 column (GE Healthcare) in SEC buffer containing 20 mM Tris-Cl pH 8.0, 500 µM TCEP, and 150 mM NaCl. EM micrographs of negatively-stained samples of the PGAM5 mutants taken directly from the indicated oligomer peaks observed during SEC are shown to the right.

The 2-fold rotational symmetry relating individual monomers within each phosphatase dimer results in identical electrostatic surface potentials on both sides of the dodecameric assembly (Fig. 2.9d). Basic residues comprise a large positively-charged patch centered on the catalytic clefts of each dimer surrounded by somewhat negatively-charged protruding loops. The structural and electrostatic symmetry suggests that filament formation lacks directionality and can occur from either face of the ring. These characteristics, together with the disruptive effect of high ionic strength on PGAM5 filaments (Fig. 2.1d), implicate complementary electrostatic forces in stabilizing the formation of PGAM5 filaments *in vitro*. To test this, we designed two charge-reversing mutations within the basic cleft, R269E and R288E, and examined their influence on PGAM5 filamentation. In buffers with physiological salt concentrations, each mutation reduced PGAM5 filament length and formation, with the R288E mutation having the greater effect (Fig. 2.9e). With the R288E mutant, we then investigated the role filaments play in regulating phosphatase activity. The phosphatase activities were similar for both wild type and R288E Δ48 PGAM5, suggesting that filament formation does not contribute substantially to the catalytic efficiency of PGAM5 phosphatase activity (Fig. 2.9f, Table 2.2).

PGAM5 forms large oligomers in cells upon cleavage from IMM

We investigated whether PGAM5 also organizes into filaments in living cells. Our biochemical and structural analysis of the filaments focused on PGAM5 without its membrane-anchoring helix. This construct approximates the state of PGAM5 generated by PARL or OMA1 cleavage in response to the loss of mitochondrial membrane potential upon treatment with CCCP, a small molecule inhibitor of oxidative phosphorylation. The resulting cleaved PGAM5 is mainly detected in mitochondria, with only a fraction detectable in the cytosol[6,8,9,11]. We explored the

subcellular localization and oligomerization of endogenous PGAM5, using CCCP to induce cleavage of PGAM5 in HEK293T cells and subcellular fractionation to distinguish between the cytoplasmic and mitochondrial pools of PGAM5. In CCCP-treated cells, cleaved PGAM5 predominantly partitioned to mitochondria (Fig. 2.11a). To assess the oligomeric state of mitochondrial PGAM5 before and after cleavage, we used blue native electrophoresis (BN-PAGE). We confirmed that BN-PAGE could differentiate different sizes of PGAM5 oligomers by comparing the migration of recombinant wild type Δ48 PGAM5 and the oligomerization-deficient mutant F244E (Fig. 2.11b). By comparing the migration of endogenous PGAM5 in the cytoplasmic (cyto) and mitochondrial (mito) fractions of untreated or CCCP-treated cells, we observed markedly higher molecular weight species for the cleaved pool of mitochondrial PGAM5 compared to the uncleaved population, approximating the behavior of the recombinant wild type Δ48 PGAM5 filaments (Fig. 2.11b). We observed a similar pattern in the cytosolic fraction after CCCP treatment, although the cytosolic pool represented only a small fraction of the total PGAM5 detected.

To visualize PGAM5 filaments in cells, we focused on cytosolic cleaved PGAM5 due to resolution limits preventing the distinction between membrane-tethered and cleaved PGAM5 molecules in the mitochondrial intermembrane compartment. To increase the pool of the cleaved cytosolic PGAM5, we expressed and imaged myc-tagged Δ23 PGAM5 (residues 24-289), mimicking the cleaved version, in COS7 cells using confocal microscopy. In a small subset of transfected cells, we observed myc-positive wire-like cytosolic structures (Fig. 2.11c). Using two higher-resolution imaging techniques, stimulated emission depletion microscopy (STED) and structured illumination microscopy (SIM), we visualized PGAM5 filaments throughout the cytoplasm in the subset of cells with this PGAM5 phenotype (Fig. 2.11c).

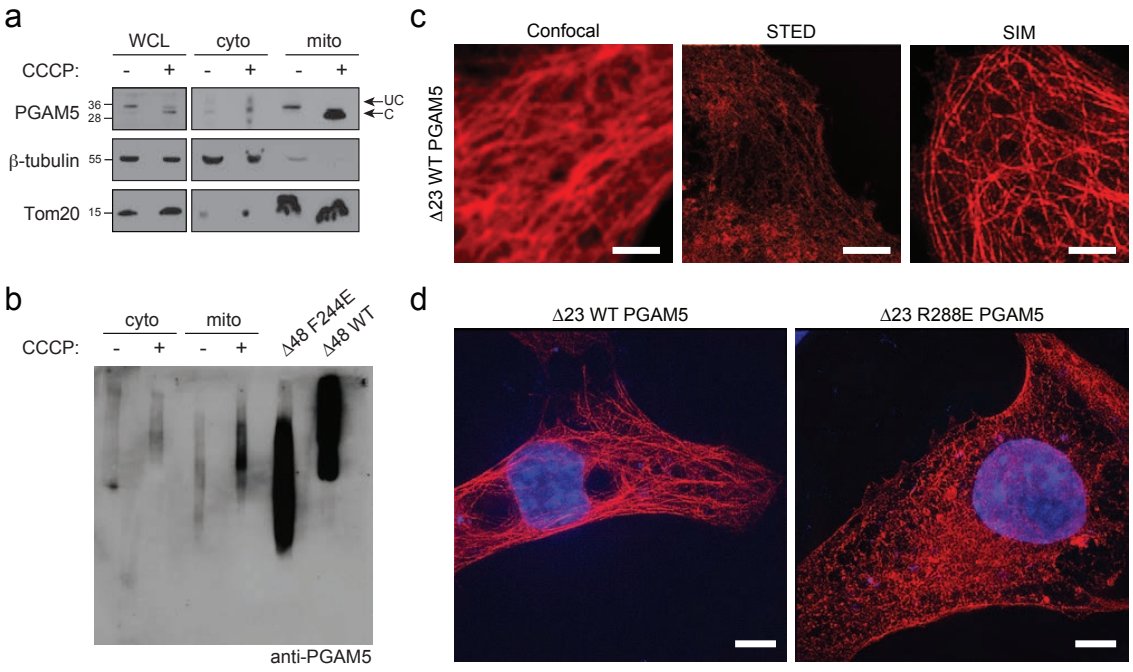

Fig. 2.11: Cleaved PGAM5 forms oligomers in cells. a. SDS-PAGE analysis of endogenous PGAM5 in HEK293T whole cell lysate (WCL), mitochondrial (mito), and cytoplasmic (cyto) fractions 4 hours post CCCP treatment. Uncleaved (UC) and cleaved (C) PGAM5 bands are marked by arrows. **b.** BN-PAGE analysis of endogenous PGAM5 4 hours post CCCP treatment in mitochondrial (mito) and cytoplasmic (cyto) fractions. Fractionation samples were normalized based on the total protein concentrations determined for the WCL samples. As a reference for migration behavior of PGAM5 oligomers, recombinant Δ48 WT (Δ48 WT) and the oligomerization-deficient mutant Δ48 F244E mutant (Δ48 F244E) PGAM5 were run alongside cellular fractionation samples on a 4-16% native-PAGE acrylamide gel (Invitrogen). Following electrophoresis, gels were immunoblotted with anti-PGAM5 antibody. **c.** Comparison of myc-tagged Δ23 PGAM5 (myc-PGAM5) filaments in transiently transfected COS7 cells stained with anti-myc antibody using three different imaging methods: confocal microscopy (left panel), stimulated emission depletion (STED) microscopy (middle panel), and structured illumination microscopy (SIM) (right panel). All scale bars correspond to 5 μm. **d**. SIM images of myc-tagged Δ23 PGAM5 filaments in COS7 cells transiently expressing wild type (WT) or the R288E PGAM5 (red). Nuclei were stained using DAPI (blue). Both scale bars in (d) correspond to 10 μm.

As a control, we evaluated the PGAM5 phenotype of the filament disrupting mutant, R288E (Fig. 2.9e). We did not find any cytosolic filaments in cells expressing the R288E mutant of Δ23 PGAM5 (Fig. 2.11d). All mutations that disrupted dodecamer assembly and consequently formation of PGAM5 filaments *in vitro* (Fig. 2.8b,c) also eliminated the detection of filaments in

cells (Fig. 2.12). Thus, the cellular structures we observed have properties like the PGAM5 filaments observed *in vitro*.

We noted that the architecture of cleaved PGAM5 filaments formed in cells resemble cytoskeletal structures. To test for a spatial relationship between PGAM5 filaments and cytoskeleton, we assessed PGAM5 filament colocalization with actin fibers or microtubules. Although we did not detect overlap between PGAM5 filaments and actin fibers (Fig. 2.13a), PGAM5 filaments colocalized with microtubules (Fig. 2.13b). Upon nocodazole treatment to disrupt microtubule polymerization, detection of PGAM5 filaments was lost (Fig. 2.14), suggesting a potentially intriguing dependence of PGAM5 filament assembly in cells on PGAM5 association with intact microtubules.

PGAM5 dodecamers promote mitochondrial clustering

Under conditions of intact mitochondrial membrane potential, PGAM5 is expected to remain in the uncleaved, membrane-tethered form. To examine the importance of PGAM5 oligomerization in this context, we leveraged the observation that overexpression of full-length PGAM5 induced clustering of mitochondria in the perinuclear region[5]. PGAM5 knockdown has an opposite effect on mitochondria, resulting in increased tubular morphology[26] and decreased stress-induced mitochondrial clustering[35]. Such effects on mitochondrial behavior stemming from changes in PGAM5 abundance may reflect the role of PGAM5 in maintaining mitochondrial homeostasis[13,26,33]. Using confocal imaging of COS7 cells, we evaluated the colocalization of full-length PGAM5 or PGAM5 mutants and a marker of mitochondrial outer membranes, Tom20 and assessed the effect of full-length PGAM5 expression on mitochondrial morphology (Fig. 2.15a).

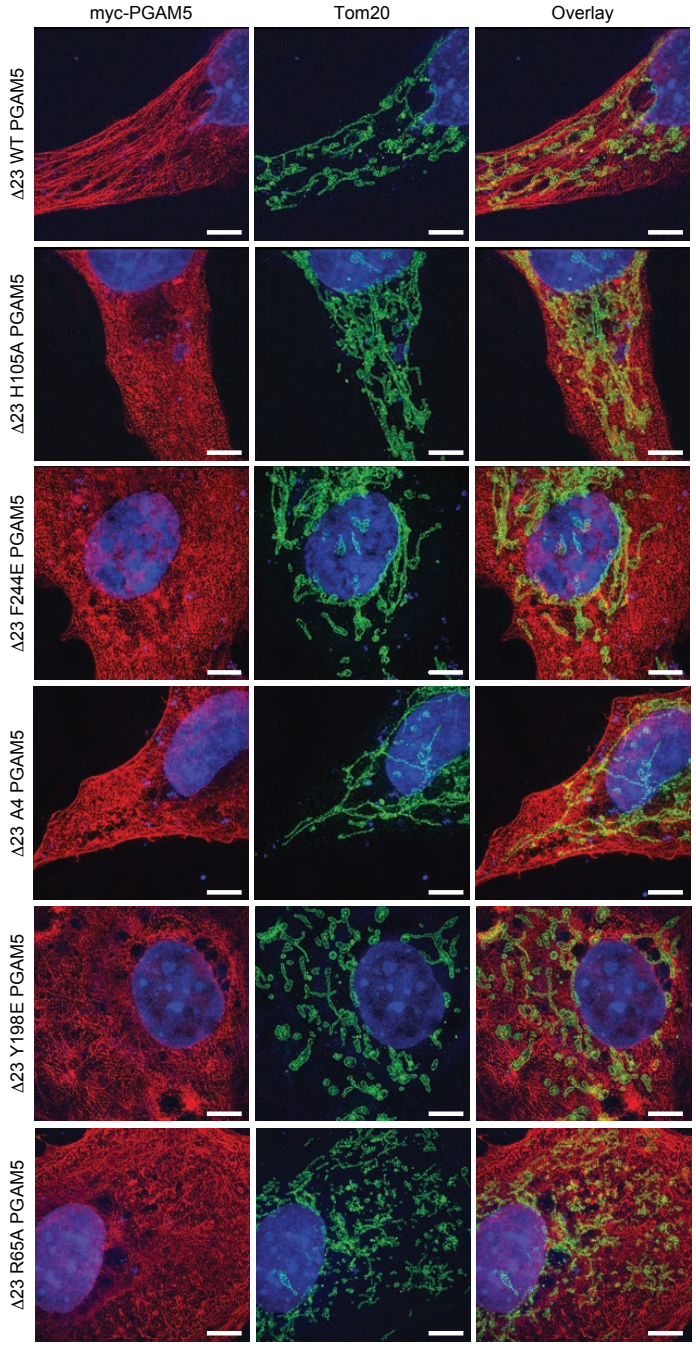

Fig. 2.12: Effect of dimerization interface mutations on PGAM5 filamentation. Representative structured illumination microscopy (SIM) images of COS7 cells transiently transfected with the myc-tagged Δ23 PGAM5 wild type (WT) and mutant variants. COS7 cells were immunostained for Tom20 with anti-Tom20 antibody (green), for PGAM5 with anti-myc antibody (red) and for nuclei with DAPI (blue). All scale bars correspond to 10 µm.

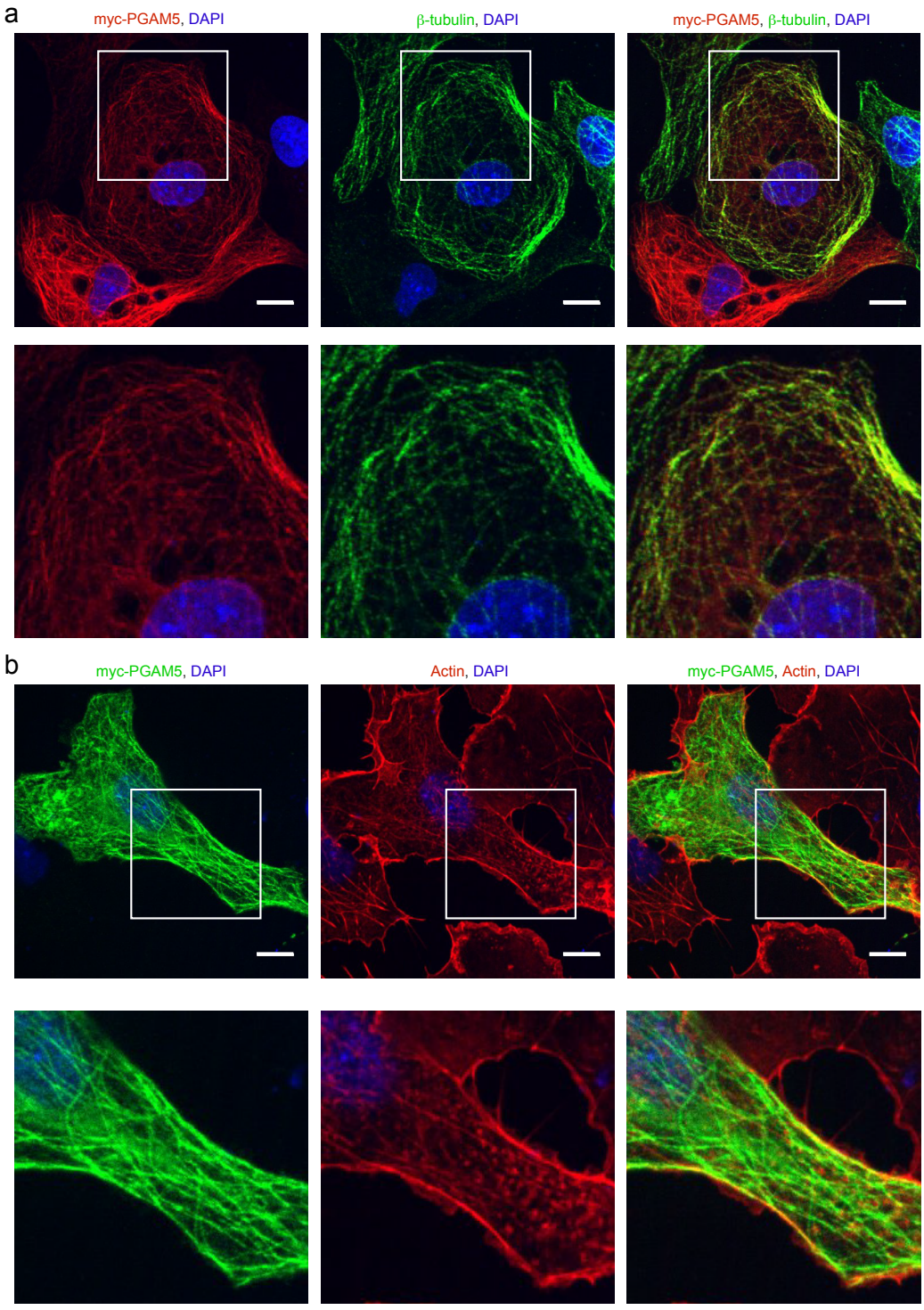

Fig. 2.13: Colocalization of PGAM5 filaments with cytoskeletal structures. a-b Representative confocal images of COS7 cells transiently transfected with the myc-tagged Δ23 PGAM5 construct. **a.** COS7 cells were immunostained for microtubules with anti-β tubulin antibody (green), for PGAM5 with anti-myc antibody (red), and with DAPI (blue). **b.** COS7 cells were immunostained for actin with Alexa Fluor-647-phalloidin (red), for PGAM5 with anti-myc antibody (green) and for nuclei with DAPI (blue). All scale bars correspond to 10 µm.

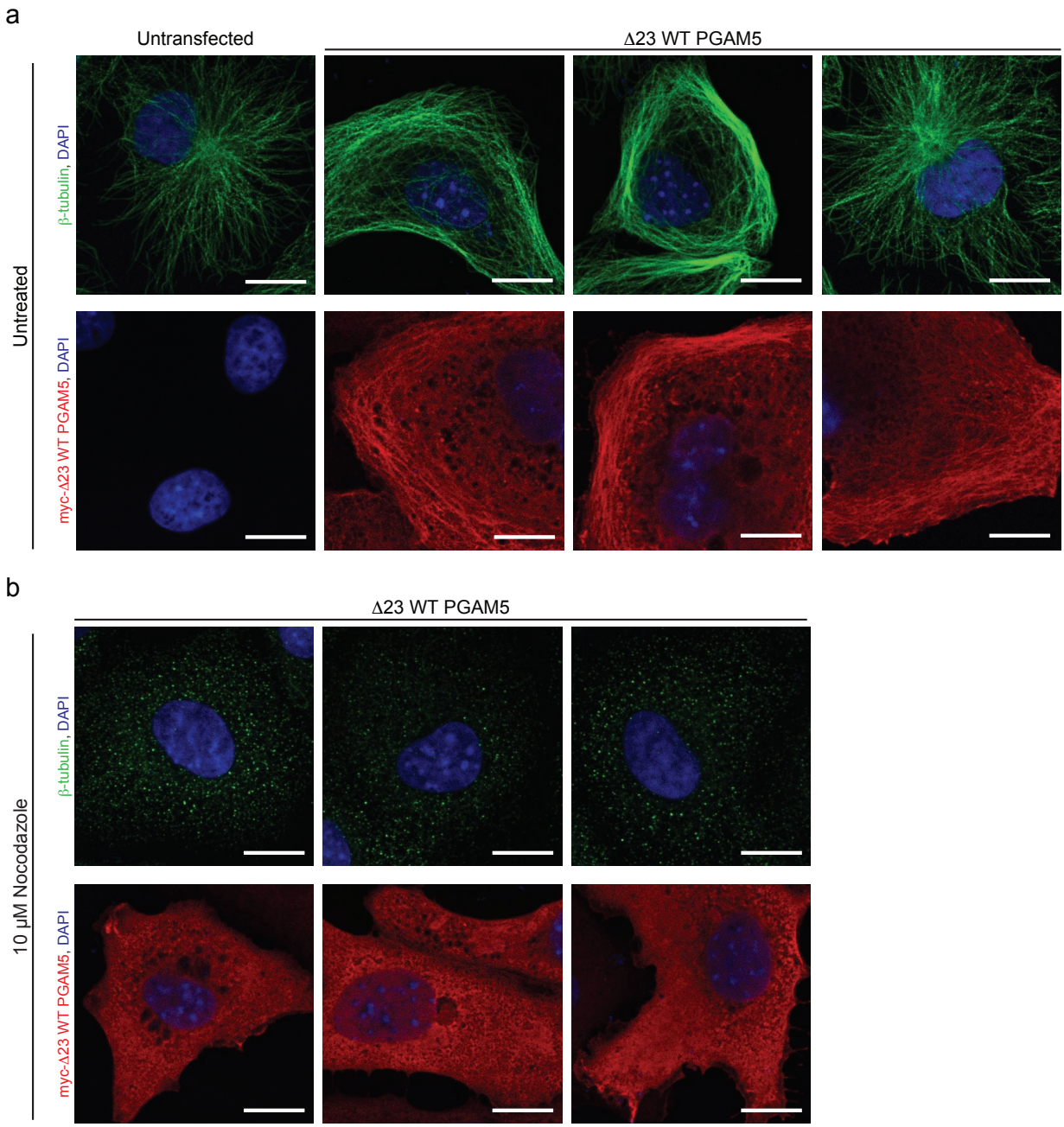

Fig. 2.14: Effect of nocodazole treatment on PGAM5 filaments. **a-b.** Representative confocal images of COS7 cells transiently transfected with myc-tagged Δ23 PGAM5. **a.** Untreated COS7 cells, either untransfected or transfected with myc-tagged Δ23 PGAM5 wild type (WT). Upper panel: staining for β-tubulin with anti-β-tubulin antibody (green) and for nuclei with DAPI (blue). Lower panel: staining for PGAM5 with anti-myc antibody (red) and for nuclei with DAPI (blue). **b.** COS7 cells transfected with myc-tagged Δ23 PGAM5 wild type (WT) treated with 10 μM nocodazole for 45 minutes. Upper panel: staining for β-tubulin with anti-β-tubulin antibody (green) and for nuclei with DAPI (blue). Lower panel shows a different set of cells stained for PGAM5 with anti-myc antibody (red) and for nuclei with DAPI (blue). All scale bars correspond to 15 μm.

Consistent with previous reports[33], expression of the two catalytically inactive PGAM5 mutants, H105A and A4, had opposing effects on mitochondrial clustering. The membrane-tethered H105A mutant induced mitochondrial clustering, similar to the effect of overexpressing wild type PGAM5; the A4 mutant resulted in fragmentation of the mitochondria (Fig. 2.15a,b).

The differences in the architecture of recombinant PGAM5 complexes formed by the H105A and A4 mutants could explain their effects on mitochondria. Although both mutations inactivate PGAM5, the H105A mutant forms higher-order oligomers and the A4 mutant prevents multimerization (Fig. 2.8b,c). Thus, we hypothesized that the assembly of the PGAM5 dodecamer, and perhaps also filamentation, drives changes in mitochondrial morphology. To test this hypothesis, we expressed the F244E mutant, which disrupts the F dimer interface and prevents multimerization, and observed that it failed to induce clustering instead causing mitochondrial fragmentation similar to the A4 mutants (Fig. 2.15a,b). Expressing of both α3 dimer interface mutants (Y198E and R65A), which disrupt ring and filament formation but preserve some phosphatase activity, also failed to induce mitochondrial clustering and resulted in a more tubular phenotype than the A4 or F244E mutants. These results suggested that mitochondrial-clustering phenotype depends on intact dodecamer interfaces of PGAM5, independent from its activity.

To evaluate if assembly of PGAM5 dodecamers into filaments affects mitochondrial clustering, we evaluated the R288E mutation, which disrupted formation of PGAM5 filaments *in vitro* without affecting the structure of the PGAM5 dodecamer (Fig. 2.9e). Expression of the R288E mutant induced mitochondrial clustering, suggesting that filament formation is either nonessential

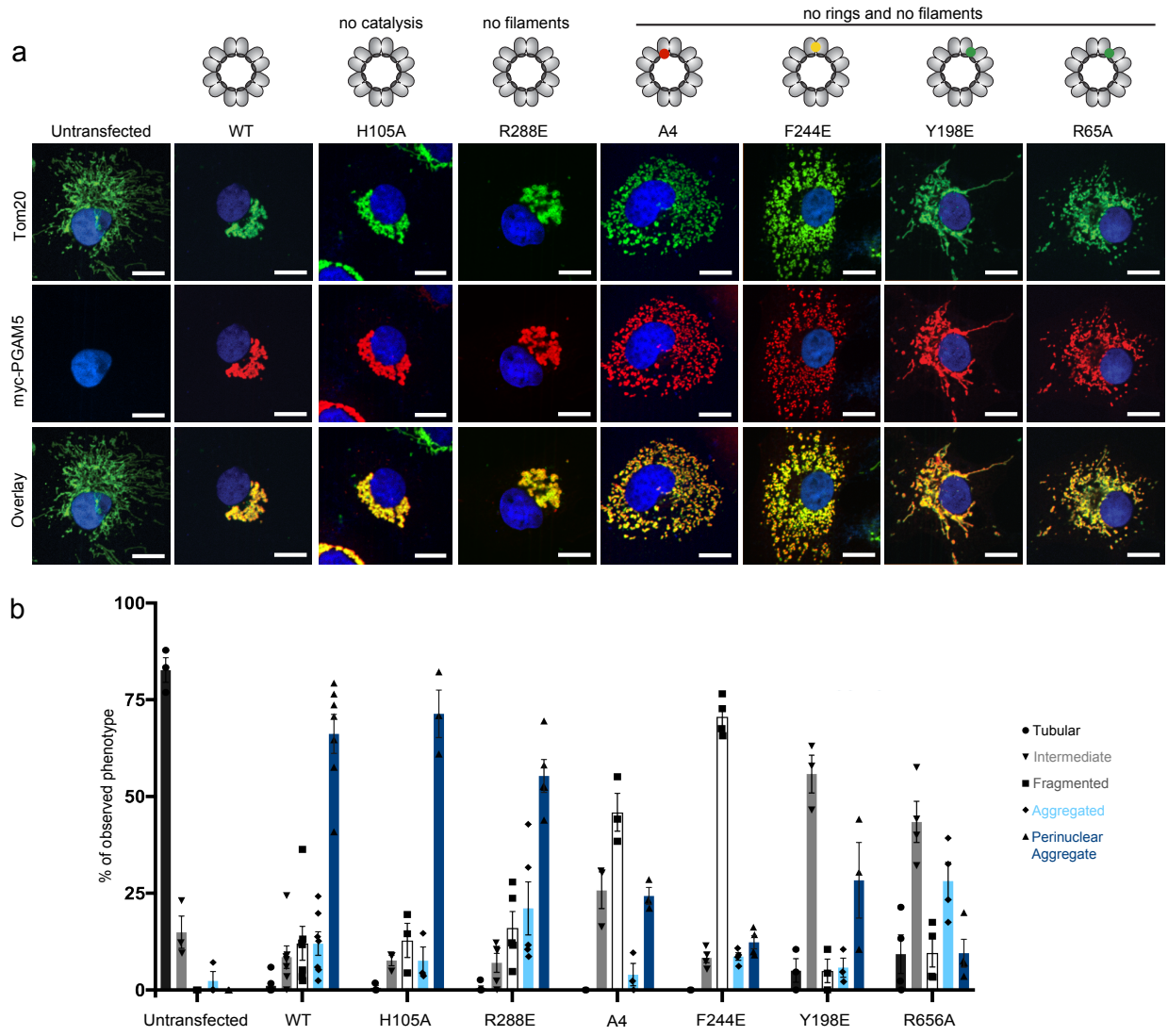

Fig. 2.15: Multimerization of full-length PGAM5 promotes clustered mitochondrial morphology. **a.** Representative confocal images of COS7 cells transiently transfected with the wild type (WT) or mutant full-length myc-tagged PGAM5 constructs and immunostained for the OMM marker Tom20 with anti-Tom20 antibody (green), PGAM5 with anti-myc antibody (red), and nucleic-stain DAPI (blue). All scale bars correspond to 15 µm. **b.** Quantification of mitochondrial phenotypes observed by confocal microscopy in COS7 cells transiently expressing PGAM5 variants as described in (a), based on at least 3 independent experiments per construct. Data are represented as mean +/- S.E.M., determined using GraphPad Prism. Untransfected cells: n= 122 cells over 3 experimental replicates. Cells expressing PGAM5 WT: n=296 cells over 7 experimental replicates. Cells expressing PGAM5 H105A: n= 141 cells over 3 experimental replicates. Cells expressing PGAM5 R288E: n= 212 cells over 5 experimental replicates. Cells expressing PGAM5 A4: n= 144 cells over 3 experimental replicates. Cells expressing PGAM5 F244E: n= 186 cells over 4 experimental replicates. Cells expressing PGAM5 Y198E: n= 108 cells over 3 experimental replicates. Cells expressing PGAM5 R65A: n=141 cells over 4 experimental replicates.

for mitochondrial clustering or is precluded when PGAM5 is embedded within mitochondrial membranes (Fig. 2.15a,b).

Mitochondrial clustering by PGAM5 is independent of DRP1

DRP1, a cytosolic dynamin-family GTPase that binds to its receptors on the OMM to promote mitochondrial fission[36], is a substrate of PGAM5[24,33]. We investigated if the clustering effect of PGAM5 overexpression on mitochondrial morphology depends on DRP1, by assessing the mitochondrial morphology in *Drp1*$^{-/-}$ mouse embryonic fibroblasts (MEFs) upon PGAM5 overexpression. The smaller size of MEF cells relative to COS7 cells made it difficult to categorize the full spectrum of phenotypes noted for COS7 cells (Fig. 2.15a,b), thus we limited the phenotypic analysis of MEFs to three categories: (i) tubular/elongated, (ii) fragmented, and (iii) aggregated (Fig. 2.17). In untransfected *Drp1*$^{-/-}$ cells, mitochondrial tubules were more connected and elongated[37-39] than in wild type MEFs (Fig. 2.16a); however, we were still able to identify all three mitochondrial phenotypes (Fig. 2.17). The distribution of phenotypes was comparable to that in wild type MEFs, despite differences in the overall appearance of the mitochondrial tubules (Fig. 2.16b).

Overexpression of wild-type PGAM5 in wild-type or *Drp1*$^{-/-}$ MEFs resulted in mitochondrial clustering similar to that observed in COS7 cells (Fig. 2.16b,c). Expression of F244E PGAM5 in either wild type or DRP1-knockout cells resulted in a shift to the fragmented phenotype of mitochondria (Fig. 2.16b,c). Thus, the effects of PGAM5 overexpression on mitochondrial phenotypes are independent of DRP1.

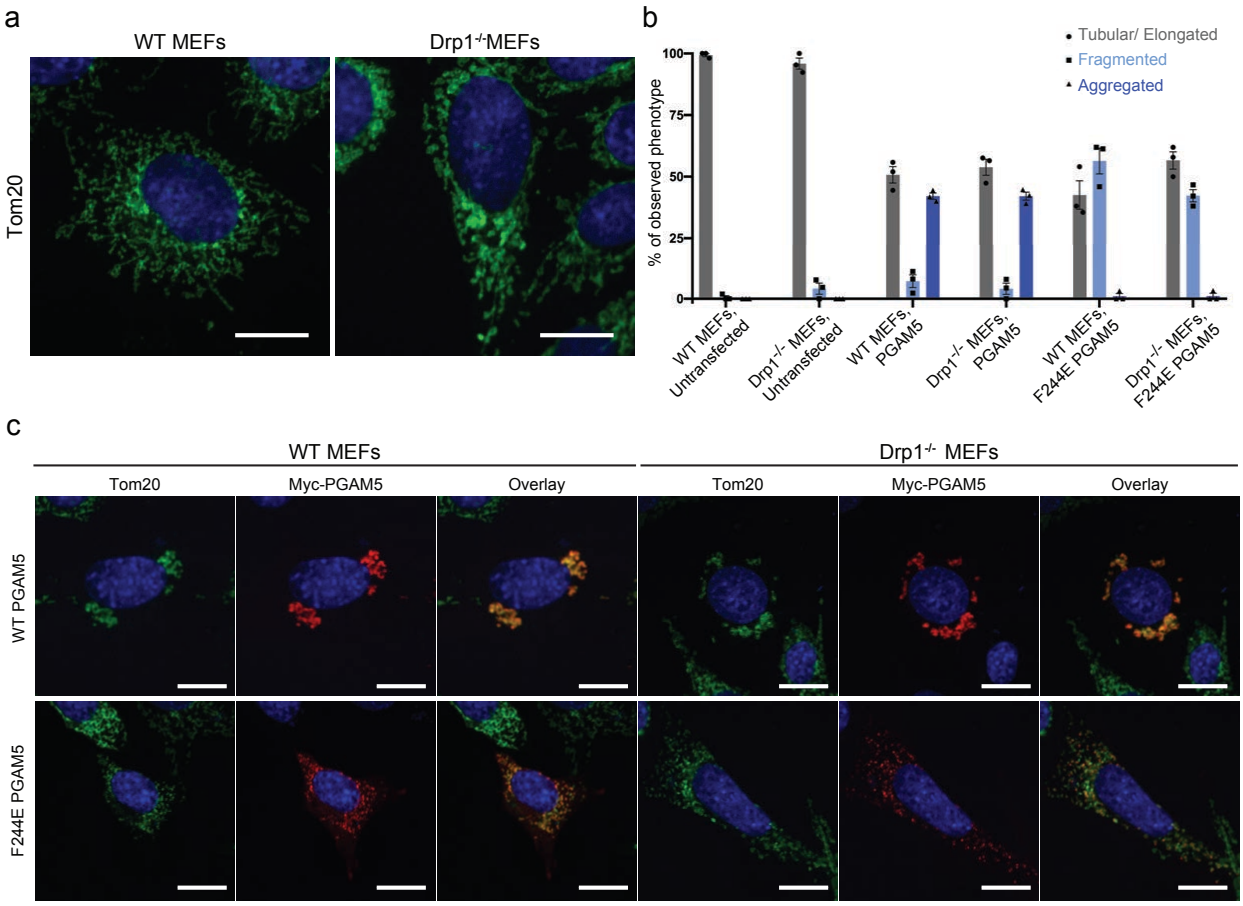

Fig. 2.16: DRP1 is dispensable for the clustered mitochondrial morphology induced by PGAM5. a Representative confocal images of wild type or Drp1$^{-/-}$ MEFs immunostained for the OMM marker Tom20 with anti-Tom20 antibody (green) and with DAPI (blue). Scale bars correspond to 15 µm. **b** Quantification of mitochondrial phenotypes observed by confocal microscopy in wild type or Drp1$^{-/-}$ MEFs either untransfected or transiently transfected with the indicated PGAM5 constructs, based on at least 3 independent experiments per construct. Data are represented as mean +/- S.E.M, determined using GraphPad Prism. Untransfected wild type (WT) MEFs: n= 123 cells over 3 experimental replicates. WT MEFs expressing full-length WT PGAM5: n= 129 cells over 3 experimental replicates. WT MEFs expressing full-length F244E PGAM5: n= 89 cells over 3 experimental replicates. Untransfected Drp1$^{-/-}$ MEFs: n= 154 cells over 3 experimental replicates. Drp1$^{-/-}$ MEFs expressing full-length WT PGAM5: n= 1179 cells over 3 experimental replicates. Drp1$^{-/-}$ MEFs expressing F244E PGAM5: n= 89 cells over 3 experimental replicates. **c**, Representative confocal images of WT or Drp1$^{-/-}$ MEFs transiently transfected with the WT or dimer interface mutant (F244E) full-length myc-tagged PGAM5 and immunostained for the OMM marker Tom20 with anti-Tom20 antibody (green), for PGAM5 with anti-myc antibody (red) and for nuclei with DAPI (blue). All scale bars correspond to 15 µm.

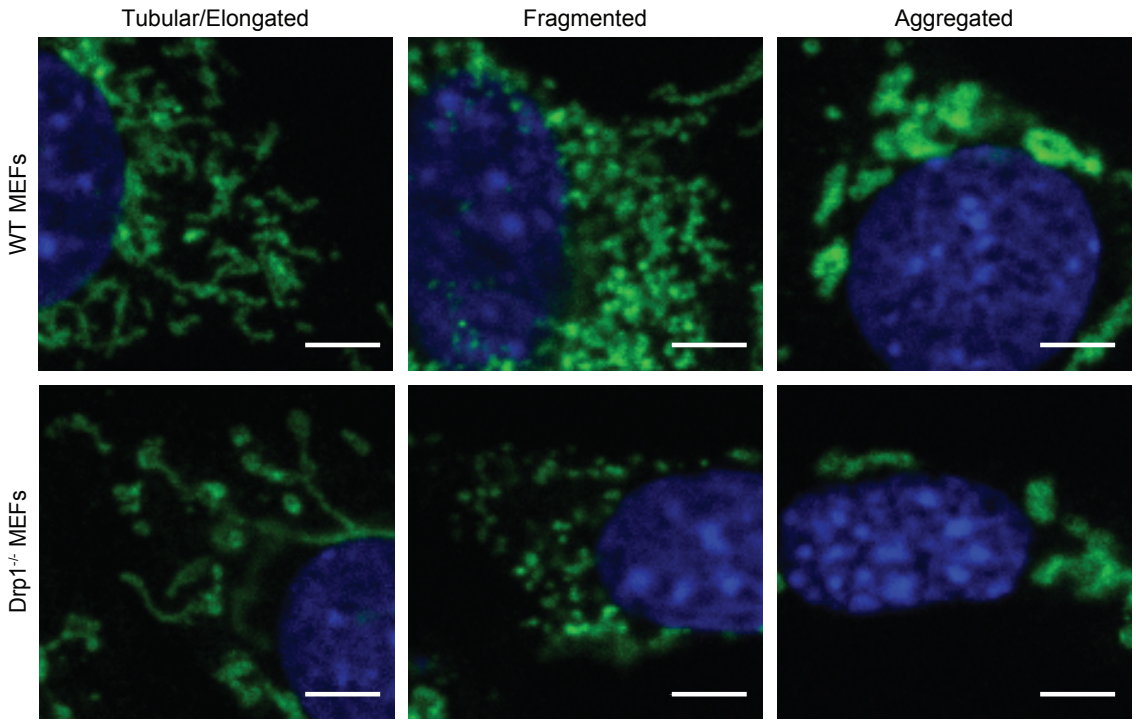

Fig. 2.17: Phenotypic categories used for scoring the effect of PGAM5 overexpression on mitochondrial morphology in MEF cells. Representative confocal images of mitochondria in: untransfected wild type and Drp1$^{-/-}$ MEFs (left panels), wild type and Drp1$^{-/-}$ MEFs transiently transfected with full-length wild type PGAM5 (center panels), or wild type and Drp1$^{-/-}$ MEFs transiently transfected with full-length F244E PGAM5 (right panels). Cells were immunostained for Tom20 with anti-Tom20 antibody (green) and for nuclei with DAPI (blue). All scale bars correspond to 15 μm.

PGAM5 localizes at contact sites of clustered mitochondria

To characterize the spatial distribution of wild-type and F244E PGAM5 at the mitochondria, we used STED to visualize the OMM with Tom20 or the IMM with Tim23. In untransfected COS7 cells, mitochondria adopted a phenotype in which tubular Tom20-positive or Tim23-positive structures extended radially from the perinuclear regions (Fig. 2.18a). In cells transiently transfected with wild-type PGAM5, mitochondrial tubules were replaced by circular mitochondria clustered in the perinuclear region (Fig. 2.18b). Frequently, single clusters were found stacked next to each, appearing as though these membranes were in direct contact (Fig. 2.18c). PGAM5 was localized exclusively inside of these distorted mitochondrial structures and

detected as puncta that mostly colocalized with Tim23 and not with Tom20 (Fig. 2.18b,c). We also observed that PGAM5 colocalization with Tom20 only occurred at the sites of contact between individual mitochondrial clusters (Fig. 2.18b,c).

As with confocal analysis (Fig. 2.15a), STED imaging showed that F244E PGAM5 expression resulted in a fragmented mitochondrial morphology and more diffuse distribution of mitochondrial vesicles in the cell (Fig. 2.18b). In contrast to wild type PGAM5, the F244E-positive mitochondria did not engage in any apparent inter-mitochondrial contacts and PGAM5 in these cells was not colocalized with Tom20. Rather, the F244E mutant was primarily found in Tim23-positive structures (Fig. 2.18b,c). These data point to a functional importance of PGAM5 multimerization in bridging adjacent mitochondrial membranes to promote interactions that might underlie the clustered phenotype. Our data are also consistent with a localization for PGAM5 at the inner mitochondrial membrane and/or possibly also within the intermembrane space, as evidenced by partitioning of the PGAM5 signal at the inner periphery of the OMM and colocalization with Tim23.

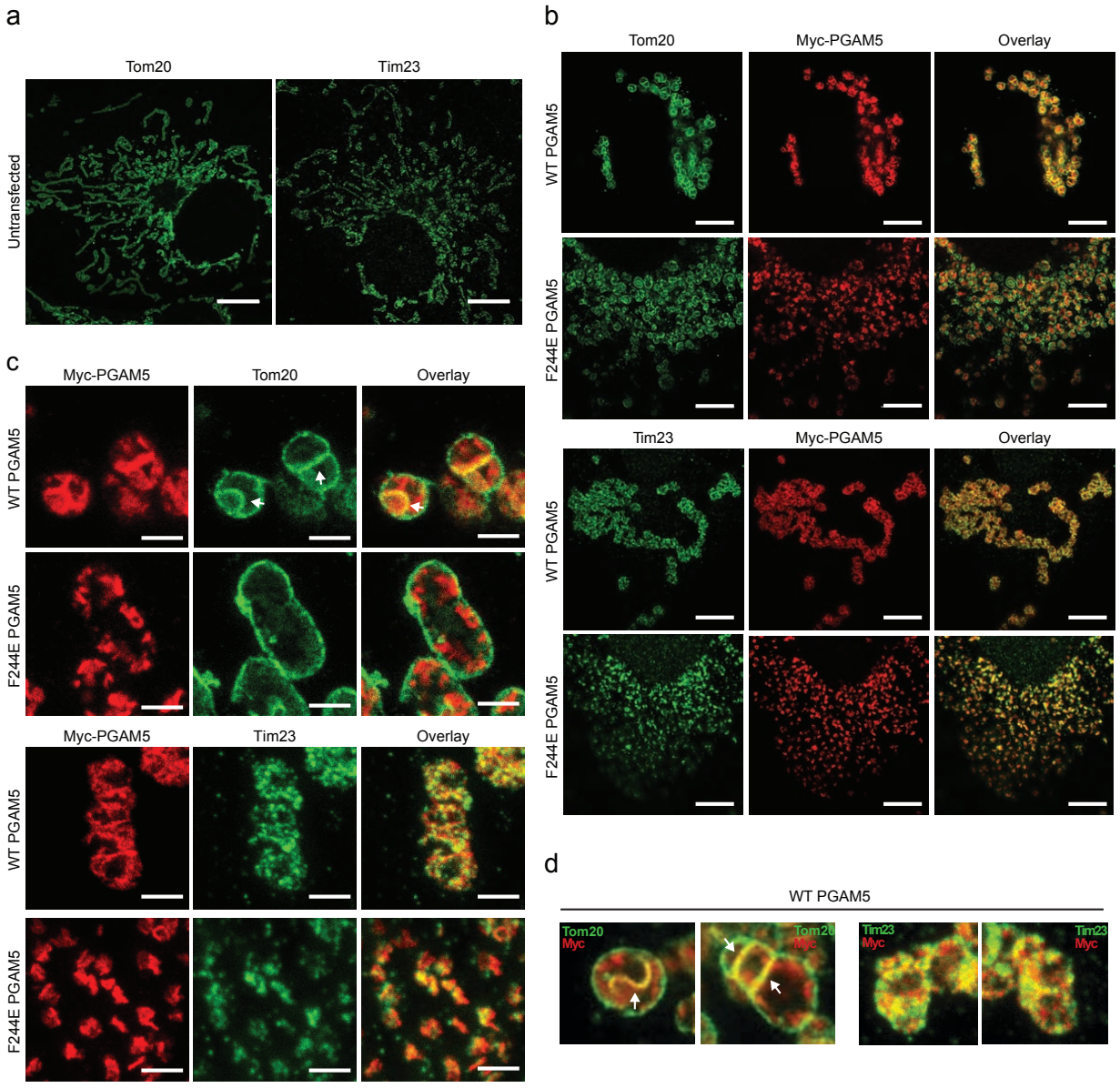

Fig. 2.18: PGAM5 localizes at inner mitochondrial membrane and at the membrane contact sites. a-d. STED images of COS7 cells that were either **a.** untransfected or **b-c.** transiently transfected with wild type (WT) or F244E full-length myc-tagged PGAM5. Tom20 was visualized with anti-Tom20 antibody (green), Tim23 with anti-Tim23 antibody (green) and PGAM5 with anti-myc antibody (red). White arrows indicate contact sites between mitochondrial membranes in which myc-tagged PGAM5 was found colocalized with Tom20. Scale bars correspond to 5 µm in (a), 5 µm in (b) and 1 µm in (c). **d.** Upper panels show representative close-up views of PGAM5 localization to the sites of mitochondrial membrane contacts. White arrows indicate sites of PGAM5 (myc, red) overlap with the outer mitochondria membrane marker Tom20 (green).

2.4 DISCUSSION

Here we investigated activation mechanisms of the PGAM5 phosphatase, whose remarkable spectrum of functions in mitochondria parallels the pleiotropic roles of the organelle itself. We discovered that PGAM5 assembles into symmetric rings in solution that polymerize into filaments. We showed that the ring structure, first observed by Chaikuad and colleagues for a PGAM5 construct containing its linker and phosphatase domains[34], also forms when phosphatase domain without these additional contiguous regions is crystallized in the presence of a peptide corresponding to the multimerization motif. Observation of PGAM5 rings in solution indicates that this form is an energetically favored state of the PGAM5 phosphatase.

Our studies demonstrate that the assembly into the dodecameric ring is an essential determinant of efficient catalytic activation of PGAM5. The multimerization step is critical: the interaction between a multimerization motif within the linker domain and a pair of phosphatase domains is essential for stabilization of the phosphatase in the active state. This interaction is further stabilized by neighboring subunits in the oligomer. The linker domain of PGAM5 mediates several protein-protein interactions, such as binding of KEAP1 and XIAP ubiquitin ligases[5,9] and Bcl-XL[12]. Through such interactions, the linker domain may regulate oligomerization, further tuned by possible post-translational modifications within the linker region. The sufficiency of the presentation of the multimerization motif *in trans* could create a mechanism for propagation of regulatory modifications from one PGAM5 monomer to another, or even between dodecamers, if PGAM5 subunits in the oligomers are capable of exchanging. This could equip PGAM5 with the ability to store information, such as the status of phosphatase domain activation, in a manner analogous to that described for CamKII[40].

The multimeric organization of PGAM5 might also have important implications for its substrate specificity as a phosphatase. Some PGAM5 substrates form higher-order oligomeric structures, including DRP1, which self-assembles into rings or filaments[36,41]. GTP hydrolysis, an important step in mitochondrial constriction by DRP1, is thought to release DRP1 from its mitochondrial receptors and triggers DRP1 filaments to curl into ring-shaped oligomers, often dodecamers[41], analogous to the PGAM5 oligomers that we describe here. Although DRP1 associates with the OMM and PGAM5 resides primarily in IMM, we observed that PGAM5 colocalizes with the OMM marker at contact sites between two adjacent mitochondrial vesicles within the mitochondrial clusters promoted by PGAM5 overexpression. These PGAM5-enriched contact sites may represent a type of membrane fusion or fission intermediate involving the formation of local membrane pores [42-47], which could facilitate interactions between DRP1 and PGAM5.

Mitochondrial morphology and function are tightly linked. The IMM is intricately structured and contains functionally distinct regions, such as inner boundary regions that are close to OMM, cristae invaginations and cristae junctions[48-51]. Formation of inner membrane supercomplexes by IMM proteins, such as adenine nucleotide translocator[52], ATP synthase[50,53] and multiprotein Mitofilin complex (MitOS)[54], is important for structural organization of the functional domains within the IMM. Our data demonstrate that PGAM5 resides primarily in the IMM and acts independently of DRP1 to influence mitochondrial morphology, suggesting that PGAM5 has an intrinsic ability to alter mitochondrial architecture. Furthermore, oligomerization, but not activity, appeared crucial for this ability of PGAM5. Hence, PGAM5 oligomerization within IMM may play a structural role in the maintenance of the functional mitochondrial membrane architecture.

Our finding that cleaved PGAM5 forms filaments composed of dodecameric phosphatase rings both *in vitro* and in cells adds a new dimension of complexity to PGAM5 signaling. Filaments did not influence the catalytic rate of PGAM5 *in vitro* nor the ability of full-length PGAM5 to influence mitochondrial morphology in cells. However, cleaved PGAM5, which accumulates with time in the cytosol, sensitizes cells to apoptosis through sequestration of the negative regulator of apoptosis, the ubiquitin ligase XIAP[9]. Other cytosolic effectors of death pathways form filamentous structures that are essential for executing cell death programs, including the caspase-8 associated death complex[55], the caspase-1 containing inflammasomes[47] and the RIP1/RIP3 necrosomes[56]. PGAM5 filamentation could ensure highly processive or cooperative dephosphorylation in these processes. We found that cytosolic PGAM5 filaments colocalized with microtubules and only formed when microtubules are intact. This phenomenon may relate to the link between PGAM5 and the stability of the Miro2 GTPase, which involves KEAP1 and the formation of a ternary complex with the Nrf2 transcription factor, to control stress-induced retrograde trafficking of mitochondria[35]. It is also possible that PGAM5 filaments formed upon PGAM5 cleavage reside primarily inside the mitochondria, playing yet unknown role(s).

Although we still know little about the regulation of PGAM5 activity, the enhanced phosphatase activity in oligomerization-competent PGAM5 supports the need for tight regulation of this intramolecular interaction. How binding partners or posttranslational modifications regulate PGAM5 catalytic activity and/or oligomerization is a topic of future studies. An exciting possibility is the pharmacological regulation of PGAM5 signaling through regulation of the interaction between the multimerization motif and the phosphatase domain. Compounds mimicking this binding event could be of potential therapeutic interest in the treatment of stroke,

myocardial infarction, and other diseases by stimulating the mitophagy-promoting functions of PGAM5[32].

2.5 METHODS

Protein expression and purification: Wild type full-length PGAM5 cDNA (corresponding to the PGAM5 long isoform (PGAM5L), residues 1-289) was purchased from Addgene. For bacterial expression and purification, the Δ90 PGAM5 (residues 91-289) and Δ48 PGAM5 (residues 49-289) were cloned into the pET28a expression vector (Novagen). These constructs were N-terminally tagged with hexahistidine (6X-HIS) followed by a linker sequence encoding a TEV protease cleavage site (ENLYFQS). Full-length and Δ23 (residues 24-289) PGAM5 variants for mammalian cell expression and imaging were cloned into the pcDNA3.1+ vector (Invitrogen). These constructs contained an internal myc-tag (EQKLISEEDL) inserted between residue 42 and 43 of the PGAM5 sequence. Mutations were introduced using either QuickChange mutagenesis or through Gibson assembly[57]. Primers used for mutagenesis are as follows: H105A (Forward: 5'-acatcttcctcatcagggcttcccagtaccacgtgg-3' Reverse: 5'-ccacgtggtactgggaagccctgatgaggaagatgt-3'), Y198E (F: 5'-gctccgtcttcctcatactgcacagcttccggc-3' R: 5'-gccggaagctgtgcagtatgaggaagacggagc-3'), R65A (F: 5'-agagacagtggttctgccctgtcccagttggg-3' R: 5'-cccaactgggacagggcagaaccactgtctct-3'), F244E (F: 5'-gccagccttcaggaggctcctgcagtgctctgcac-3' R: 5'-gtgcagagcactgcaggagcctcctgaaggctggc-3'), R288E (F: 5'-cctcccgacaagatcactgaatcctgagatccgaattc-3' R: 5'-gaattcggatctcaggattcagtgatcttgtcgggagg-3'). Mutation of WT A4 was done by sequential mutation of W58A and D59A and followed by W62A and D63A. W58A/D59A (F: 5'- gtcccagttgggggccgcgacaccggggccc-3' R: 5'-gggccccggtgtcgcggcccccaactgggac-3'), W62A/D63A (F: 5'- gtggttctcgcctggccgcgttggggtcccaga-3' R: 5'- tctgggaccccaacgcggccaggcgagaaccac-3').

Y92A (F: 5’-cgtggccttggctttggcgtggtccagcttggac-3’ R: 5’-gtccaagctggaccacgccaaagccaaggccacg-3’), D111A (F: 5’-cccagtaccacgtggccggctccctggagaag-3’ R: 5’-cttctccagggagccggccacgtggtactggg-3’), K191A (F: 5’-tgcacagcttccggcgcccaatgagacacggg-3’ R: 5’-cccgtgtctcattgggcgccggaagctgtgca-3’), R218A/E220A (F: 5’-gtaactgtcctccgcctgcgcggc-0=atctgcgcgg-3’ R: 5’-ccgcgcagatgccgcgcaggcggaggacagttac-3’).

For recombinant protein expression, BL21 DE3 pLysS *E. coli* cells transformed with pET28a-PGAM5 constructs were cultured in Luria Broth media supplemented with kanamycin (30 µg/mL) at 37^{o} C until 0.4 optical density at 600 nm was reached. Protein expression was induced with 0.2 mM IPTG and cells were cultured for additional 12 hours at 25^{o} C. Following collection by centrifugation at 5000 x g, cell pellets were resuspended in Lysis Buffer (20 mM Tris-Cl pH 8.0, 500 mM NaCl, 0.5 mM TCEP, 5% glycerol, 20 mM Imidazole pH 8.0 supplemented with EDTA-free protease inhibitors (Roche)). Cells were lysed by sonication at 25% of max power in cycles of 4s on and 2s off for 5 minutes. Lysates were clarified by centrifugation at 18,000 x g and loaded by gravity flow on HiTrap Ni-NTA resin (GE Healthcare). Protein was eluted using Elution Buffer (20 mM Tris-Cl pH 8.0, 500 mM NaCl, 0.5 mM TCEP, 5% glycerol, 200 mM Imidazole pH 8.0) and exchanged into buffer containing 20 mM Tris-Cl pH 8.0, 150 mM NaCl, and 0.5 mM TCEP using a 10 kDa cutoff concentrator (Millipore). The sample was further purified by size exclusion chromatography (SEC) using a Superose 6 10/300 GL Increase column (GE Healthcare) equilibrated in buffer containing 20 mM Tris-Cl pH 8.0, 150 mM NaCl and 0.5 mM TCEP. Salt titration experiments were performed by SEC in buffer conditions containing 20 mM Tris-Cl pH 8.0, 0.5 mM TCEP and concentrations of NaCl ranging from 150 mM to 1 M.

Peptides: The ASK1 phosphopeptide (NFEDH(pS)APPSP) and the PGAM5 multimerization motif (MM) peptide (GPGVWDPNWDRREP)[33], were purchased at a purity of 95% or greater (Elim Biopharma). Peptides were resuspended in 20 mM Tris-Cl pH 7.5, aliquoted, and flash frozen in liquid nitrogen prior to storage at -80° C.

Negative-stain sample preparation and data acquisition: Homemade grids were prepared for negative-stain experiments by depositing a thin plastic layer on the surface of 400-mesh copper grids (Ted Pella) floated on 2% amyl acetate (EMS)[58]. Air-dried grids were then coated with ~3 nm of continuous carbon film, negative glow discharged, and loaded with 2.5 uL of purified PGAM5 (~0.01-0.1 mg/mL). Following a 30s incubation, grids were briefly dipped in 2 drops of sample buffer and one drop of 0.75% uranyl formate staining solution with blotting performed between drops by touching the edge of the grid briefly to the surface of Whatman 1 filter paper. Sample grids were dipped in a second drop of stain for 30 seconds, blotted on filter paper, and air dried prior to imaging. Images were collected using a 120 kV Tecnai T12 (FEI) microscope equipped with a Gatan 4K x 4K CCD camera at 52K magnification corresponding to a pixel size of 2.21Å.

Cryo-EM sample preparation, data acquisition and processing: For cryo-EM experiments, we first screened grid type and protein buffer to identify optimal conditions for data collection. We observed significant orientation bias as well as aggregation on traditional Quantifoil 1.2/1.3 400 mesh spacing gold grids (Electron Microscopy Sciences) that could not be improved by changes in buffer conditions (i.e. varying salt concentration, addition of glycerol, addition of low concentrations of detergent). While aggregation was somewhat alleviated by sample application

on C-flat 1.2/1.3 holey thick carbon grids (Electron Microscopy Sciences), sample quality appeared to be the best for 3 μL of purified PGAM5 sample (at 0.10 mg/mL) in ring stabilization buffer (20 mM Tris-Cl pH 8.0, 600 mM NaCl, 0.5 mM TCEP) applied to freshly glow-discharged Lacey Formvar/Carbon 400 mesh continuous carbon coated copper grids (Ted Pella) placed inside a Vitrobot Mark IV (FEI) equilibrated to 4° C and 100% humidity. Following a 10 second incubation, grids were blotted between Whatman 1 paper for 6 seconds, and plunge-frozen in liquid ethane. Images were recorded using a 300kV Titan Krios microscope (FEI) equipped with a K2 Summit detector (Gatan) operated in super-resolution mode (UC Berkeley). 6543 images were collected at a nominal magnification of 22.5K, corresponding to a pixel size of 0.53 Å. Dose-fractionated movies were acquired at an electron flux of 1.8 e^{-1}/A^2 over 7.75 seconds with 0.25 second exposures per frame (31 frames total), corresponding to a total dose of 55 $e^{-1}/Å^2$. Images were recorded with a defocus range of -1 to 2.5 μm.

Frame-based motion correction, 2X binning, and dose weighting were performed on dose-fractionated image stacks using MotionCor2[59] resulting in one integrated image per stack with a pixel size of 1.07 Å. The contrast transfer function was estimated from motion corrected, non-dose-weighted images using GCTF version 1.06[60]. From an initial subset of micrographs, approximately 1000 particles were manually picked and subject to likelihood-based 2D classification in Relion 2.0[61] to generate templates for automated particle selection using Gautomatch version 0.55[60]. In total, 131,396 particles were extracted at a box size of 190 pixels with 2.14 Å/pixel and subject to 2D-classification to eliminate particles of poor quality resulting in a dataset of 22,422 particles corresponding to orientations in which C6 symmetry of the dodecameric assembly of Δ48 PGAM5 was observed. The final selected particles were re-centered

and re-extracted at full pixel size to generate the class average shown in Fig. 2.3a. Data collection details are reported in Supplementary Table 2.1.

Supplementary Table 2.1 Cryo-EM data collection, refinement and validation statistics

	Δ48 PGAM5
Data collection and processing	
Magnification	22,500
Voltage (kV)	300
Electron exposure (e–/Å^2)	1.8
Defocus range (μm)	-1.0 – 2.5
Pixel size (Å)	0.53
Initial particle images (no.)	131,396
Final particle images (no.)	22,422

X-ray crystallography: The Δ90 H105A PGAM5 construct was crystallized using hanging drop vapor diffusion at room temperature in the presence of the ASK1 phosphopeptide alone or together with the MM peptide. The electron density corresponding to the ASK1 peptide could not be resolved in any of the structures. For crystallization of Δ90 H105A PGAM5 with the ASK1 peptide, protein was concentrated to 5 mg/mL and incubated with the peptide on ice at a 5:1 molar ratio of peptide:protein. Crystals were grown in a 2 μL drop (1 μL protein + 1 μL reservoir solution) against a reservoir solution comprised of 100 mM HEPES pH 7.5, 200 mM $MgCl_2$ and 30% w/v PEG 400. For crystallization of the Δ90 H105A PGAM5 in complex with the MM peptide, protein at a concentration of 7.5 mg/mL was incubated on ice with 3:3:1 molar ratio of ASK1 peptide:multimerization motif peptide:protein. Crystals were grown in 2 μL drops (1 μL protein + 1 μL reservoir solution) equilibrated against reservoir solution containing 100 mM Tris-Cl pH 7.0, 200 mM $MgCl_2$ and 10% w/v PEG 8000. Crystals from both conditions were cryoprotected with Paratone-N oil and flash-cooled to 100 K in liquid nitrogen.

X-ray diffraction data were collected at 1.111 Å, 77K at the ALS 8.3.1. beamline (Berkeley, CA) on a Pilatus 6M detector. Data were indexed with XDS[62], scaled in Aimless[63] and phases determined in Phaser[64]. Δ90 PGAM5 H105A crystals diffracted to 1.7 Å in space group $P2_12_12_1$ and with unit cell dimensions: a = 71.0 Å, b = 72.0 Å, c = 81.9 Å, $\alpha = \beta = \gamma = 90°$ and with two molecules in the asymmetric unit. A solution was generated by molecular replacement using one copy of PDB 3MXO as the search model. Crystals of Δ90 PGAM5 H105A/MM diffracted to 2.6 Å in the space group $P2_12_12_1$ with unit cell dimensions: a = 49.3 Å, b = 242.5 Å, c = 272.5 Å, $\alpha = \beta = \gamma = 90°$ and with twelve molecules in the asymmetric unit. The structure was solved by molecular replacement using a single monomer of PDB 5MUF and searching for 12 copies in the asymmetric unit. Refinement was performed in Phenix[65] with iterative rounds of model building in Coot[66]. Model quality was assessed with MolProbity[67] and coordinates deposited in the RCSB PDB databank under the PDB codes 6CNI [http://dx.doi.org/10.2210/pdb6CNI/pdb] (Δ90 PGAM5 H105A) and 6CNL [http://dx.doi.org/10.2210/pdb6CNI/pdb] (Δ90 PGAM5 H105A/MM). Detailed statistics for data collection and structure refinement reported in Table 1.

Phosphatase activity assay: Phosphatase assays were performed at room temperature for wild type and mutant constructs of 6xHIS-Δ48 PGAM5 (A4, R65A, H105A, Y198E, F244E, R269E, and R288E). ASK1 phosphopeptide was serially diluted (0 – 200 μM) into reaction buffer (20 mM Tris-Cl pH 8.0, 150 mM NaCl and 0.5 mM TCEP) and the assay was started by the addition of PGAM5 (20 nM). The reaction was quenched at various time points with the addition of malachite green (Promega) and the total free phosphate in solution measured as the absorbance at 620 nm. Initial rates and Michaelis-Menten kinetic parameters were calculated in Prism (GraphPad) and are reported in Table 2.

Subcellular fractionation: HEK293T cells (ATCC) cultured under normal conditions were treated with CCCP (50 μM) (Carbonyl cyanide 3-chlorophenylhydrazone, Sigma Aldrich) prepared in complete media for 4 hours prior to harvest. Following treatment, subcellular fractionation of cellular cytoplasm and mitochondria was performed by resuspending harvested cells first with plasma membrane (PM) permeabilization buffer (20 mM HEPES, 100 mM Sucrose, 2.5 mM $MgCl_2$, 100 mM KCl, 10 mM DTT, 0.025% digitonin, pH 7.4) supplemented with DNase (Roche) and complete protease inhibitors without EDTA (Roche). Following incubation at 4° C for 30 minutes with end over end mixing, membrane fractions were separated from cytosol by centrifugation at 4° C and 13,000 x g for 10 minutes. Supernatant was collected as the cytosolic (cyto) fraction. The remaining pellet was washed twice by resuspending in cold PBS and centrifugation at 4° C and 600 x g for 5 minutes in between washes. Resuspended mitochondrial membranes were then solubilized in a volume of mitochondrial permeabilization buffer (20 mM BisTris, 50 mM NaCl, 10% glycerol, 10 mM DTT, 2% digitonin, pH 7.4, supplemented with protease inhibitors) equivalent to the volume of PM buffer used and incubated with end over end mixing for 30 min at 4° C prior to one final centrifugation at 4° C and 13,000 x g for 10 minutes. Supernatant from this fraction was collected as the mitochondrial (mito) fraction. Samples were prepared for SDS-PAGE loading controls and blue native-PAGE (BN-PAGE) by adding equivalent volumes of either standard SDS-PAGE loading dye or 10X BN-PAGE loading dye (100 mM Bis-Tris pH 7.0, 500 mM 6-amino-nexamoic acid, and 5% Coomassie Blue R-250), respectively. Samples for SDS-PAGE were normalized for concentration and subject to immunoblotting with antibodies against PGAM5 (1:3000) (kind gift from Z. Wang), β-tubulin (1:2000) (Cell Signaling Technologies, Inc., 2128S), and Tom20 (1:100) (Santa Cruz

Biotechnologies, Inc., sc-17764). Uncropped scans of blots shown in Fig. 2.11a are included in the supplementary information (Supplementary Figure 6).

Blue Native-PAGE: BN-PAGE was performed for equivalent volumes of the total fractionation sample supplemented with BN-PAGE loading dye[68,69]. Samples were loaded onto a 4-16% Native-PAGE gel (Invitrogen) and electrophoresed under 8 mA of constant current in blue cathode buffer (Invitrogen) until the dye front had migrated approximately one-third of the way through the resolving gel. Next, the blue cathode buffer was replaced with clear anode buffer (Invitrogen) and electrophoresis continued at 150V for 60 minutes, then increased to 250V for the remainder of the experiment (45 minutes). Prior to transfer to PVDF (Millipore) and immunoblotting, the native gels was soaked for 10 minutes in Tris-glycine transfer buffer supplemented with 20% methanol and 0.05% SDS. Following the transfer, the PVDF membrane was completely destained in 100% methanol, then equilibrated in blocking buffer (5% w/v milk prepared in TBST buffer) prior to immunoblotting with anti-PGAM5 antibody.

Confocal imaging: Monkey kidney COS7 cells (obtained from J. Kuriyan, UC Berkeley) were cultured at 37° C in 5% CO_2 with DMEM supplemented with 10% FBS, and 1% Penicillin-Streptomycin (Thermo Fisher). Mouse embryonic fibroblasts (obtained from D. Chan, Caltech) were cultured at 37° C in 5% CO_2 with DMEM supplemented with 10% FBS, 100 μM Non-Essential Amino Acids and 1% Penicillin-Streptomycin (Thermo Fisher). For imaging, COS7 and MEF cells were plated at a density of 0.9 x 10^5 cells per well in a 6 well plate (Corning) on acid-washed glass coverslips and grown for 16 hours at 37°C. Cells were then transfected with 500 ng of full-length or cleaved (Δ23) PGAM5 using Lipofectamine 3000 (Invitrogen) and incubated for

24 hours at 37° C. For nocodazole treatments, relevant cells were incubated with 10 μM nocodazole in media for 45 minutes at 37° C. Following transfection and drug treatment, cells were washed with cold PBS, and fixed with 3.7% formaldehyde for 1 hour at room temperature. After three rinses with PBS, cells were permeabilized with 0.1% Triton X-100 for 5 minutes, then washed three times with PBS. Permeabilized cells were incubated with the blocking buffer (1% BSA in PBS) for 5 minutes at room temperature, then for 1 hour at 37° C with blocking buffer supplemented with primary antibodies. Those included anti-myc (mouse, 1:6000 dilution in blocking buffer) (Millipore, 05-724), anti-Tom20 (rabbit, 1:250) (Santa Cruz Biotechnology, SC-17764), anti-β-tubulin (rabbit, 1:25) (Cell Signaling Technologies, 2128S), anti-β-tubulin (rabbit, 1:250) (Abcam, Ab179513) or Alexa Fluor-647 Phalloidin (1:20) (Thermo Fischer, A22287). For Tim23 labeling, blocking buffer contained 10% FBS and primary labeling used Anti-Tim23 antibody (rabbit, 1:250) (Proteintech, 11123-1-AP). Coverslips were washed three times with PBS and incubated with respective secondary antibodies: FITC-488 (rabbit, 1:500) (Invitrogen, A-11034) and Alexa-647 (mouse, 1:500) (Invitrogen, A327728) for 1 hour at 37° C in the dark. Following three washes with PBS, samples were incubated with the nuclei stain DAPI (1:1000 dilution in water) (Thermo Fischer, D1306) for 5 minutes at room temperature. Following three final water washes to remove excess DAPI, coverslips were mounted using ProLong Gold (Invitrogen) and dried overnight at room temperature in the dark. Imaging was done using a Nikon TIRF microscope with a Yokagawa CSU-X1 spinning disk confocal consisting of 405, 491, 561 and 640 nm lasers with the use of a 60x objective. Data were processed using FIJI v1.0 (55).

Structure illumination imaging (SIM): COS7 cells for SIM imaging were cultured, transfected, and prepared for imaging as for confocal microscopy. Slides were imaged on an N-SIM (OMX

microscope with 405nm, 488nm, 561nm and 640nm lasers) using an Apo TIRF 100x objective with 1.56 oil in 3D mode and standard operating procedure. Image reconstruction was performed in SoftWoRx v6.5.2 (GE Healthcare).

Stimulated Emission Depletion (STED) imaging: COS7 cells for STED imaging were cultured, transfected, and prepared for imaging as for confocal and SIM microscopy, however using different secondary antibodies: secondary Alexa-594 (rabbit, 1:500) (Invitrogen, R37117) and Alexa-647 (mouse, 1:500) (Invitrogen) antibodies. Images were acquired using a Leica Stimulated Emission Depletion (STED) SP8 microscope (equipped with a white light laser, a 775 nm depletion laser and 100x objective HC PL APO 100x/1.40 OIL) using standard operating procedure. Images were processed in FIJI v1.0[70].

2.6 ACKNOWLEDGEMENTS

We thank the staff at ALS 8.3.1 beamline for assisting with X-ray diffraction experiments, D. Castaneda-Castellanos for assistance with STED imaging, D. Larsen and K. Herrington for assistance with confocal and SIM imaging, and P. Littlefield for experimental assistance at early stages of the project. We are grateful to Z. Wang for providing the anti-PGAM5 antibody[24] and D. Chan for providing the *Drp1*$^{-/-}$ MEFs. We also thank M. Braunfeld, M. Harrington, D. Bulkley, and A. Myasnikov of the UCSF Center for Advanced CryoEM and P. Tobias of the Berkeley Bay Area CryoEM Facility, which are supported in part from NIH grants S10OD020054 and 1S10OD021741 and the Howard Hughes Medical Institute (HHMI). We also thank the QB3 shared cluster and NIH grant 1S10OD021596-01 for computational support. Lastly, we thank P. Thomas, R. Kalia and the members of the Jura and Frost for critical reading of the manuscript and insightful

discussions. This work was supported by grants from the UCSF Program for Breakthrough Biomedical Research (PBBR) to N.J. and A.F., a Faculty Scholar grant from the HHMI to A.F., NIH grant 1DP2GM110772-01 to A.F., the UCSF Genentech Fellowship to K.R, the UCSF/NIGMS IMSD Fellowship to K.R, and UCSF Discovery Fellowship to K.R. A.F. is a Chan Zuckerberg Biohub investigator.

2.7 REFERENCES

1. Rigden, D.J. The histidine phosphatase superfamily: structure and function. *Biochem J* **409**, 333-48 (2008).
2. Jedrzejas, M.J. Structure, function, and evolution of phosphoglycerate mutases: comparison with fructose-2,6-bisphosphatase, acid phosphatase, and alkaline phosphatase. *Prog Biophys Mol Biol* **73**, 263-87 (2000).
3. Takeda, K. et al. Mitochondrial phosphoglycerate mutase 5 uses alternate catalytic activity as a protein serine/threonine phosphatase to activate ASK1. *Proc Natl Acad Sci U S A* **106**, 12301-5 (2009).
4. Panda, S. et al. Identification of PGAM5 as a Mammalian Protein Histidine Phosphatase that Plays a Central Role to Negatively Regulate CD4(+) T Cells. *Mol Cell* **63**, 457-69 (2016).
5. Lo, S.C. & Hannink, M. PGAM5 tethers a ternary complex containing Keap1 and Nrf2 to mitochondria. *Exp Cell Res* **314**, 1789-803 (2008).
6. Sekine, S. et al. Rhomboid protease PARL mediates the mitochondrial membrane potential loss-induced cleavage of PGAM5. *J Biol Chem* **287**, 34635-45 (2012).
7. Lu, W. et al. Genetic deficiency of the mitochondrial protein PGAM5 causes a Parkinson's-like movement disorder. *Nat Commun* **5**, 4930 (2014).
8. Saita, S. et al. PARL mediates Smac proteolytic maturation in mitochondria to promote apoptosis. *Nat Cell Biol* **19**, 318-328 (2017).
9. Zhuang, M., Guan, S., Wang, H., Burlingame, A.L. & Wells, J.A. Substrates of IAP ubiquitin ligases identified with a designed orthogonal E3 ligase, the NEDDylator. *Mol Cell* **49**, 273-82 (2013).

10. Wai, T. et al. The membrane scaffold SLP2 anchors a proteolytic hub in mitochondria containing PARL and the i-AAA protease YME1L. *EMBO Rep* **17**, 1844-1856 (2016).

11. Bernkopf, D.B. et al. Pgam5 released from damaged mitochondria induces mitochondrial biogenesis via Wnt signaling. *J Cell Biol* (2018).

12. Lo, S.C. & Hannink, M. PGAM5, a Bcl-XL-interacting protein, is a novel substrate for the redox-regulated Keap1-dependent ubiquitin ligase complex. *J Biol Chem* **281**, 37893-903 (2006).

13. O'Mealey, G.B. et al. A PGAM5-KEAP1-Nrf2 complex is required for stress-induced mitochondrial retrograde trafficking. *J Cell Sci* **130**, 3467-3480 (2017).

14. Imai, Y. et al. The loss of PGAM5 suppresses the mitochondrial degeneration caused by inactivation of PINK1 in Drosophila. *PLoS Genet* **6**, e1001229 (2010).

15. Matsuda, N. et al. PINK1 stabilized by mitochondrial depolarization recruits Parkin to damaged mitochondria and activates latent Parkin for mitophagy. *J Cell Biol* **189**, 211-21 (2010).

16. Vives-Bauza, C. et al. PINK1-dependent recruitment of Parkin to mitochondria in mitophagy. *Proc Natl Acad Sci U S A* **107**, 378-83 (2010).

17. Geisler, S. et al. PINK1/Parkin-mediated mitophagy is dependent on VDAC1 and p62/SQSTM1. *Nat Cell Biol* **12**, 119-31 (2010).

18. Narendra, D.P. et al. PINK1 is selectively stabilized on impaired mitochondria to activate Parkin. *PLoS Biol* **8**, e1000298 (2010).

19. Chen, G. et al. A regulatory signaling loop comprising the PGAM5 phosphatase and CK2 controls receptor-mediated mitophagy. *Mol Cell* **54**, 362-77 (2014).

20. Gispert, S. et al. Parkinson phenotype in aged PINK1-deficient mice is accompanied by progressive mitochondrial dysfunction in absence of neurodegeneration. *PLoS One* **4**, e5777 (2009).

21. Glasl, L. et al. Pink1-deficiency in mice impairs gait, olfaction and serotonergic innervation of the olfactory bulb. *Exp Neurol* **235**, 214-27 (2012).

22. Kitada, T. et al. Impaired dopamine release and synaptic plasticity in the striatum of PINK1-deficient mice. *Proc Natl Acad Sci U S A* **104**, 11441-6 (2007).

23. Valente, E.M. et al. Hereditary early-onset Parkinson's disease caused by mutations in PINK1. *Science* **304**, 1158-60 (2004).

24. Wang, Z., Jiang, H., Chen, S., Du, F. & Wang, X. The mitochondrial phosphatase PGAM5 functions at the convergence point of multiple necrotic death pathways. *Cell* **148**, 228-43 (2012).

25. Ishida, Y. et al. Prevention of apoptosis by mitochondrial phosphatase PGAM5 in the mushroom body is crucial for heat shock resistance in Drosophila melanogaster. *PLoS One* **7**, e30265 (2012).

26. Moriwaki, K. et al. The Mitochondrial Phosphatase PGAM5 Is Dispensable for Necroptosis but Promotes Inflammasome Activation in Macrophages. *J Immunol* **196**, 407-15 (2016).

27. Murphy, J.M. et al. The pseudokinase MLKL mediates necroptosis via a molecular switch mechanism. *Immunity* **39**, 443-53 (2013).

28. Remijsen, Q. et al. Depletion of RIPK3 or MLKL blocks TNF-driven necroptosis and switches towards a delayed RIPK1 kinase-dependent apoptosis. *Cell Death Dis* **5**, e1004 (2014).

29. Moujalled, D.M., Cook, W.D., Murphy, J.M. & Vaux, D.L. Necroptosis induced by RIPK3 requires MLKL but not Drp1. *Cell Death Dis* **5**, e1086 (2014).

30. He, G.W. et al. PGAM5-mediated programmed necrosis of hepatocytes drives acute liver injury. *Gut* **66**, 716-723 (2017).

31. Xu, W. et al. Bax-PGAM5L-Drp1 complex is required for intrinsic apoptosis execution. *Oncotarget* **6**, 30017-34 (2015).

32. Lu, W. et al. Mitochondrial Protein PGAM5 Regulates Mitophagic Protection against Cell Necroptosis. *PLoS One* **11**, e0147792 (2016).

33. Wilkins, J.M., McConnell, C., Tipton, P.A. & Hannink, M. A conserved motif mediates both multimer formation and allosteric activation of phosphoglycerate mutase 5. *J Biol Chem* **289**, 25137-48 (2014).

34. Chaikuad, A. et al. Structures of PGAM5 Provide Insight into Active Site Plasticity and Multimeric Assembly. *Structure* **25**, 1089-1099 e3 (2017).

35. O'Mealey, G.B. et al. A PGAM5-KEAP1-Nrf2 complex is required for stress-induced mitochondrial retrograde trafficking. *J Cell Sci* (2017).

36. Ingerman, E. et al. Dnm1 forms spirals that are structurally tailored to fit mitochondria. *J Cell Biol* **170**, 1021-7 (2005).

37. Osellame, L.D. et al. Cooperative and independent roles of the Drp1 adaptors Mff, MiD49 and MiD51 in mitochondrial fission. *J Cell Sci* **129**, 2170-81 (2016).

38. Ishihara, N. et al. Mitochondrial fission factor Drp1 is essential for embryonic development and synapse formation in mice. *Nat Cell Biol* **11**, 958-66 (2009).

39. Wakabayashi, J. et al. The dynamin-related GTPase Drp1 is required for embryonic and brain development in mice. *J Cell Biol* **186**, 805-16 (2009).

40. Stratton, M. et al. Activation-triggered subunit exchange between CaMKII holoenzymes facilitates the spread of kinase activity. *Elife* **3**, e01610 (2014).

41. Kalia, R. et al. Structural basis of mitochondrial receptor binding and constriction by DRP1. *Nature* **558**, 401-405 (2018).

42. Engel, A. & Walter, P. Membrane lysis during biological membrane fusion: collateral damage by misregulated fusion machines. *J Cell Biol* **183**, 181-6 (2008).

43. Papanicolaou, K.N., Phillippo, M.M. & Walsh, K. Mitofusins and the mitochondrial permeability transition: the potential downside of mitochondrial fusion. *Am J Physiol Heart Circ Physiol* **303**, H243-55 (2012).

44. Katsov, K., Muller, M. & Schick, M. Field theoretic study of bilayer membrane fusion: II. Mechanism of a stalk-hole complex. *Biophys J* **90**, 915-26 (2006).

45. Marrink, S.J. & Mark, A.E. The mechanism of vesicle fusion as revealed by molecular dynamics simulations. *J Am Chem Soc* **125**, 11144-5 (2003).

46. Muller, M., Katsov, K. & Schick, M. New mechanism of membrane fusion. *Journal of Chemical Physics* **116**, 2342-2345 (2002).

47. Noguchi, H. & Takasu, M. Fusion pathways of vesicles: A Brownian dynamics simulation. *Journal of Chemical Physics* **115**, 9547-9551 (2001).

48. Reichert, A.S. & Neupert, W. Contact sites between the outer and inner membrane of mitochondria-role in protein transport. *Biochim Biophys Acta* **1592**, 41-9 (2002).

49. Perkins, G.A. & Frey, T.G. Recent structural insight into mitochondria gained by microscopy. *Micron* **31**, 97-111 (2000).

50. Strauss, M., Hofhaus, G., Schroder, R.R. & Kuhlbrandt, W. Dimer ribbons of ATP synthase shape the inner mitochondrial membrane. *EMBO J* **27**, 1154-60 (2008).

51. Nunnari, J. & Suomalainen, A. Mitochondria: in sickness and in health. *Cell* **148**, 1145-59 (2012).

52. Claypool, S.M., Oktay, Y., Boontheung, P., Loo, J.A. & Koehler, C.M. Cardiolipin defines the interactome of the major ADP/ATP carrier protein of the mitochondrial inner membrane. *J Cell Biol* **182**, 937-50 (2008).

53. Paumard, P. et al. The ATP synthase is involved in generating mitochondrial cristae morphology. *EMBO J* **21**, 221-30 (2002).

54. Barbot, M. et al. Mic10 oligomerizes to bend mitochondrial inner membranes at cristae junctions. *Cell Metab* **21**, 756-63 (2015).

55. Fu, T.M. et al. Cryo-EM Structure of Caspase-8 Tandem DED Filament Reveals Assembly and Regulation Mechanisms of the Death-Inducing Signaling Complex. *Mol Cell* **64**, 236-250 (2016).

56. Li, J. et al. The RIP1/RIP3 necrosome forms a functional amyloid signaling complex required for programmed necrosis. *Cell* **150**, 339-50 (2012).

57. Gibson, D.G. et al. Enzymatic assembly of DNA molecules up to several hundred kilobases. *Nat Methods* **6**, 343-5 (2009).

58. Booth, D.S., Avila-Sakar, A. & Cheng, Y. Visualizing proteins and macromolecular complexes by negative stain EM: from grid preparation to image acquisition. *J Vis Exp* (2011).

59. Zheng, S.Q. et al. MotionCor2: anisotropic correction of beam-induced motion for improved cryo-electron microscopy. *Nat Methods* **14**, 331-332 (2017).

60. Zhang, K. Gctf: Real-time CTF determination and correction. *J Struct Biol* **193**, 1-12 (2016).

61. Kimanius, D., Forsberg, B.O., Scheres, S.H. & Lindahl, E. Accelerated cryo-EM structure determination with parallelisation using GPUs in RELION-2. *Elife* **5**(2016).

62. Kabsch, W. Integration, scaling, space-group assignment and post-refinement. *Acta Crystallogr D Biol Crystallogr* **66**, 133-44 (2010).

63. Otwinowski, Z. & Minor, W. Processing of X-ray diffraction data collected in oscillation mode. *Methods Enzymol* **276**, 307-26 (1997).

64. McCoy, A.J. et al. Phaser crystallographic software. *J Appl Crystallogr* **40**, 658-674 (2007).

65. Adams, P.D. et al. PHENIX: a comprehensive Python-based system for macromolecular structure solution. *Acta Crystallogr D Biol Crystallogr* **66**, 213-21 (2010).

66. Emsley, P. & Cowtan, K. Coot: model-building tools for molecular graphics. *Acta Crystallogr D Biol Crystallogr* **60**, 2126-32 (2004).

67. Chen, V.B. et al. MolProbity: all-atom structure validation for macromolecular crystallography. *Acta Crystallogr D Biol Crystallogr* **66**, 12-21 (2010).

68. Wittig, I., Braun, H.P. & Schagger, H. Blue native PAGE. *Nat Protoc* **1**, 418-28 (2006).

69. Ma, S. et al. Assembly of the Bak apoptotic pore: a critical role for the Bak protein alpha6 helix in the multimerization of homodimers during apoptosis. *J Biol Chem* **288**, 26027-38 (2013).

70. Schindelin, J. et al. Fiji: an open-source platform for biological-image analysis. *Nat Methods* **9**, 676-82 (2012).

71. Baker, N.A., Sept, D., Joseph, S., Holst, M.J. & McCammon, J.A. Electrostatics of nanosystems: application to microtubules and the ribosome. *Proc Natl Acad Sci U S A* **98**, 10037-41 (2001).

Chapter 3:

Identification and characterization of novel PGAM5 modulators

This work was done in collaboration with Trent Balius, PhD from Brian Shoichet's lab at UCSF. Contributions are as follows: Karen Ruiz, Trent Balius and Natalia Jura developed the project. Karen Ruiz expressed, optimized and purified each of the protein constructs, performed cell-based flow cytometry experiments, compound testing, activity assays, X-ray crystallography acquisition, processing and data analysis. Trent Balius designed and refined the compounds and provided experimental feedback. Christopher Agnew helped with X-ray crystallography data acquisition and processing and performed control BMPR2 kinase assay. Natalia Jura contributed to the project development and data analysis.

3.1 Introduction

Phosphoglycerate mutase 5 has continued to develop as an interesting subject of study for its wide variety of cellular roles, its unique mechanism of activation, and its cellular migration. Despite the strides in our collective understanding of PGAM5, many questions still surround this atypical protein phosphatase. PGAM5 has been well established as a participator in various cell stress and death pathways[1-6] and has been implicated as a key regulator of mitochondrial dynamics through its activity as a protein phosphatase and as a protein binding partner[7,8], yet all of these identified connections lack information on and cellular context of PGAM5's oligomeric status and leave us without a way to effectively modulate this phosphatase's higher order structure formation. PGAM5's cellular localization has been pinpointed to the mitochondria, and its cleavage from the membrane and release into the cytosol has been established, however, whether PGAM5 natively exists as a single monomer, a constitutive dimer, a dodecamer or higher order structure when docked to the mitochondria has not yet been studied. Similarly, PGAM5's catalytic activity, if any, while in a membrane-tethered state has yet to be elucidated. These same questions remain open with regard to PGAM5's wide range of binding partners and protein substrates both inside the mitochondria and in the cytosol; despite the identifications of these interactions, the oligomeric state of PGAM5 remains a mystery. It remains a possibility that PGAM5's interactions with its wide variety of protein binding partners and its ability to function as a signaling node between mitochondrial homeostasis and cell death could be regulated by its various multimeric states.

Our findings have verified earlier reports that PGAM5's phosphatase activity is dependent on its ability to form higher order structures and this activity is directly linked to its ability to oligomerize[9].The exact physiological role this oligomerization plays in the cell is still unknown and would require spatial and temporal separation of PGAM5's various oligomeric states.

PGAM5's multiple cellular functions, combined with its ability to self-regulate its phosphatase activity through higher order structure formation, however, make it technically challenging to parse PGAM5's multiple functions and understand the various ways in which PGAM5 regulates the mitochondria and contributes to cell death. Our observation that PGAM5's ability to remodel the mitochondrial membrane is independent from its interactions with Drp1 lead us to wonder how PGAM5 is able to remodel the mitochondrial membrane seemingly only through its ability to form higher order structures and add another layer of complexity to understanding PGAM5's role in the mitochondria. Now that we understand PGAM5 is able to self-associate into dimers, observe dimers are able to adjacently interact to form dodecamers, these dodecamers have the ability to polymerize, one of the most pressing questions in the PGAM5 and mitochondrial field is how PGAM5's multiple states are regulated in its different cellular contexts, considering PGAM5's higher order structure formation is directly tied to its phosphatase activity, and given its migratory abilities. To address these questions, our lab has begun a collaboration with the Shoichet lab at UCSF to develop and test novel regulators of PGAM5's oligomeric states.

3.2 RESULTS

Effect of PGAM5 on cell death

An interesting phenomenon observed visually during our confocal imagining experiments with cells expressing wild type Δ23 PGAM5 was that transfected slides showed a higher than average amount of cell death following transfection. This observation across different experiments led us to question whether expression of this construct could in some way contribute to cell death. In order to explore the role cleaved PGAM5 has on the cell when it is no longer localized to the mitochondria, we generated and expressed a 'cleaved' construct of PGAM5 lacking the

transmembrane domain and compared the effect on cell viability against a full-length construct. To this end, both full-length and cleaved Δ23 PGAM5 were cloned into a GST-containing pIRES2 vector[10], allowing for further study of the downstream effects of PGAM5 cleavage and release from the mitochondria.

In order to quantify and compare the effects of PGAM5 cleavage on cell health, we expressed the truncated Δ23 construct of PGAM5 in immortalized suspension human T lymphocyte Jurkat cells. As a control, we also expressed full length PGAM5 containing an intact mitochondrial targeting sequence in parallel. 24 hours post-transfection, flow cytometry was used to separate transfected cells expressing PGAM5 and GPF from untransfected cells. The presence of phosphatidylserine on the outer leaflet of the plasma membrane was used to detect and quantify the cells undergoing apoptosis through the use of Annexin V stain. Use of GFP and Annexin V allowed for us to calculate the amount of transfected cells in each experiment through the presence of GPF and further subgroup them into living cells with little to no expression of phosphatidylserine or dying cells presenting phosphatidylserine on the outer leaflet of the cell, as indicated by high Annexin V signal. Expression of full-length mitochondrially tethered PGAM5 results in an average of 25% cell death, while expression of our Δ23 construct lacking the transmembrane domain resulted in an average of 60% cell death as indicated by the total percent dead Jurkat cells (Fig. 3.1). In order to test whether this increase in cell death was due to PGAM5's phosphatase activity, we introduced the catalytic mutation H105A into both the full length and truncated Δ23 constructs and observed no difference in the amount cell death, suggesting the ability of PGAM5 to mediate cell death is dependent on its catalytic ability. Interested in whether this observed increase in cell death is caused by PGAM5's ability to dodecamerize or form filaments, we introduced our dimerization, dodecamerization and filamentation mutations into the

full length and Δ23 cleaved construct, expressed and compared the resulting amount of cell death. Similar to expression of catalytically dead truncated PGAM5, expression of Δ23 cleaved dimer mutant F244E or Δ23 cleaved WT A4 results in no increase in cell death, further validating the requirement of PGAM5's phosphatase activity as a key role in its ability to result in cell death. In an effort to parse whether this was directly tied to PGAM5's ability to form dodecamers or ability to filament, we expressed R288E in full length and cleaved form, and observed that expression of the cleaved form of R288E does not result in a higher incidence of cell death, suggesting that filamentation is somehow correlated with cell death. Interestingly, we observed that expression of Y198E, the mutant able to ablate dodecamer formation through disruption of the α3 helix interaction results in a higher incidence of cell death in the cleaved form. While puzzling, this result suggests PGAM5-mediated cellular death is dependent on filament formation.

While interesting, our findings bring up further questions surrounding the role of PGAM5 oligomerization in the cell. Our observations that PGAM5's ability to form a higher order oligomer is be tied to its ability to cause cell death make it essential to have tools to finely regulate its phosphatase activity and higher order oligomerization. We are currently only able to regulate PGAM5's higher order structure formation with point mutations and would require chemical tools in the form of small molecules to probe PGAM5 formation of filaments and higher order structures in detail. To this end, we began a collaboration with a computational biology lab to identify such molecules.

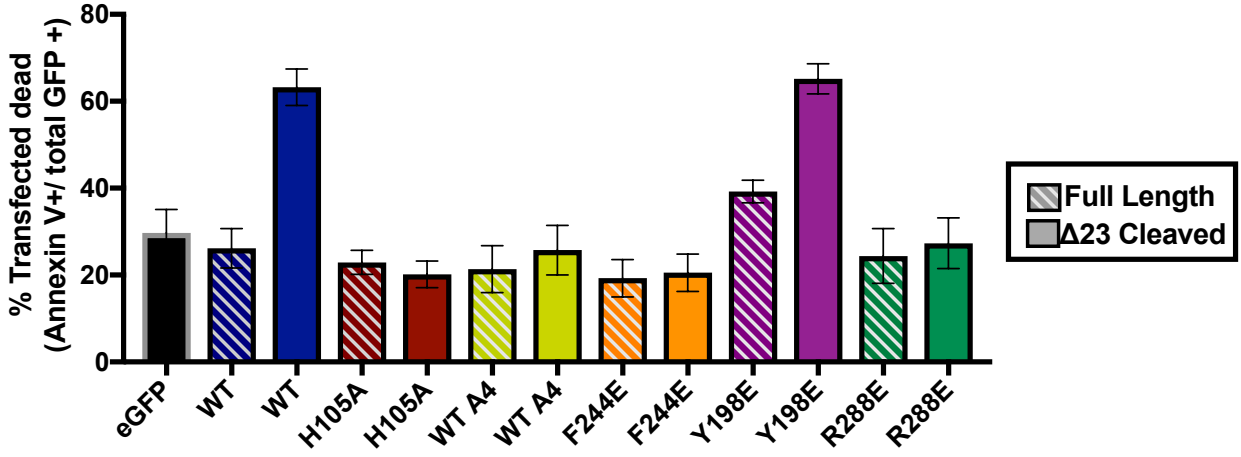

Figure 3.1: Quantification of Jurkat cell death in the presence PGAM5 expression. Percentage of transfected cells that have been identified as dead expressing full length PGAM5 expressing cells indicated in striped bars, while cleaved Δ23 PGAM5 expressing cells indicated in colored bars.

Compound identification and testing

As with the majority of other phosphatases, there are no known drug modulators of PGAM5 commercially available, a technological hurdle that makes studying PGAM5 more challenging but one which we sought to address with our newfound structural insights. In our earlier work, we have shown that activation of PGAM5's phosphatase activity is dependent on the specific interaction between the phosphatase domain and the adjacent multimerization motif localized in the linker region of the protein. By analyzing our crystal structure of PGAM5, we were able to observe the interaction of the multimerization motif with its catalytic core induces the formation of a small allosteric pocket in the phosphatase domain and presents a potential site for drug modulation. Formation of this pocket introduces a novel way to regulate PGAM5's activity through the identification and optimization of chemical compounds to activate or inhibit PGAM5's phosphatase activity. This more detailed understanding of the molecular mechanism through

which PGAM5's activity is regulated, and PGAM5's role in a myriad of mitochondrial and cellular roles, make it a compelling drug target and a region of interest for our studies.

PGAM5's catalytic activation requires the specific interaction between the catalytic core, the PGAM domain, with the adjacent multimerization motif (MM) tucked inside the linker domain. This interaction is unique and presents the perfect modulation site, as the multimerization motif sequence is a conserved unique feature of PGAM5 not found in the rest of the phosphoglycerate mutase family, even in the Sts phosphatases which have been found to similarly dimerize and which possess tyrosine phosphatase activity[11].

In an effort to generate a chemical toolkit with which to regulate PGAM5 activity, we formed a collaboration with the lab of Dr. Brian Shoichet at UCSF and worked in collaboration with Trent Balius to identify and test compounds to inhibit PGAM5's higher order structure formation and phosphatase activity. To this end, we employed the use of the *in silico* screening platform DOCK[12,13] and the ZINC15 database of virtual compounds[14] to identify possible compounds that may interact with the allosteric pocket of PGAM5. Various iterations of DOCK exist, the original established in the Kuntz lab in the early 1980's at UCSF[15], which later segmented, and two branches are current in development: DOCK 6.9 and DOCK3.7. DOCK3.7, optimized from DOCK 3 branch and currently developed in the Shoichet lab, was used to identify and test preliminary potential ligand candidates to PGAM5's allosteric pocket. To perform a virtual screen with DOCK3.7 for PGAM5, we first performed the preliminary ligand and receptor preparation steps followed by orienting and scoring as outlined in the following.

Ligand preparation. To prepare the ligands for sampling, the internal degrees of freedom as measured by the rotatable bonds and torsion angles for each must were identified and pre-computed prior to introduction of the ligand to the receptor. The conformational sampling was

generated about an unvarying part of the ligand, most often a ring, creating a hierarchy. Up to three hierarchies, in the form of three rings, were generated for each molecule.

Receptor Preparation. In order to prepare the receptor for ligand binding simulations, we selected a binding site of interest and used hotspots in the shapes of spheres to define the binding site of interest. These spheres were generated by combining a crystallographic ligand with spheres that defined the inverse image of the pocket, which in turn was generated with Sphgen. To generate potential modifiers of PGAM5, we used the side chains of residues Trp58, Trp62, Asp43 and Arg65 of the multimerization motif rather than the backbone to define the pocket for 6CNL. To define the pocket of the 3MXO structure, we similarly relied on use of side chain residues, in this case using Met89 and Tyr92, which overlap with the multimerization motif binding site. Missing regions for 3MXO were added with Modeller and AMBER to minimize the model, while crystallographic coordinates were unmodified for 6CNL. After we defined the pocket of interest, we generated energetic grids about the spheres to define the bounding box by pre-computing the energetic properties of the binding site. These energetic grids were generated by placing a dummy atom at each grid point and subsequently calculating the energetics between that dummy atom with the whole receptor protein. Use of the pre-computed grids allowed for more rapid evaluation of energies during docking. By using grids to precompute the energies, we were able to substantially speed up our scoring calculations within the docking program. Three different grids were used to generate Van der Waals, electrostatic and ligand desolvation grids. Van der Waals and ligand desolvation grids were generated with the dock accessory programs ChemGrid and SolvMap, respectively, while the electrostatics grid was generated with Qnifft. Once the receptors were prepared, we moved on to orientation and scoring of possible modifiers of PGAM5.

Orienting and scoring. Orientation sampling and scoring were performed within the DOCK3.7 program. We used DOCK3.7 to first identify possible matches between atoms of the unvarying part of the ligand and the spheres by comparing their internal distances. Using this technique, many possible matches were generated. DOCK3.7 then subsequently oriented potential matches by orienting the unvarying segment of the ligand into the receptor binding site, placing the matched atoms onto the matched spheres, along with the rest of the ligand hierarchy. The orienting step was performed for all viable matches; multiple orientations were generated for each hierarchy. Scores for all orientations and conformations of the potential ligand were then calculated on the precomputed grid. Generation of this score served as a crude approximation of binding energy and was made up of three different terms: Van der Waals, electrostatic and ligand desolvation. The Van der Waals term served to highlight shape complementarity as well as quality of fit, the electrostatic term served to estimate charge complementarity while ligand desolvation represented the cost of displacing waters from the ligand. Overall, this generated score was used to select the best poses for each ligand and generate a rank for the possible candidate molecules. The molecules with the best scores were selected for further analysis.

By using these techniques, we performed virtual screens against PGAM5 to identify candidate molecules that may be able to interact with PGAM5's allosteric pocket for experimental testing. Two different PGAM5 structures were prepared and four docking calculations were run. Our dodecameric active structure (PDB: 6CNL) and the pre-existing inactive dimer (PDB: 3MXO) structure were both prepared for docking using the above technique. The ZINC15 database, containing 169 million lead-like molecules and 11.5 million fragments, was screened. Four initial docking calculations were performed: for both PGAM5 structures, we docked both lead-like molecules and fragments to the allosteric pocket.

For each screen, to group chemotypes together, the top 300,000 molecules were clustered using ecfp4 fingerprints in Chemaxon, Tc calculations and a best first clustering scheme to narrow down the list of possible candidate molecules. The top 1000 cluster heads were then subsequently visualized in the context of the receptor using the ViewDock module in UCSF Chimera. Candidate molecules were eliminated through visual inspection for the following reasons: (1) the molecule existed in an unreasonable protomer or tautomer, (2) the molecule had internal strain in the form of internal clashes or odd geometry, (3) the molecule had one or more stranded hydrogen bond donor, (4) the molecule had two or more stranded hydrogen bond acceptors. In addition to these inspection guidelines, (5) the molecule's quality of fit and (6) the molecule's quality of polar interactions in the form of hydrogen bonding were also evaluated for in selecting the top candidates for possible PGAM5 modulation.

The best 17-23 molecules from each of the screens were presented in a hit picking party and assigned a grade by five experts from the Shoichet lab to narrow down the list of possible candidates to the 30 most promising molecules. These molecules where ordered from Enamine for make-on-demand synthesis. Of these 30, two were unable to be synthesized, leaving 28 candidates to test for binding to PGAM5 (Fig. 3.2). The initial 28 compounds were a combination of fragments and lead-like molecules and were tested in their ability to modulate PGAM5's phosphatase activity and ability to form higher order structures.

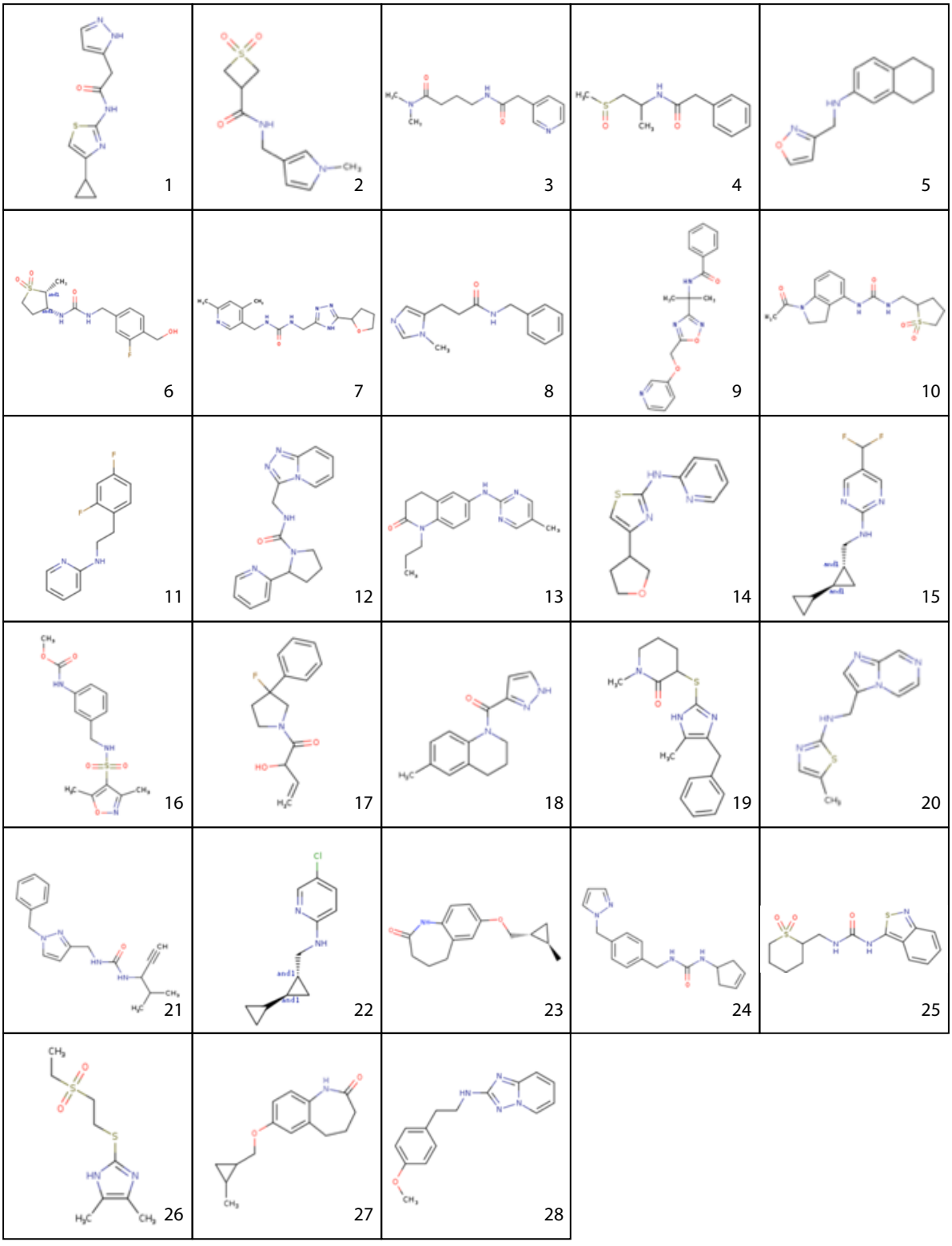

Figure 3.2: 28 potential PGAM5 compounds. Combination of fragment and lead-like compounds acquired from Enamine based on their potential to bind to and modulate PGAM5's activity and ability to form higher order structures.

Effect of compound on different oligomeric states of PGAM5

Now that we had identified potential modulators of PGAM5, we began by testing their activity towards purified Δ48 PGAM5. To saturate the protein and attempt to disrupt any previously bound multimerization motif bound in the allosteric pocket, we incubated 20 nM final concentration of purified protein with 1 mM of compound. Each activity assay was initiated with the addition of 75 μM final concentration of pASK1 substrate peptide. Quenching and subsequent detection of the free phosphatase in solution was followed by normalization of the observed activities relative to the negative control Δ48 WT incubated with DMSO and tested with pASK1 peptide. Preliminary experiments indicate that four of the compounds generated had an effect on phosphatase activity. Compounds 13, 19, 22, and 28 resulted in a 25% decrease in phosphatase activity and appeared the most promising compounds to pursue in further studies (Fig. 3.3).

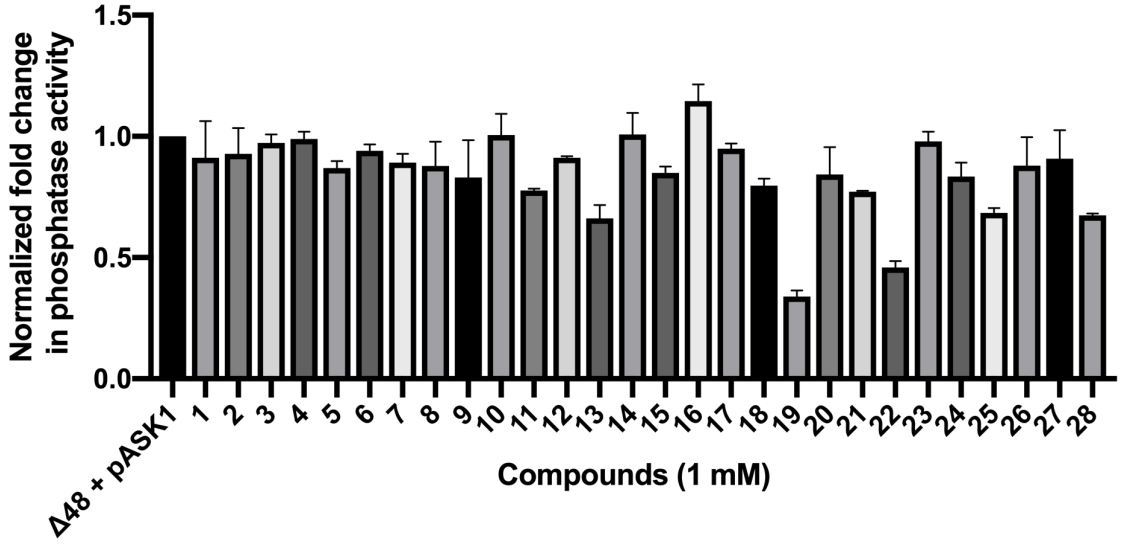

Figure 3.3: Activity of Δ48 PGAM5 incubated with compounds for pASK1 substrate. 20nM Δ48 PGAM5 incubated with 1mM compound, followed by exposure to 75 μM pASK1 substrate peptide. Activity normalized for phosphatase activity of Δ48 in the presence of DMSO for pASK1.

Curious to more rigorously parse filamented from dimeric protein, we repeated this experiment immediately after size exclusion purification of Δ48 PGAM5. Freshly collected peak

maxima from the filamented and dimeric peaks were incubated with 1 mM compound and tested for phosphatase activity against substrate 75 μM final concentration of pASK1 substrate peptide (Fig. 4). Similar to earlier experiments, compounds 13, 19, 22 and 28 showed a consistent decrease in phosphatase activity, though the exact effect they had on filaments or dimeric protein was varied. Significantly more variation in the effect of the compounds on dimeric PGAM5 was observed, which may have been contributed to by our earlier observation that the dimeric peak of Δ48 PGAM5 is able to spontaneously dodecamerize and are able to subsequently form filaments in solution, which may affect the compound's ability to interact with PGAM5 at the target allosteric pocket of interest.

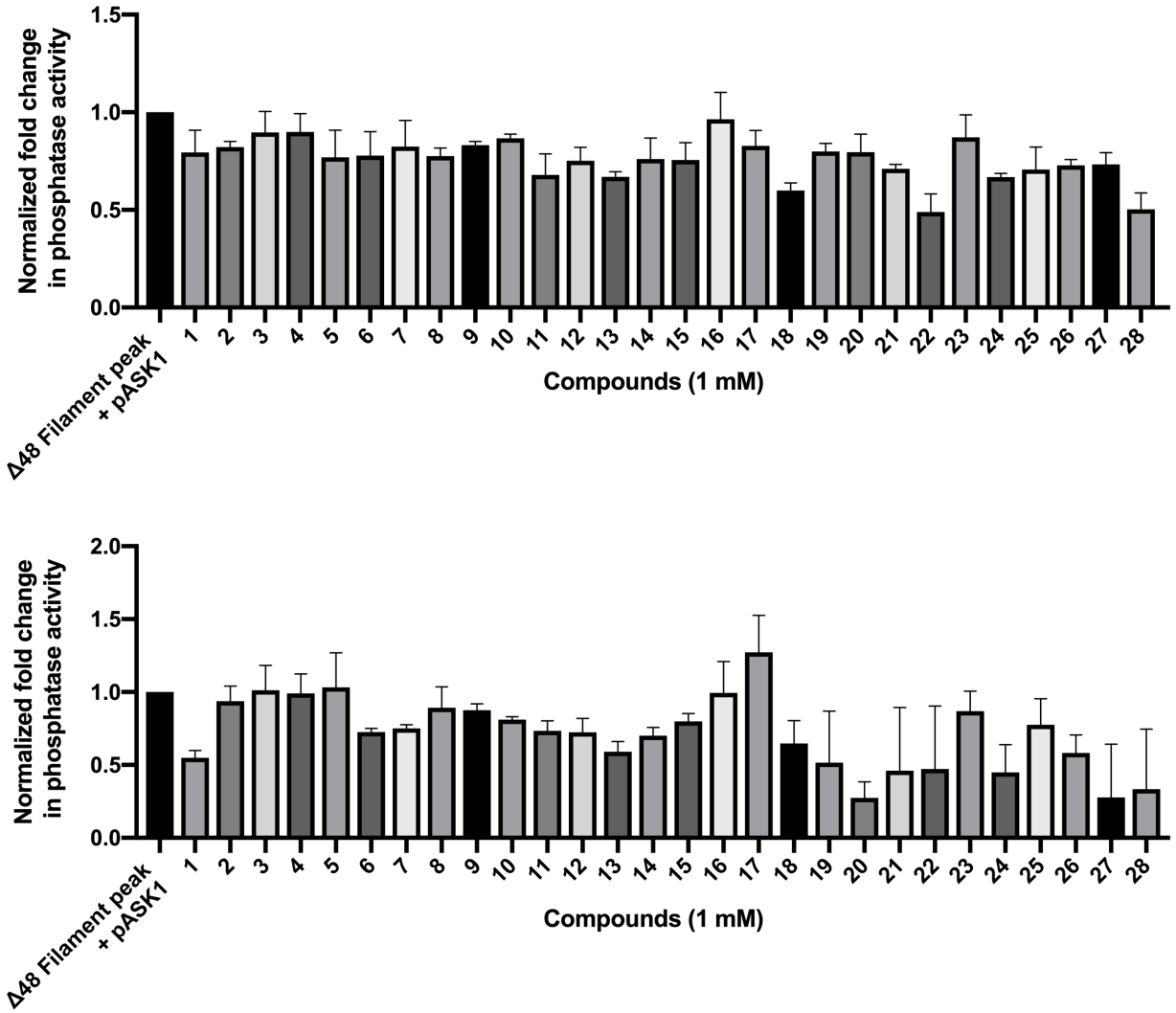

Figure 3.4: Activity assays of filamented or dimeric PGAM5 in the presence of compounds. Phosphatase activity assays of filament peak (upper panel) and dimeric peak (lower panel) 20nM Δ48 PGAM5 for 7μM pASK1 peptide after incubation with 1 mM of each of the compounds.

Given the tight interaction between the multimerization motif and the allosteric pocket of PGAM5, we were curious if the binding affinity between the compounds and the allosteric pocket might be too weak to dislodge any previously bound multimerization motif. To spatially separate the multimerization motif from the phosphatase domain, we opted to set up a competition assay in which we incubated the purified Δ90 catalytic core of PGAM5 with the compounds, followed by subsequent addition of the multimerization motif peptide added *in trans*. Previous assays have indicated Δ90 PGAM5 alone has poor catalytic activity on the order of hours; given this consideration, we incubated the phosphatase reaction for three hours at room temperature. Quenching and subsequent detection of the free phosphatase in solution followed by normalization of the observed activities relative to the negative control Δ90 WT incubated with DMSO, incubated with the multimerization motif and subsequently and tested with pASK1 peptide indicates that the majority of the compounds had an effect on phosphatase activity (Fig. 3.5). The decrease in phosphatase activity observed compared to the filamented form of the protein suggests that the compound's inability to better inhibit phosphatase activity may be due to its inability to access the allosteric pocket in the presence of a pre-bound multimerization motif.

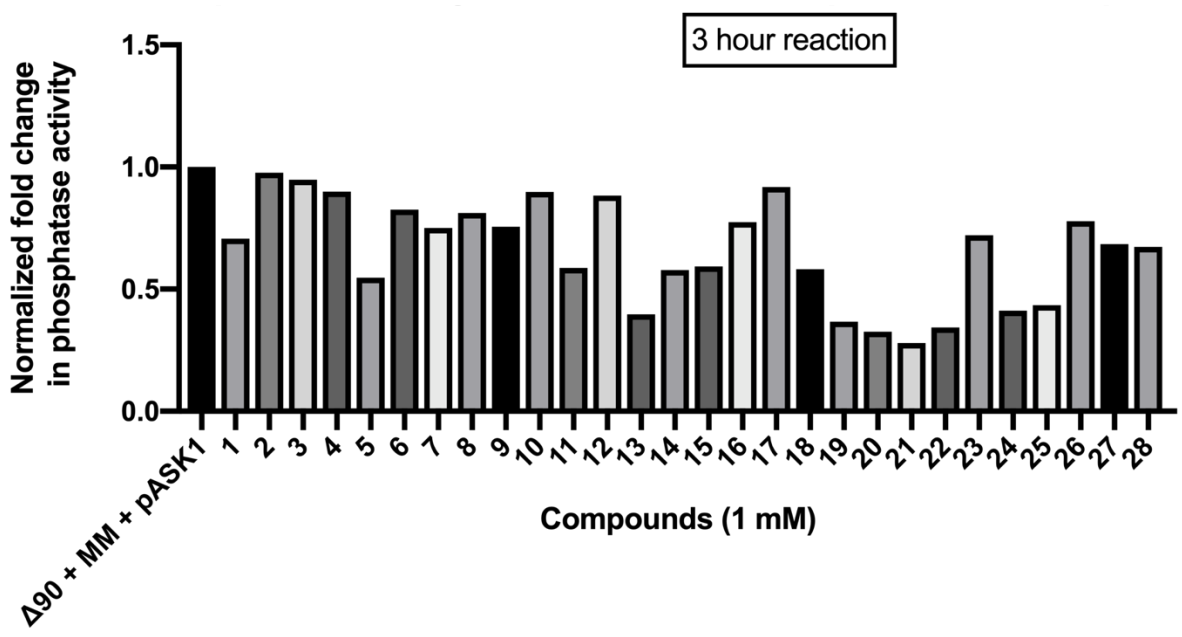

Figure 3.5: Effect of compounds on activity of Δ 90 PGAM5. 500nM Δ90 PGAM5 incubated with 1mM compound, followed by incubation with 20uM multimerization motif and subsequent exposure to 75uM pASK1 peptide.

Dose response of best hits

Given that we do not know the oligomeric state of PGAM5 while on the mitochondrial membrane, or if the multimerization motif is able to interact with the catalytic core while membrane tethered, we became most interested in further exploring the compounds that show most potent effect on filamented PGAM5, as these most likely possessed the highest binding affinity for the protein. Cross comparison of the effect of the 28 compounds on PGAM5's phosphatase activity led us to decide to focus on compounds 13, 19, and 22, as these consistently showed consistent phosphatase activity inhibition in the presence of the multimerization motif containing construct. We decided to perform a dose response of compound 3, one with which we had seen no real change on PGAM5's activity as a phosphatase, in parallel as a negative control. In order to begin to determine the range of inhibition of the compounds of interest for PGAM5 and their maximal inhibitory effect, we performed a dose response experiment in which we varied the concentration of

compound while maintaining the concentration of Δ48 WT protein constant (Fig. 3.6). Based on our dose response data, we were able determine for efficient binding and inhibition of PGAM5, we would require concentrations higher than 1mM of compound for our crystallography and future activity assays. This proved challenging, especially given some difficulty we observed with compound precipitation, particularly with compound 22, which we observed readily precipitates out of solution at concentrations higher than 1mM. Despite this, we were able to determine binding of compound binding to PGAM5 is weak and suggested our follow up crystallographic and activity assays would require high concentrations of compound to bind to and inhibit PGAM5.

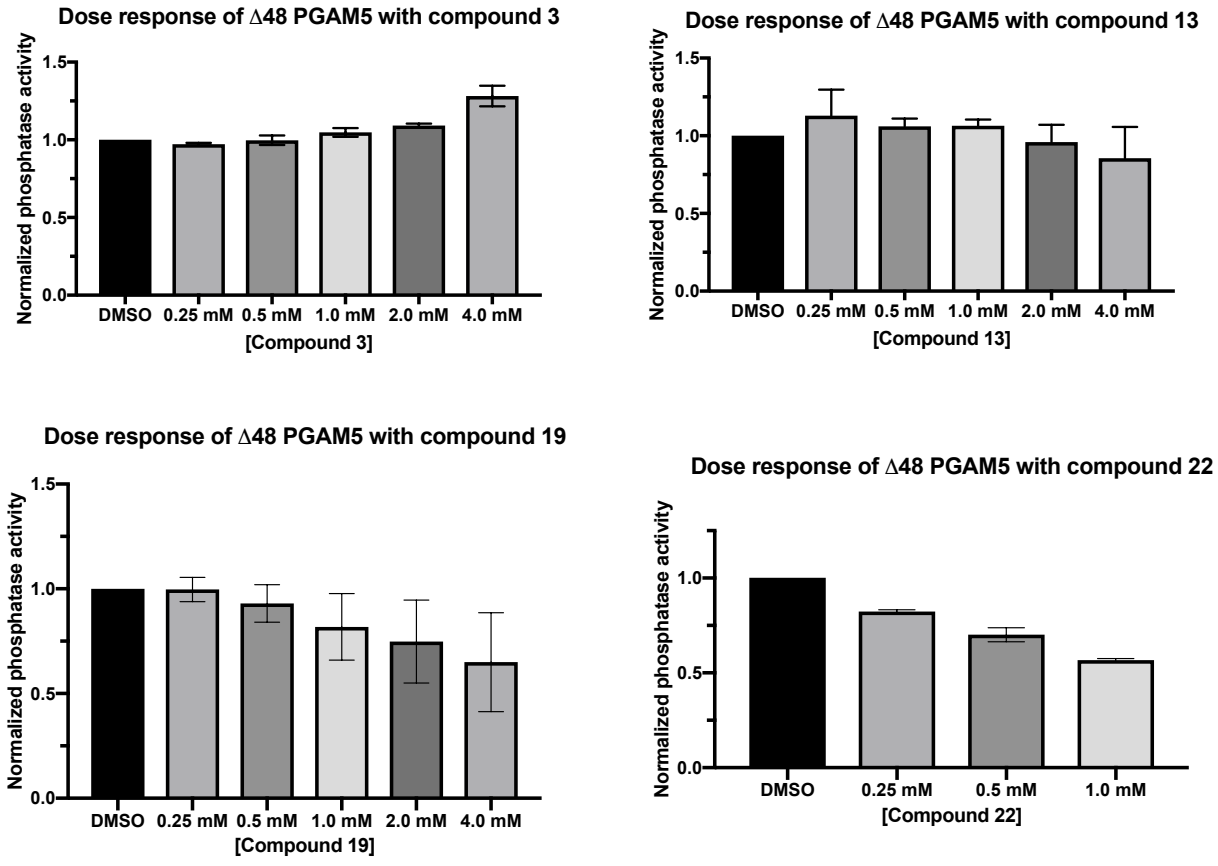

Figure 3.6: Dose response of Δ 48 PGAM5 for compounds of interest. 20nM Δ48 PGAM5 was incubated with a range of compounds 3, 13, 19 or 22 ranging from 0-4mM (upper left, upper right, lower left, lower right, respectively). Data for compound 22 higher than 1mM excluded due to precipitation.

Compound specificity for PGAM5

One concern with initial trials of compounds on receptor activity is that these novel compounds may aggregate, causing receptor aggregation and an artificial, non-specific decrease in target protein activity. To validate the specificity of the compounds of interest for PGAM5 in inhibiting its phosphatase activity, we tested whether the most promising compounds would inhibit activity of an unrelated protein. We incubated BMPR2 kinase with 1mM of compounds 13, 19 and 22 and observed these compounds show no significant effect on the kinase's activity. The lack interference of BMPR2's kinase activity in the presence of 1mM of each of the compounds as compared to a DMSO control indicates the ability of these compounds to inhibit PGAM5 is specific an is not merely due to compound-directed protein aggregation (Fig. 3.7). Now that we were able to determine the interaction these compounds have with PGAM5 is specific, we pursued a high-resolution structure of the interaction of our PGAM5 protein with these novel compounds.

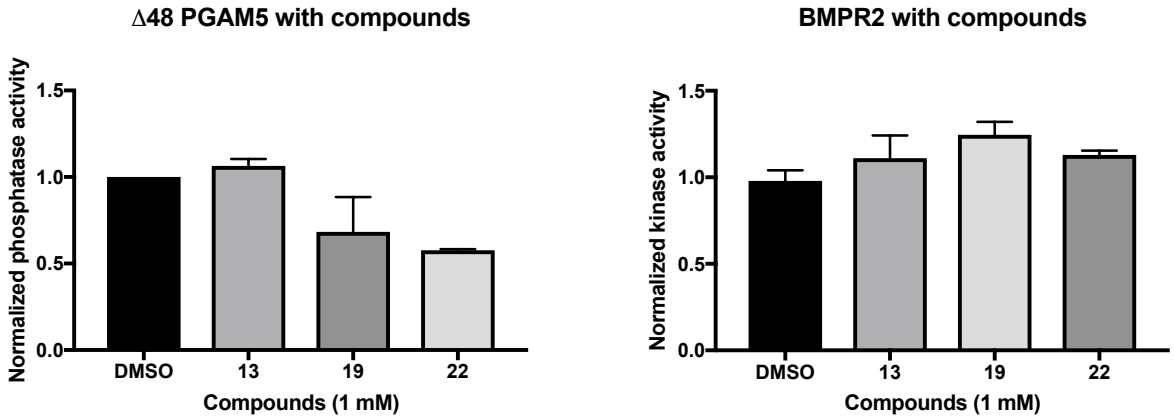

Figure 3.7: Compound specificity for PGAM5. Validating specificity of compound inhibition for PGAM5 through a phosphatase assay (left) compared to kinase assay for BMPR2 done in presence of BMPR2 kinase pre-incubated with compounds (right).

Crystallization of Δ90 PGAM5 in presence of most promising compounds

Identification and preliminary testing of the possible compounds suggests that these compounds are able to specifically inhibit PGAM5's phosphatase activity. In an effort to verify the site of interaction of these compounds with PGAM5, we sought to solve a crystal structure of the catalytic core of PGAM5 with compounds 13, 19 or 22.

Our initial crystallographic attempts focused on soaking existing Δ90 H105A and Δ90 WT PGAM5 crystals with serial dilutions of the compounds (Fig. 3.8). We generated crystals for PGAM5 in identical conditions to our Δ90 H105A structure (PDB: 6NCI) and first attempted to bind compound to protein by incubating our protein crystals in the presence of compounds 13, 19 and 22. Given that our crystals appeared stable in the presence of compound for multiple days and up to a week, we proceeded with data collection. Using molecular replacement, we were able to solve the structure of Δ90 PGAM5 but were dismayed to find a lack of density for each of the compounds in the allosteric pocket. Analysis of the electron density revealed that rather than having compound bound in the allosteric pocket, the N-terminal scar resulting from the TEV cleavage of the 6xHIS tag at the N-terminus of our construct occluded the predicted compound binding site. We were unable to observe any corresponding to compound bound to PGAM5 for in any of these crystal structures.

Our subsequent attempts focused on co-crystallizing Δ90 H105A WT PGAM5 with compounds. To this end, we incubated the protein with 2.5mM of each compound, centrifuged to remove any excess precipitant and crystallized in earlier $MgCl_2$, HEPES and PEG solution found to yield abundant crystals and crystallized in hanging drop. Our observation that PGAM5 was able to crystallize in the presence of compound left us hopeful that the protein had succeeded in interacting with compound and we proceeded with data collection and processing. Despite having

crystallized the protein in the presence of each of the compounds, we found that all of the structures we solved lacked density for any of the compounds, and instead observed the N-terminal TEV-cleave site methionine overhang once again occupied the region of interest. In an effort to relieve this potential overhang and leave the region of interest exposed for compound to interact with and have the ability to bind in PGAM5's allosteric pocket, we decided to modify our crystallographic construct.

Optimization and purification of 3x-GS linker-Δ94 PGAM5

Due to our identification of the N-terminus TEV scarring site in the allosteric pocket of PGAM5, we decided to generate various constructs of PGAM5 that would eliminate the N-terminal's association with the region of interest. Cleavage of our N-terminal 6x-HIS tag resulted in a methionine overhang, which interacted consistently with the region of interest. In an effort to eliminate this interacted, we proceeded to generate a construct with a singular patch of GS residues immediately following the 6x-HIS tag. Additionally, we generated a construct with a repeating 3x-GS linker immediately after the 6x-HIS tag.

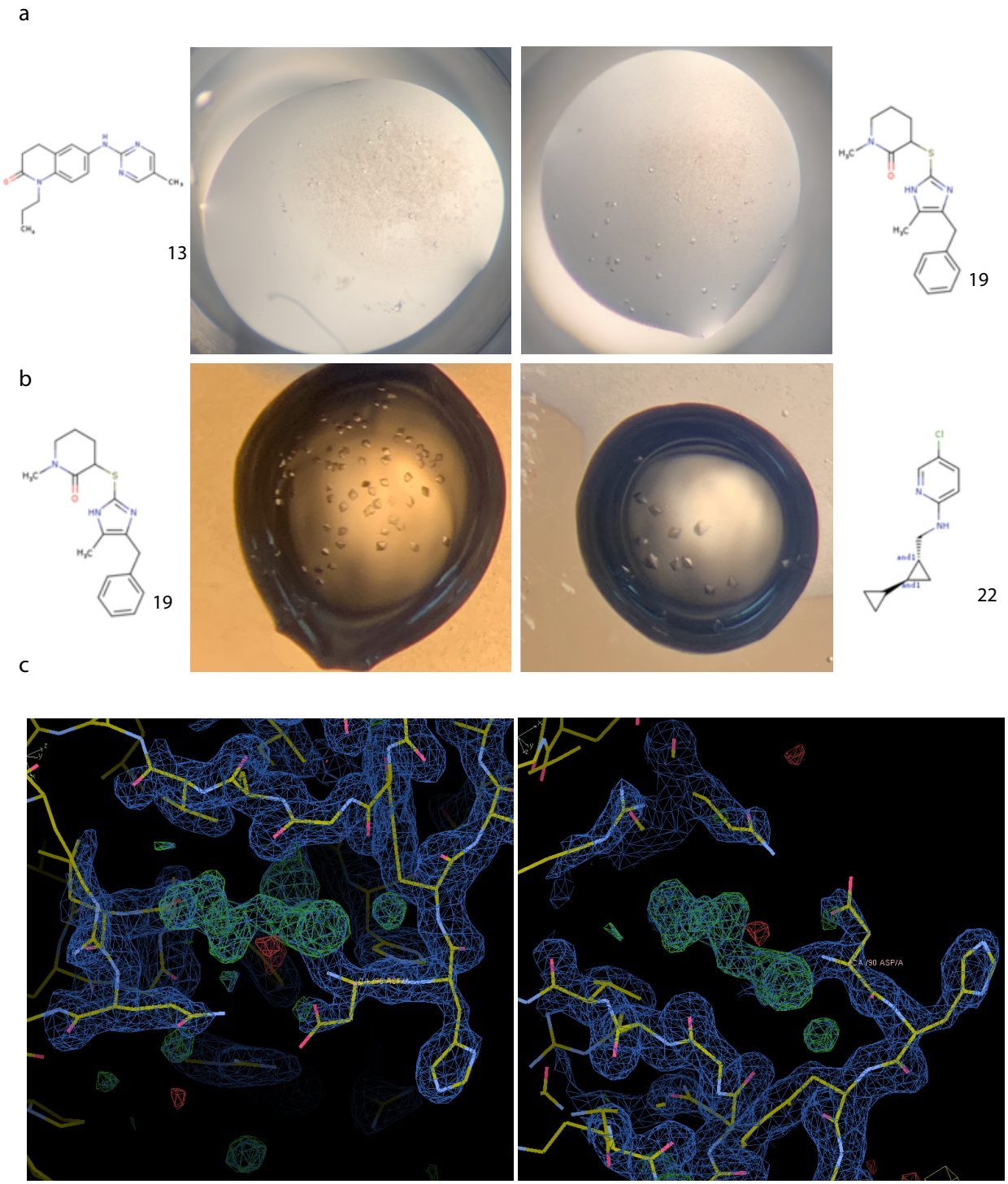

Figure 3.8: Crystallographic attempts with PGAM5 and compounds. a. Soaked Δ94 H105A PGAM5 crystals in compounds 13 and 19. **b.** Co-crystallization of Δ94 H105A PGAM5 with compounds 19 and 22. **c.** Two views of PGAM5's allosteric pocket showing electron density for Δ94 H105A PGAM5 co-crystallized with compound 13. Green mesh indicates observed region of density for overhang methionine in lieu of compound density.

3.3 DISCUSSION

While phosphatases have remained largely understudied, the critical roles they play in the cell through their ability to post-translationally modify substrates and directly affect cellular outcomes make them an important region of study. PGAM5's emergence as a regulator of cellular life and death, as well as a novel signaling node implicated in vastly different functions within the mitochondria, presents this atypical phosphatase as a fascinating subject of study. Its novel mode of self-regulation and complex higher order structure make it a compelling yet challenging potential drug target.

In collaboration with the Shoichet lab at UCSF, we have identified and characterized 28 possible novel regulators of PGAM5's phosphatase activity and have performed preliminary analyses on their ability to interact with the phosphatase to modulate its phosphatase activity. We have parsed these compounds by their ability to interact with the catalytic core of PGAM5 through interactions with Δ90 PGAM5 and their ability to bind to and inhibit Δ48 PGAM5 as a dimer or filament. We have identified three compound candidates which we believe would be of interest to optimize and pursue further through biochemical, cellular and structural means.

Finding a way to tightly control PGAM5's ability to self-associate and self-activate would be of therapeutic value and would yield a great new tool through which to control various mitochondrial pathways and cell life or death. Our work has provided new structural insights behind the mechanism of PGAM5's activation as a phosphatase, but much remains unknown about this peculiar phosphatase and the ways in which it controls cellular outcomes. It remains a possibility that PGAM5's interaction with its wide variety of protein binding partners and its ability to function as a signaling node between mitochondrial homeostasis or cell death could be regulated by its multimeric state.

Following the conclusion of these experiments, it has been observed PGAM5's dynamic multimers are able to dephosphorylate BCL-xL or FUNDC1, and in doing so, effectively regulate mitochondrial and cellular fate[16]. Dephosphorylation of BCL-xL by dimeric PGAM5 has been found to result in anti-apoptotic activity, while it was found that under induced oxidative stress conditions, the amount of multimerized PGAM5 increases and results in dephosphorylation of FUNDC1. Dissociation of PGAM5 from BCL-xL and association with FUNDC1 has been observed to result in mitochondrial fission and mitophagy, putting forth the idea that PGAM5 is able to function as a sensor for oxidative stress and respond by changing its oligomerization state, substrates, and thereby regulate mitochondrial integrity and morphology. Ultimately, it is postulated PGAM5's oligomeric state may be able to determine whether the cell will live or die. These new and exciting results shed light on the importance of designing, testing and optimizing small molecule inhibitors of PGAM5, a feat which our laboratory will continue to pursue. Additional work is needed to further optimize, characterize and improve the ability of these preliminary compound hits for PGAM5, but will yield great tools to further study this fascinating atypical protein phosphatase.

3.4 METHODS

Protein expression and purification: Wild type full-length PGAM5 cDNA (corresponding to the PGAM5 long isoform (PGAM5L), residues 1-289) was purchased from Addgene. For bacterial expression and purification, the Δ90 PGAM5 (residues 91-289) and Δ48 PGAM5 (residues 49-289) were cloned into the pET28a expression vector (Novagen). These constructs were N-terminally tagged with hexahistidine (6X-HIS) followed by a linker sequence encoding a TEV protease cleavage site (ENLYFQS). Addition of a GS-linker was added (3x-GS) for additional crystallographic experiments by adding GSGSGS sequence between the N-terminal 6X-HIS and TEV sites and residue 95 of PGAM5 (3xGS-Δ94 PGAM5). Mutations were introduced using either QuickChange mutagenesis or through Gibson assembly[17]. Primers used for mutagenesis are as follows: H105A (Forward: 5'-acatcttcctcatcagggcttcccagtaccacgtgg-3' Reverse: 5'-ccacgtggtactgggaagccctgatgaggaagatgt-3'), Y198E (F: 5'-gctccgtcttcctcatactgcacagcttccggc-3' R: 5'-gccggaagctgtgcagtatgaggaagacggagc-3'), R65A (F: 5'-agagacagtggttctgccctgtcccagttggg-3' R: 5'-cccaactgggacagggcagaaccactgtctct-3'), F244E (F: 5'-gccagccttcaggaggctcctgcagtgctctgcac-3' R: 5'-gtgcagagcactgcaggagcctcctgaaggctggc-3'), R288E (F: 5'-cctcccgacaagatcactgaatcctgagatccgaattc-3' R: 5'-gaattcggatctcaggattcagtgatcttgtcgggagg-3'). Mutation of WT A4 was done by sequential mutation of W58A and D59A and followed by W62A and D63A. W58A/D59A (F: 5'- gtcccagttgggggccgcgacaccggggccc-3' R: 5'-gggccccggtgtcgcggcccccaactgggac-3'), W62A/D63A (F: 5'- gtggttctcgcctggccgcgttggggtcccaga-3' R: 5'- tctgggaccccaacgcggccaggcgagaaccac-3').

For recombinant protein expression, BL21 DE3 pLysS *E. coli* cells transformed with pET28a-PGAM5 constructs were cultured in Luria Broth media supplemented with kanamycin (30 μg/mL) at 37° C until 0.4 optical density at 600 nm was reached. Protein expression was

induced with 0.2 mM IPTG and cells were cultured for additional 12 hours at 25° C. Following collection by centrifugation at 5000 x g, cell pellets were resuspended in Lysis Buffer (20 mM Tris-Cl pH 8.0, 500 mM NaCl, 0.5 mM TCEP, 5% glycerol, 20 mM Imidazole pH 8.0 supplemented with EDTA-free protease inhibitors (Roche)). Cells were lysed by sonication at 25% of max power in cycles of 4s on and 2s off for 5 minutes. Lysates were clarified by centrifugation at 18,000 x g and loaded by gravity flow on HiTrap Ni-NTA resin (GE Healthcare). Protein was eluted using Elution Buffer (20 mM Tris-Cl pH 8.0, 500 mM NaCl, 0.5 mM TCEP, 5% glycerol, 200 mM Imidazole pH 8.0) and exchanged into buffer containing 20 mM Tris-Cl pH 8.0, 150 mM NaCl, and 0.5 mM TCEP using a 10 kDa cutoff concentrator (Millipore). The sample was further purified by size exclusion chromatography (SEC) using a Superose 6 10/300 GL Increase column (GE Healthcare) equilibrated in buffer containing 20 mM Tris-Cl pH 8.0, 150 mM NaCl and 0.5 mM TCEP. Fractions were collected and used immediately for activity assays or to set crystallography trays.

PGAM5 expression in Jurkat cells: Wild type full-length PGAM5 cDNA (corresponding to the PGAM5 long isoform (PGAM5L), residues 1-289) was purchased from Addgene. For expression in Jurkat cells, full-length and Δ2-24 (residues 24-289) PGAM5 variants for mammalian cell expression and imaging were cloned into the pIRES2 vector (Invitrogen). Jurkat cells were acquired from J. McLaurin in the Weiner lab at UCSF. Cells were transfected with pIRES2 vectors using Trans-IT Jurkat transfecting reagent (Mirusbio Cat # MIR2120) following recommended manufacturer protocols.

Modeling: Docking for the allosteric pocket of PGAM5 with lead-like molecules and fragments was performed using DOCK3.7 by Trent Balius, PhD. DOCK3.7 is freely available for non-commercial research (http://dock.compbio.ucsf.edu/DOCK3.7/).Compounds docked in this study are freely available on the Irwin and Shoichet lab lead-like make on demand library (http://zinc15.docking.org/). Compounds were purchased from Enamine, Kiev, Ukraine.
Chemaxon was used to protonate ligands, Corina was used to generate the initial 3D conformation, AMSOL used to calculate partial charges and desolvation values, Omega from OpenEye was used to conformationally expand ligands and mol2todb2.py was used to generate the dockable db2.gz files from output from the previous steps. The above steps were run through the *generate/build_database_ligand.sh* script provided with the DOCK 3.7 distribution

Compound acquisition, dilution and storage: Compounds were purchased from Enamine (https://enamine.net/) and were received as a mixture of viscous oils or powders. Compounds were dissolved in 100% fresh DMSO to make up 250 mM stocks and stored in glass vials with parafilm. Stocks were kept at -20 ^{o} C for long term storage. Aliquots were made to be used for experiments to avoid repetitive freeze-thawing of compounds. Compound ID, ZINC ID, molecular weight (MW) and logp values provided in table 2.1.

Peptides: The ASK1 phosphopeptide (NFEDH(pS)APPSP) and the PGAM5 multimerization motif (MM) peptide (GPGVWDPNWDRREP)[9] were purchased at a purity of 95% or greater (Elim Biopharma). Peptides were resuspended in 20 mM Tris-Cl pH 7.5, aliquoted, and flash frozen in liquid nitrogen prior to storage at -80^{o} C.

Table 3.1: Enamine compound ID, ZINC ID, molecular weight and logp values

Compound	ID	ZINC ID	mwt	logp
1	Z1255564056	ZINC000121091067	248.311	1.925
2	Z2772154651	ZINC000631611880	242.3	-0.314
3	Z1177728516	ZINC000348868450	249.314	0.609
4	Z1656071016	ZINC000182751233	239.34	1.112
5	Z2285860826	ZINC000651254919	228.295	3.166
6	Z2808669295	ZINC000636686801	330.381	0.693
7	Z2496159919	ZINC000654585699	330.392	1.667
8	Z1835946072	ZINC000188385791	243.31	1.669
9	Z2160513701	ZINC000347306850	338.367	2.709
10	Z1709214128	ZINC000575636852	351.428	1.294
11	Z1183910699	ZINC000069798379	234.249	3.014
12	Z813229004	ZINC000056557853	322.372	2.171
13	Z1583451895	ZINC000091025924	296.374	3.218
14	Z1686540422	ZINC000273841125	247.323	2.786
15	Z2274656608	ZINC000450928572	239.269	2.294
16	Z2069918626	ZINC000496476237	339.373	1.948
17	Z2638697773	ZINC000614530974	249.285	1.631
18	Z381616680	ZINC000047989063	241.294	2.311
19	Z1618007411	ZINC000539806212	315.442	3.022
20	Z1673501846	ZINC000170594968	245.311	2.106
21	Z2044042936	ZINC000284152823	310.401	2.388
22	Z2274654255	ZINC000382428661	222.719	2.615
23	Z3252177877	ZINC000629359812	245.322	2.996
24	Z1416609479	ZINC000675300140	296.374	2.449
25	Z2840961144	ZINC000640249651	339.442	2.385
26	Z2217546493	ZINC000292716812	248.373	1.553
27	Z2721846482	ZINC000629359812	245.322	2.996
28	Z1787490399	ZINC000094601543	268.32	2.393

Phosphatase activity assay: Phosphatase assays were performed at room temperature for wild type 6xHIS-Δ48 PGAM5 and 6xHIS-Δ90 PGAM5. Protein was diluted into reaction buffer to a final concentration of 20 nM and incubated with 1mM final concentration of each compound. DMSO was used as a negative control for each series of reactions, and each reaction was set up in triplicate. Protein was incubated in the presence of compound for 25-30 minutes at room temperature prior to addition of the substrate peptide. ASK1 phosphopeptide was diluted to 750 μM into reaction buffer (20 mM Tris-Cl pH 8.0, 150 mM NaCl and 0.5 mM TCEP) and reaction was initiated by addition of substrate peptide to compound and protein incubation mixture. Reaction was run for 10 minutes at room temperature prior to quenching with R&D Malachite Green phosphate detection kit (Cat: DY996) following manufacturer protocol. The total free phosphatase in solution was measured as the absorbance at 620 nm.

X-ray crystallography:

Soaking of Δ90 H105A PGAM5 with compounds 13, 19 and 22: The Δ90 H105A PGAM5 construct was crystallized using hanging drop vapor diffusion at room temperature in the absence of the ASK1 phosphopeptide. Crystals were grown in a 2 μL drop (1 μL protein reservoir solution) against a reservoir solution comprised of 100 mM HEPES pH 7.5, 200 mM $MgCl_2$ and 30% w/v PEG 400. Once crystals were fully grown, crystals were soaked in 0-2.5mM of each of the compounds for 24-72 hours at room temperature. Crystals from both conditions were cryoprotected with Paratone-N oil and flash-cooled to 100 K in liquid nitrogen.

Co-crystallization of Δ90 H105A PGAM5 with compounds 13, 19 and 22: Purified protein was concentrated to 10 mg ml^{-1} by centrifugation (Amicon Ultra-15, 10 kDa molecular mass cutoff;

Millipore). Initial attempts to combine purified recombinant Δ90 H105A with various concentrations of compounds between 0-2.5mM resulted in precipitation of protein in the drops but yielded protein crystals over 1 week. Crystals were cryoprotected with Paratone-N oil and flash-cooled to 100 K in liquid nitrogen.

Data collection: X-ray diffraction data were collected at 1.111 Å, 77K at the ALS 8.3.1. beamline (Berkeley, CA) on a Pilatus 6M detector. Data were indexed with XDS[18], scaled in Aimless[19] and phases determined in Phaser[20]. Δ90 PGAM5 H105A crystals diffracted to 1.7 Å in space group $P2_12_12_1$ and with unit cell dimensions: a = 71.0 Å, b = 72.0 Å, c = 81.9 Å, $\alpha = \beta = \gamma = 90°$ and with two molecules in the asymmetric unit. A solution was generated by molecular replacement using one copy of PDB 3MXO as the search model. Refinement was performed in Phenix[65] with iterative rounds of model building in Coot[21].

3.5 ACKNOWLEDGEMENTS

We are grateful to Justin McLaurin and Orion Weiner's lab for providing Jurkat T-cells, and to Jane Gordon and Sarah Elmes for their assistance with training and in setting up the flow cytometry machines used (FACS Calibur) at UCSF. We are thankful to Trent Balius for all of his work in compound design and optimization, and for all of his continued support through the early compound testing phase. We would like to thank the rest of the Shoichet lab for their experimental assistance and for their help in further optimizing our first round of compound hits. Additionally, we would like to thank the staff at the ALS 8.3.1. beamline for assisting with X-ray diffraction experiments, the Shoichet lab for their assistance and participation in the 'hit picking party' in predicting compounds. We would especially like to thank Christopher Agnew for all of his

guidance and assistance with crystallography data collection and processing, and for performing the BMPR2 kinase assay, without whom this work would not have been possible. Additionally, we would like to thank all of the members of the Jura lab for their advice, helpful discussions and feedback.

3.6 REFERENCES

1. Sadatomi D, Tanimura S, Ozaki K, Takeda K. Atypical protein phosphatases: emerging players in cellular signaling. Int J Mol Sci. 2013;14(3):4596-612.
2. Wang Z, Jiang H, Chen S, Du F, Wang X. The mitochondrial phosphatase PGAM5 functions at the convergence point of multiple necrotic death pathways. Cell. 2012;148(1-2):228-43.
3. Moriwaki K, Farias Luz N, Balaji S, De Rosa MJ, O'Donnell CL, Gough PJ, et al. The Mitochondrial Phosphatase PGAM5 Is Dispensable for Necroptosis but Promotes Inflammasome Activation in Macrophages. J Immunol. 2016;196(1):407-15.
4. Wu H, Xue D, Chen G, Han Z, Huang L, Zhu C, et al. The BCL2L1 and PGAM5 axis defines hypoxia-induced receptor-mediated mitophagy. Autophagy. 2014;10(10):1712-25.
5. Sekine S, Yao A, Hattori K, Sugawara S, Naguro I, Koike M, et al. The Ablation of Mitochondrial Protein Phosphatase Pgam5 Confers Resistance Against Metabolic Stress. EBioMedicine. 2016;5:82-92.
6. Panda S, Srivastava S, Li Z, Vaeth M, Fuhs SR, Hunter T, et al. Identification of PGAM5 as a Mammalian Protein Histidine Phosphatase that Plays a Central Role to Negatively Regulate CD4(+) T Cells. Molecular cell. 2016;63(3):457-69.
7. Lo SC, Hannink M. PGAM5 tethers a ternary complex containing Keap1 and Nrf2 to mitochondria. Experimental cell research. 2008;314(8):1789-803.
8. Lo SC, Hannink M. PGAM5, a Bcl-XL-interacting protein, is a novel substrate for the redox-regulated Keap1-dependent ubiquitin ligase complex. The Journal of biological chemistry. 2006;281(49):37893-903.

9. Wilkins JM, McConnell C, Tipton PA, Hannink M. A conserved motif mediates both multimer formation and allosteric activation of phosphoglycerate mutase 5. The Journal of biological chemistry. 2014;289(36):25137-48.
10. Zhuang M, Guan S, Wang H, Burlingame AL, Wells JA. Substrates of IAP ubiquitin ligases identified with a designed orthogonal E3 ligase, the NEDDylator. Molecular cell. 2013;49(2):273-82.
11. Zhou W, Yin Y, Weinheimer AS, Kaur N, Carpino N, French JB. Structural and Functional Characterization of the Histidine Phosphatase Domains of Human Sts-1 and Sts-2. Biochemistry 2017 56 (35), 4637-4645.
12. Coleman RG, Carchia M, Sterling T, Irwin JJ, Shoichet BK. Ligand pose and orientational sampling in molecular docking. PLoS One. 2013 Oct 1;8(10):e75992.
13. Lyu J, Wang S, Balius TE, Singh I, Levit A, Moroz YS, O'Meara MJ, Che T, Algaa E, Tolmachova K, Tolmachev AA, Shoichet BK, Roth BL, Irwin JJ. Ultra-large library docking for discovering new chemotypes. Nature. 2019 Feb;566(7743):224-229.
14. Sterling T, Irwin JJ. ZINC 15 – Ligand Discovery for Everyone. Journal of Chemical Information and Modeling 2015 55 (11), 2324-2337.
15. Kuntz ID, Blaney JM, Oatley SJ, Langridge R, Ferrin TE. A geometric approach to macromolecule-ligand interactions. J Mol Biol. 1982 Oct 25;161(2):269-88.
16. Ma K, Zhang Z, Chang R, Cheng H, Mu C, Zhao T, Chen L, Zhang C, Luo Q, Lin J, Zhu Y, Chen Q. Dynamic PGAM5 multimers dephosphorylate BCL-xL or FUNDC1 to regulate mitochondrial and cellular fate. Cell Death Differ. 2019 Jul 31. doi: 10.1038/s41418-019-0396-4. [Epub ahead of print]

17. Gibson, D.G. et al. Enzymatic assembly of DNA molecules up to several hundred kilobases. Nat Methods **6**, 343-5 (2009).
18. Kabsch, W. Integration, scaling, space-group assignment and post-refinement. Acta Crystallogr D Biol Crystallogr 66, 133-44 (2010).
19. Otwinowski, Z. & Minor, W. Processing of X-ray diffraction data collected in oscillation mode. Methods Enzymol 276, 307-26 (1997).
20. McCoy, A.J. et al. Phaser crystallographic software. J Appl Crystallogr 40, 658-674 (2007).
21. Emsley, P. & Cowtan, K. Coot: model-building tools for molecular graphics. Acta Crystallogr D Biol Crystallogr 60, 2126-32 (2004).

Publishing Agreement

It is the policy of the University to encourage the distribution of all theses, dissertations, and manuscripts. Copies of all UCSF theses, dissertations, and manuscripts will be routed to the library via the Graduate Division. The library will make all theses, dissertations, and manuscripts accessible to the public and will preserve these to the best of their abilities, in perpetuity.

Please sign the following statement:

I hereby grant permission to the Graduate Division of the University of California, San Francisco to release copies of my thesis, dissertation, or manuscript to the Campus Library to provide access and preservation, in whole or in part, in perpetuity.

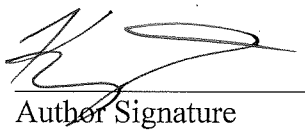

Author Signature

9/9/2019

Date